Effect of the Anode Fall on the Electron Density Balance in Anode Plasma with Electric Double Layer

T. Kh. Guseĭnov[a,*], M. Moslehi-Fard[b,**], and A. Kh. Muradov[a]

[a] *Baku State University, Baku, Azerbaijan*
[b] *Tabriz State University, Tabriz, Iran*
*e-mail: * htarlan@box.az; ** moslehi@tabrizu.ac.ir*
Received June 9, 2004

Abstract—The depth of a potential well in anode plasma with electric double layer was measured in a nonstationary regime and was found to exhibit chaotic oscillations. It is concluded that the anode fall plays the role of a valve controlling the concentration of electrons trapped in the anode plasma. The measurements were performed using a multigrid electron energy analyzer under the conditions when the floating potential in front of the anode passed through a certain level. The distribution of the potential well depths was studied. The most probable values fall within an interval from 3 to 6 V. Substitution of the obtained values into the average electron density balance equation provides satisfactory agreement in the order of magnitude of the electron density. © 2005 Pleiades Publishing, Inc.

Introduction. The results of investigations of electric double layers (DLs) in plasma showed that several groups of transmitted and reflected particles must be present in order to provide for a stationary DL in plasma or in the electron beam–plasma system [1, 2]. These groups have been experimentally observed [3, 4], and the densities and energy distributions of such transmitted and reflected (trapped) electrons [5], as well as the thermal energies of ions in plasmas with DLs [6], have been measured. [5]. Although it was pointed out [1, 4] that a stable DL can, in principle, exist without a component of electrons reflected from the DL, the presence of such particles on both sides of the potential minimum is stipulated in most real cases.

In view of the significant role of trapped electrons in systems with DLs, it is important to study their properties and the factors determining their density, energy spectrum, etc. Under the experimental conditions studied in [4, 5], where the entire plasma beam occurred in a longitudinal magnetic field (so that electrons were magnetized, but not ions), the field prevented electrons from moving toward the walls in the transverse direction. In the axial direction (at the edges), electrons could not leave the anode plasma by moving toward the cathode (due to the DL potential drop) and, hence, the loss of electrons from this plasma was determined by the anode fall. The existence of the anode fall was originally reported in [4], where the role of this factor in the balance of electrons in the anode plasma was pointed out. The results of measurements performed by the probe technique showed that the potential well depth

(PWD) in the anode fall is on the order of 4 V. However, limited spatial and temporal resolution of the probe technique did not allow the anode fall magnitude and dynamics to be studied in sufficient detail.

This Letter reports on the results of investigation of the PWD distribution in the anode plasma of a plasma beam with DL. The role of the anode fall in the electron density balance in the anode plasma is discussed.

Experimental. The experimental setup and the longitudinal potential distribution in the system are described in detail elsewhere [5]. A plasma beam was generated by an electric arc in mercury vapor with a liquid cathode. The beam propagated along a cylindrical quartz tube with an inner diameter of 12 cm toward a stainless steel flat disk anode. Depending on the anode current, a DL was formed at various distances from the anode. The mercury vapor pressure in the system was on the order of 10^{-5} Torr, and the magnetic field strength was ~25 G.

The depth of the anode potential well was measured with the aid of a multigrid electron energy analyzer mounted on the anode. The first grid had a cell size of 0.03 mm and was welded to the anode surface from the plasma side (the Debye length was on the order of 0.1 mm). The second grid (4 lines/mm) was biased by a retarding potential. A 20-V potential applied to the third grid accelerated electrons and repulsed ions. The fourth grid was connected to the case and both served as the collector of electrons. The analyzer was positioned at the anode center and had a circular working surface with a diameter of 3 mm.
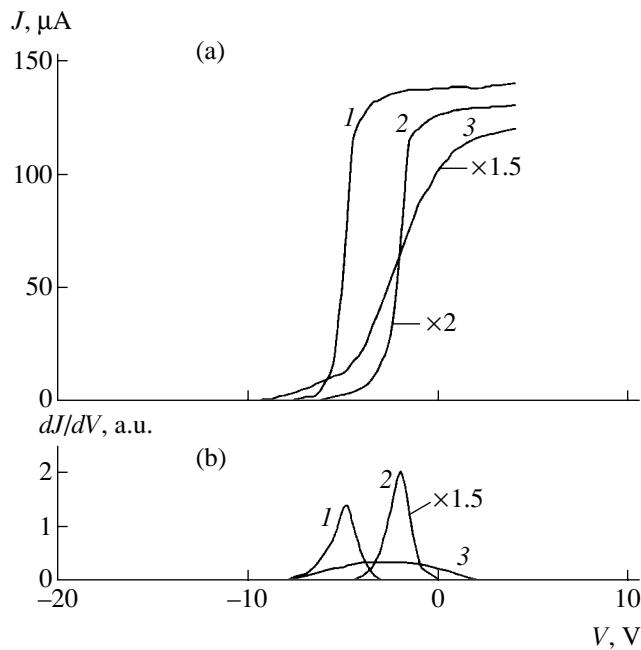
J, μA

Fig. 1. Plots of (a) the collector current and (b) its derivative for $I_a = 300$ mA and (*1*) $V_A = 4.8$, (*2*) 2 V and (*3*) the average collector current versus the second-grid potential.
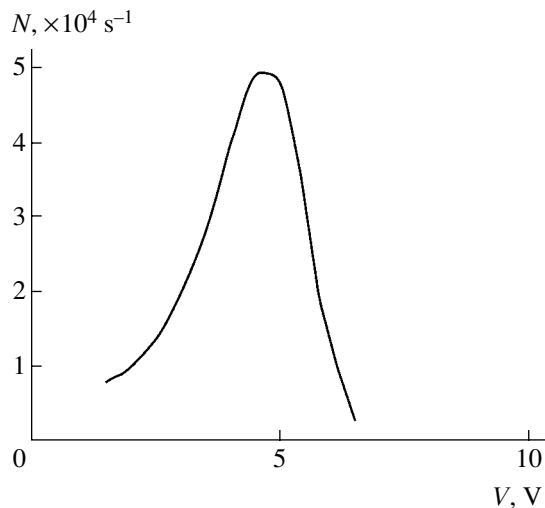
$N, \times 10^4$ s^{-1}

Fig. 2. A plot of the number of pulses measuring PWD versus potential level.

Experimental procedure and results. The PWD was determined using the results of measurements of the collector current as a function of the potential V applied to the second grid (C_2). As the magnitude of the negative retarding potential applied to C_2 decreased to a certain level, the collector current exhibited a sharp growth. The retarding potential corresponding to the current buildup determines the depth of the anode potential well. In the presence of a DL, the PWD exhibited strong fluctuations and the experimental curve was smeared, which complicated the measurements. The

fluctuating PWD was measured using a thin cylindrical probe arranged at the anode so as not to shadow the entrance of the energy analyzer. The potential oscillations detected by the isolated probe were fed to a comparison circuit. When the probe potential passed through a certain level, a 50-ns-long rectangular gate pulse was generated. This pulse opened the entrance of an accumulator, which measured the current passing through a given resistance R. Thus, by varying the retarding potential, it was possible to measure the collector current as a function of the retarding potential V. Note that these characteristics were measured when the potential passed through a certain preset level.

Figure 1a shows the typical characteristics (curves *1* and *2*) measured for two potential levels V_A. Simultaneously, the number of pulses per second was counted. It was established that, irrespective of the direction of crossing the preset potential, higher V_A values corresponded to lower collector currents and, hence, lower electron densities. Curve *3* in Fig. 1a is a plot of the average current versus the potential of the second grid. Figure 1b presents the first derivatives of the curves in Fig. 1a. The PWD was taken equal to the voltage corresponding to the maximum of the first derivative. As can be seen, the position of this maximum exhibits a significant shift, hindering the measurement of the average PWD, while the character of fluctuations cannot be determined at all.

Figure 2 shows a plot of the number of PWD readings versus the retarding potential V. As can be seen from these data, the most probable PWD value falls within 3–6 V, although sometimes this value can be much higher.

Discussion. In analyzing the electron density balance in the anode plasma, we may ignore a contribution due to the ionization caused by pair collisions. Then, the balance equation retains both the "income" term related to electrons transmitted via the DL to the anode plasma and the "loss" term due to electrons reaching the anode upon surmounting the anode fall. The equation of the average electron density balance is as follows:

$$n_D \int_{v_D}^{\infty} v f(v) dv = n_A \int_{v_A}^{\infty} v f_A(v) dv, \qquad (1)$$

where n_D and n_A are the numbers of electrons passing via the double layer potential drop (V_D) and via the anode fall V_A, respectively. The verification of formula (1) using the electron distributions f_D and f_A in the cathode and anode plasma, respectively, and the corresponding

electron densities n_D and n_A for $V_A = 4.8$ V and $V_D = 18$ V showed a satisfactory agreement between n_D/n_A values (in the order of magnitude).

REFERENCES

1. M. A. Hellberg, M. A. Raadu, and R. L. Mace, in *Proceedings of the Symposium on Double Layer Potential Formation and Related Nonlinear Phenomena in Plasmas, Sendai, 1996*, p. 3.

2. P. Carlgvist, in *Proceedings of the Symposium on Wave Instabilities in Space Plasmas, Helsinki, 1978* (Reidel, Dordrecht, 1979), p. 83.

3. L. Lindberg, in *Proceedings of the International Conference on Plasma Physics (ICPP 82), Göteborg, 1982*, p. 137.

4. S. Torvén and L. Lindberg, J. Phys. D **13**, 2285 (1980).

5. A. Kh. Muradov, Fiz. Plazmy **11**, 1386 (1985) [Sov. J. Plasma Phys. **11**, 794 (1985)].

6. H. S. Maciel and J. E. Allen, in *Proceedings of the 18th International Conference on Phenomena in Ionized Gases, 1985,* Vol. 1, p. 155.

Translated by P. Pozdeev

He–Ne/I₂ Laser on a Shock-Absorbing Base

P. S. Krylov and V. E. Privalov*

St. Petersburg State Technical University, St. Petersburg, 195251 Russia
* e-mail: vep29@bstu.spb.su
Received August 4, 2004

Abstract—A new variant of the unique spectroscopic device, a He–Ne/I₂ laser ensuring the most reproducible wavelength in the visible range among the existing analogs, is described. © *2005 Pleiades Publishing, Inc.*

The definition of the meter adopted by the Comité International des Poids et Mesures (CIPM) in 1983 has stipulated radiations of the stabilized lasers of five types as possessing the standard wavelengths (see table) [1, 2]. These values were obtained as a result of numerous international comparisons carried out in a period from 1974 to 1982 (see, e.g., review [3]). Subsequently, this work has been continued [4, 5], and the accuracy of reproduction of the radiation frequency (wavelength) of a He–Ne/CH₄ laser is now ensured to within 12–13 decimal digits and will probably reach 14 digits. However, even this is probably not a theoretical limit for a stabilized laser of this type [6]. For other lasers, the error of reproduction of the radiation frequency is presently detected in the 11th or 12th decimal digit.

Most widely used are He–Ne lasers stabilized with respect to the saturated iodine absorption (He–Ne/I₂ laser) at a wavelength of 0.6329 μm, which is the strongest transition in the visible spectrum of neon. Lasers of this type are well studied and highly reliable. The general state of the art with these lasers, as well as the domestic achievements (R&D and their commercial production in Russia) have been considered in monographs [7, 8].

In addition to lasers operating at the wavelengths indicated above, good results were also obtained using He–Ne/I₂ lasers generating at 0.5435 μm. In this case, the frequency (wavelength) reproducibility is on the level of the best standards [9] and exceeds that of the other iodine-stabilized He–Ne lasers, because the contrast of the absorption peaks of iodine in the *B–X* bands increases with decreasing wavelength. Good results were also obtained for lasers operating at 0.5939 and 0.6401 μm. Now, the task is to develop a metal vapor laser stabilized by iodine absorption [10]. Attempts have been also made to create an iodine-stabilized semiconductor laser [11]. In particular, a method proposed in [12] allows a working line in the range from 0.499 to 0.829 μm to be selected from a total of about a million candidates.

Iodine and methane by no means exhaust the list of possible absorbing media suited for stabilization of the radiation frequency of potential standard sources. For example, it was suggested to stabilize semiconductor lasers using the absorption in cesium and rubidium [13, 14]. The number of possible standard sources will probably increase: if this number is small, the intermediate frequencies have to be determined using an external interferometer (which is less precise than an optical heterodyne).

Meanwhile, investigations aimed at the development of the most widely used He–Ne/I₂ laser (0.6329 nm) have continued, and attempts have been made to stabilize the laser frequency with respect to the fifth harmonic of the reference signal [15, 16]. Should such lasers prove to be cheap, compact, and reliable, their use of at scientific research centers and high-precision processing facilities would allow the measure-

Standard frequencies of laser radiations stipulated by the definition of the meter (recommended by CIPM in 1983)

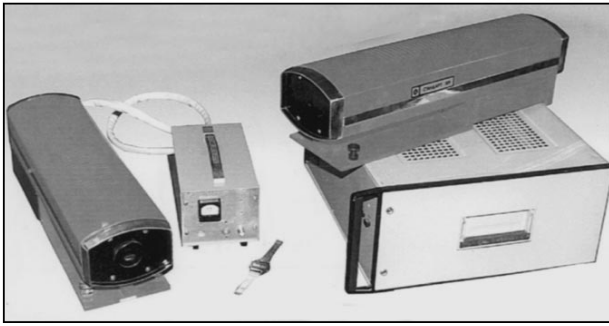| Laser	Frequency, MHz	Wavelength, μm	Uncertainty of reproduction
He–Ne/CH₄	88 376 181.608	3.3922313970	1.3×10^{-10}
He–Ne/I₂	437 612 214.8	0.6329913981	1.1×10^{-9}
He–Ne/I₂	489 880 355.1	0.6119707698	1×10^{-9}
He–Ne (2^z harmonic, 1.15 μm) or Ar/I₂ dye laser	520 206 808.61	0.57629476027	6×10^{-10}
	582 490 603.6	0.5146734662	1.3×10^{-9}

Fig. 1. He–Ne/I$_2$ lasers with power supply units.

ments to be performed on site and would eliminate the existing multistep validation system without any loss in the precision and unification of measurements.

We have developed He–Ne/I$_2$ lasers of various types (0.6329 and 0.6119 μm), some of which have been implemented in commercial production [7, 8]. One variant generated a nonmodulated radiation [17]. The prototype considered below is distinguished from the previous variant by smaller dimensions and a lower weight of the power supply unit, while retaining the metrological characteristics on the standard level. Figure 1 shows the new setup in comparison to the previous one. The new power supply unit has a volume below 2 dm^3 and a weight below 3 kg. The results of investigations showed that the new variant has a precision comparable with that of the previous setups. A prototype of this system was demonstrated at the Hanover International Fair in 1998.

The system has been continuously improved. Figure 2 shows a functional scheme of the new He–Ne/I$_2$ laser, which illustrates the operation principle and presents some details of the system. Display *19* shows a series of the absorption peaks of ^{127}I$_2$, one of which is used for frequency stabilization. Figure 3 presents the complete laser frequency spectrum in the working spectral range. Most attention is now devoted to the noise characteristics of both the generator and related electronics. The emitter design and the type and location of a photodetector are such that the problem of stability of the axis of the directivity diagram is not related to the laser frequency stabilization. This problem might arise in matching to the measuring devices. However, we have used He–Ne/I$_2$ lasers for about three decades, and this problem was encountered neither in the optical heterodyne schemes nor in the case of interferometers. Apparently, instability of the diagram axis (on the order of 2–3 minutes of arc) is below the level on which it is significant.

It should be borne in mind that the He–Ne/I$_2$ laser is a highly sensitive optical device whose parameters can be significantly influenced by vibrations of the base. Therefore, the base is an important part of the system.
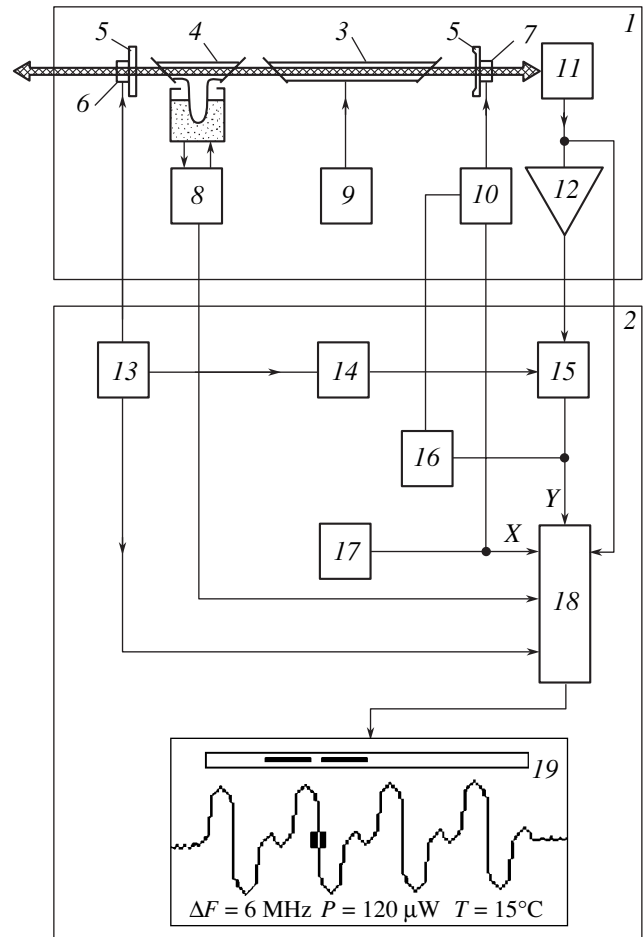
Fig. 2. Schematic diagram of the spectroscopic setup: (*1*) He–Ne/I$_2$ laser unit; (*2*) AFC unit; (*3*) active element; (*4*) absorbing cell; (*5*) mirrors; (*6*) piezoelectric modulator; (*7*) piezoelectric corrector; (*8*) stabilizer of the temperature of the absorbing cell finger; (*9*) high-voltage power supply; (*10*) dc amplifier; (*11*) photodetector; (*12*) lock-in amplifier; (*13*) *f* generator; (*14*) 3*f* generator; (*15*) lock-in detector; (*16*) intermediate pulse control; (*17*) digital ramp generator; (*18*) microprocessor; (*19*) display.
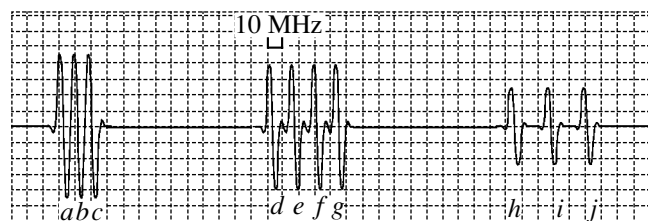

Fig. 3. Laser frequency spectrum: λ_a = 0.632990997 μm; λ_b = 0.632991009 μm; λ_c = 0.632991020 μm; λ_d = 0.632991177 μm; λ_e = 0.632991198 μm; λ_f = 0.632991213 μm; λ_g = 0.632991230 μm; λ_h = 0.632991369 μm; λ_i = 0.632991398 μm (ν_i = 473612214.8 MHz); λ_j = 0.632991427 μm.
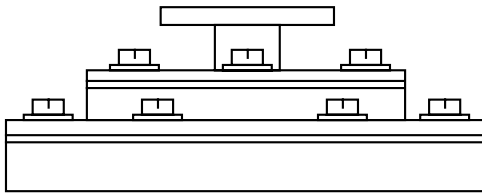
Fig. 4. Schematic diagram of a shock-absorbing base.

It was demonstrated (see, e.g., [18]) that modulation of the discharge current or the laser cavity length at frequencies close to (or multiples of) that of the master oscillator of the automatic frequency control (AFC) system (*f* generator *13* in Fig. 2) leads to a shift of the He–Ne/I_2 laser frequency and may even break the AFC system operation. Vibrations of the laser base produce modulation of the cavity length and decrease the stability and reproducibility of the laser frequency. Estimates show that the ultimate precision (minimum error) in the frequency reproducibility of the given laser (to within twelve decimal digits) can be reached provided that the shock-absorbing system decreases the amplitude of vibrations by two orders of magnitude in the frequency range from several hertz to several kilohertz.

As is known [19], the square of the fundamental frequency of a mechanical system is proportional to the stiffness and inversely proportional to the mass. In order to suppress undesired vibrations, a setup is usually made heavy (with a weight of up to several hundred kilograms or even a ton) and either mounted on elastic supports or suspended on elastic springs. The aim is to shift the fundamental frequency out of the spectral range of external vibrations (extending from 10 Hz to 20 kHz)—namely, to decrease the fundamental frequency to a minimum level, because increasing it above the upper boundary of the vibration spectrum for such a big weight is impossible. However, an alternative solution consists in creating shock absorbers of zero stiffness [20], which makes it possible to reduce the fundamental frequency to 1 Hz and below at a system weight on the order of tens of kilograms. We have also created a shock absorber of this kind representing a vacuum shock-absorbing support [21].

The principle of operation of the vacuum support ensures an effective decrease in the dependence of the stiffness of elastic structural elements on a static load. The stiffness of the support is determined by the design of elastic elements of the vacuum joint, which can be decreased to a sufficiently low level. The optimum solution is to mount the protected object on a platform based on four vacuum supports. Each support (Fig. 4) has the form of a disk with a diameter from 100 to 250 mm (weighing from 2 to 5 kg), which has a nominal load capacity from 80 to 500 kg. The support is 110 mm in height and has a rod with a plate for mounting the platform. The number of supports in a system

can be increased to eight and above, depending on the static load. The uniform loading of supports is achieved with the aid of additional balance loads, which is quite a simple task in a system with four supports. The principle of shock absorption in such systems is described elsewhere [22].

The shock-absorbing base includes a distribution system of vacuum pipes, a vacuum system control unit, a small mechanical vacuum pump (3NVR-3D), and a mechanical lock used in the switch-off state. The system reaches a float-up state 1 min after switching on the vacuum pump. Repeated switch-on of the pump is required with a period of several hours, depending on the quality of vacuum seals.

The fundamental frequencies of vibrations in the vertical and horizontal planes of a shock-absorbing system with a weight capacity of 500 kg (comprising four 125-kg supports) were measured using an external pulsed perturbation and found to be below 0.81 and 2 Hz, respectively. As a result, the system decreases the amplitude of vibrations in the frequency range from 4 Hz to 5 kHz by approximately two orders of magnitude and provides conditions for reaching the ultimate metrological characteristics of the He–Ne/I_2 laser described above. Our laser has been successfully used with such shock-absorbing supports for validation of the metrological characteristics of commercial lasers of the LGN-302 [23] and LGN-303 [24] types (neither the He–Ne/I_2 laser features nor the shock-absorbing supports were mentioned in these communications).

REFERENCES

1. *Documents Concerning the New Definition of the Meter*, Metrologiya **19**, 163 (1983).

2. V. E. Privalov, *Quantum Electronics and the New Definition of the Meter* (Leningrad, 1987) [in Russian].

3. V. P. Kapralov and V. E. Privalov, Opt. Spektrosk. **55**, 1101 (1983) [Opt. Spectrosc. **55**, 671 (1983)].

4. J.-M. Chartier, L. Robertson, and S. Fredin-Pacard, IEEE Trans. Image Process **20**, 181 (1991).

5. J. Hu, E. Ikonen, and K. Riski, Metrologiya **33**, 467 (1996).

6. S. N. Bagaev and V. P. Chebotaev, Usp. Fiz. Nauk **148**, 143 (1986) [Sov. Phys. Usp. **29**, 82 (1986)].

7. V. E. Privalov, *Gas-Discharge Lasers in Measuring Facilities* (Sudostroenie, Leningrad, 1989) [in Russian].

8. V. A. Ivanov and V. E. Privalov, *Application of Lasers in Precision-Mechanics Devices* (Politekhnika, St. Petersburg, 1993) [in Russian].

9. U. Brand, Opt. Commun. **100**, 361 (1993).

10. V. E. Privalov, J. Mosc. Phys. Soc. **7**, 335 (1997).

11. Ludvigsen, Dissertation (Espoo, 1994).

12. V. E. Privalov and S. K. Savelyev, Proc. SPIE **3687**, 2 (1999).

13. *Highly Coherent Small-Size Tunable Lasers. Laser Optics* (FIAN, St. Petersburg, 1998) [in Russian].

14. *Rb-Stabilized Diode Laser for Length Measurements* (PTB, Braunschweig-Berlin, 1998).

15. A. V. Mironov, Candidate's Dissertation (Leningrad State University, Leningrad, 1989).

16. J. Hu, T. Ahola, E. Ikonen, and K. Riski, IEEE Trans. Image Process **46**, 186 (1997).

17. P. S. Krylov, A. V. Mironov, and V. E. Privalov, Prib. Tekh. Éksp., No. 4, 197 (1989).

18. P. S. Krylov and V. E. Privalov, Radiotekh. Élektron. (Moscow) **32**, 587 (1987).

19. A. A. Andronov, A. A. Vitt, and S. E. Khaikin, *Theory of Oscillators* (Fizmatgiz, Moscow, 1959; Pergamon Press, Oxford, 1966).

20. USSR Inventor's Certificate No. 1155803; Byull. Izobret., No. 18 (1985).

21. RF Patent No. 2066799; Byull. Izobret., No. 26 (1996).

22. P. S. Krylov and V. E. Privalov, Prib. Tekh. Éksp., No. 6, 135 (1998).

23. V. P. Kapralov and V. E. Privalov, Opt. Spektrosk. **84**, 518 (1998) [Opt. Spectrosc. **84**, 458 (1998)].

24. A. N. Vlasov, V. E. Privalov, and P. S. Krylov, Proc. SPIE **4680**, 52 (2002).

Translated by P. Pozdeev

Shape Memory Effect in Porous Volume NiTi Articles Fabricated by Selective Laser Sintering

I. V. Shishkovsky

Samara State Technical University, Samara, Russia
e-mail: shiv@fian.smr.ru
Received July 23, 2004

Abstract—The shape memory effect in porous nickel titanium (NiTi) articles obtained by means of layered synthesis using selective laser sintering (SLS) technology was studied by measuring the temperature dependence of the electric resistivity of the material. For the porous NiTi samples synthesized from Ni and Ti powders, the interval of probable appearance of the shape memory effect falls within the temperature interval from –50 to 0°C. In a porous material synthesized by laser sintering from a commercial NiTi powder of the PV N55T45 grade, this effect falls in the interval from +25 to +50°C. Prospects for the use of porous NiTi articles as medicinal implants are discussed. © 2005 Pleiades Publishing, Inc.

Introduction. Nickel–titanium (NiTi) alloys are promising materials for medicinal implants, which is related to their high biocompatibility, specific strength, corrosion resistance, and load damping properties, as well as to the unique properties known as the shape memory effect. The latter effect, observed in both solid and porous NiTi alloys [1], is explained by thermoelastic martensite transformations taking place in these materials. The structural, thermal, and mechanical properties of porous NiTi materials in comparison to the analogous cast alloys have been extensively studied by researchers of the well-known school at the Tomsk State University [1, 4, 5]. In particular, it was established that doping (leading to deviations from the stoichiometric NiTi composition) influences the sequence of structural and phase transformations in porous NiTi [6].

Previously, it was demonstrated that NiTi articles can be synthesized by means of self-propagating high-temperature synthesis (SHS) in the laser radiation controlled regime [2]. It was also shown that layer-by-layer formation of volume articles possessing any preset shape is possible by means of the selective laser sintering (SLS) technology [3]. This study, based on the previous results [2, 3] and the data reported in [4–6], was devoted to monitoring of the features of SLS-synthesized intermetallic NiTi articles by measuring the electric resistivity of the material. It is suggested that this method (justified and illustrated in [4, 5, 7]) can be used to reveal the shape memory effect in porous NiTi articles obtained by laser synthesis.

Experimental. The shape memory effect was studied in monolayer samples sintered using a Kvant-60 technological laser setup. Laser radiation was focused in a spot with a diameter of $D \sim 100$ μm. The laser output power P was measured by a TI-4 power meter and controlled in the range from 2 to 20 W. The laser beam was scanned at a velocity v, which could be varied within broad limits. The laser sintering was effected by meander scans over the surface of a NiTi powder freely delivered into a special chamber filled with argon. The experimental setup, the SLS process, and the optimum regimes of NiTi sintering are describes elsewhere [2, 3].

The NiTi synthesis in the regime of the controlled exothermal burning reaction was performed using powdered titanium (PTOM grade) and a powdered nickel-based cladding composition (PGSR4 grade, 80% Ni and 20% of cladding additives). For comparison, the same technological scheme was used for the laser sintering (without synthesis) of monolayers of a commercial NiTi powder of the PV N55T45 grade (Polema Co., Tula). The particle size in the initial powders was ~100 μm (as monitored by sieving analysis), which was comparable with the laser spot diameter. The laser sintering led to the formation of flat monolayer samples with dimensions $\sim 10 \times 30 \times d$ mm, where d is the sintered layer thickness. The dimensions of sintered samples were measured by slide calipers.

The electric resistivity of the laser-sintered samples was determined from a voltage drop measured by a potentiometric technique. The temperature was measured using chromel–copel thermocouples. The conducting leads used in the electric measurements had small resistances. These leads, as well as the thermocouple wires, were laser-spot-welded to the rough sample surface. The total relative error of the resistivity measurements was 6–7%, and the tolerated error of the thermocouple readings was about ±0.2 mV.

The parameters of laser processing regimes used for the NiTi sample preparation using the combined SHS–SLS process and the laser sintering of a commercial intermetallic powder are listed in the table. The last column in this table gives the deposited laser energy,

defined as $A = PD/(Dv\Delta)$, where Δ is the laser scan step (in this study, $\Delta = D$). Thus, the physical meaning of A [J/cm^2] is the surface energy density of the laser action. As can be seen, an increase in the laser energy deposited in the powder leads to a greater thickness of the sintered layer. However, very large A values lead to deformation of the sintered layers (data for these non-optimum regimes are not presented), which hinders the formation of volume articles without delamination of sequential layers. It should be noted that the thicknesses of sintered layers in the commercial NiTi powder (PV N55T45) in the bottom part of the table are generally somewhat lower as compared to the values obtained for the Ni–Ti powder mixture even at much higher deposited energies. This is related to the fact that the SLS process in the Ni–Ti powder mixture involved an exothermal burning reaction leading to the SHS of an intermetallic NiTi phase [2]. The additional energy deposition due to this exothermal reaction led to an increase in the sintered layer thickness. On the other hand, we failed to select parameters of the controlled SHS–SLS process [2] so as to provide for a 100% yield of NiTi (even upon an additional annealing of the articles). The laser-sintered samples always contained some other intermetallic phases, including Ni_3Ti, $NiTi_3$, $NiTi_2$, and/or the initial components (Ni, Ti).

Results and discussion. Figures 1a–1c show the results of measurements of the resistivity ρ [$\mu\Omega$ cm] in a temperature range from –100 to +100°C. The measuring system was verified by measuring ρ of cast NiTi wires with a diameter of 1.8 and 0.5 mm (Fig. 1a). All samples were measured in the heating (from –100 to +100°C) and cooling (from +100 to –100°C) modes (in Fig. 1, the results of these measurements are represented by filled and open symbols, respectively). For the 0.5-mm cast wire, the resistivity value corresponds to the reference data and the behavior of the $\rho(T)$ curve agrees with that reported in the literature (see, e.g., [1, Fig. 2.35]). Indeed, the resistivity curve measured in the heating mode exhibits a peak in the region of the austenite transformation; a peak observed in the cooling mode reflects a transition from the high-temperature phase B19 to the low-temperature phase B2. This region probably corresponds to the shape memory effect in the cast NiTi wire.

Figures 1b and 1c show the results of measurements performed on the porous layers of synthesized and commercial NiTi, respectively, processed in various regimes described in the table. For the other regimes (presented in the table and not illustrated in Figs. 1b and 1c), the $\rho(T)$ curves were completely (or nearly) monotonic, which was evidence of the absence (or very small level) of structural and phase transitions in such materials. It should be noted that such monotonic $\rho(T)$ curves were mostly typical of the processing regimes with relatively low deposited laser energies.

The first result revealed by an analysis of the data in Figs. 1b and 1c is that the intervals of the austenite and

Parameters of laser processing regimes

Regime No.	Laser power P, W	Laser beam scan velocity v, cm/s	Sintering depth d, mm	Deposited laser energy A, J/cm^2
Combined SHS–SLS of NiTi from Ni–Ti powder mixture				
1	11.7	5.7	0.12	103.05
4	13.9	5.7	0.13	122.42
7	15.7	5.7	0.14	138.28
2	11.7	3.8	0.17	154.57
5	13.9	3.8	0.19	183.63
8	15.7	3.8	0.22	207.41
3	11.7	2.8	0.23	206.1
6	13.9	2.8	0.25	244.85
9	15.7	2.8	0.28	276.56
Laser sintering of commercial NiTi powder (PV N55T45, Polema Co., Tula)				
10	13	2.3	0.11	286.24
11	13	1.9	0.12	343.5
12	13	1.4	0.14	457.97
13	13.9	2.3	0.14	306.06
14	13.9	1.9	0.14	367.28
15	13.9	1.4	0.15	489.68
16	15.7	2.3	0.14	345.7
17	15.7	1.9	0.14	414.84
18	15.7	1.4	0.16	553.09

martensite transformations in porous samples are significantly shifted and broadened compared to those in the cast NiTi. This peculiarity was also pointed out in [4, 5]. For porous NiTi samples obtained by sintering of the PV N55T45 powder and synthesized by the SHS–SLS of the Ni–Ti powder mixture, the ρ values are ~20 and ~40 times the resistivity of the cast material, respectively. Since our synthesized NiTi samples may contain some other intermetallic phases [2] (see also the data [7] concerning the effect of dopants on the temperature dependence of the resistivity), the values of the resistivity in Fig. 1b differ more significantly than those in Fig. 1c from data for the cast NiTi wires (Fig. 1a). In addition, a comparison of Figs. 1b and 1c shows that the intervals of the structural and phase transitions in the samples obtained by sintering of the commercial NiTi powder shift toward positive temperatures. In contrast, in the samples synthesized from Ni and Ti powders, these intervals shift toward negative temperatures.

Finally, it should be noted that the presence of the shape memory effect in the porous NiTi monolayers
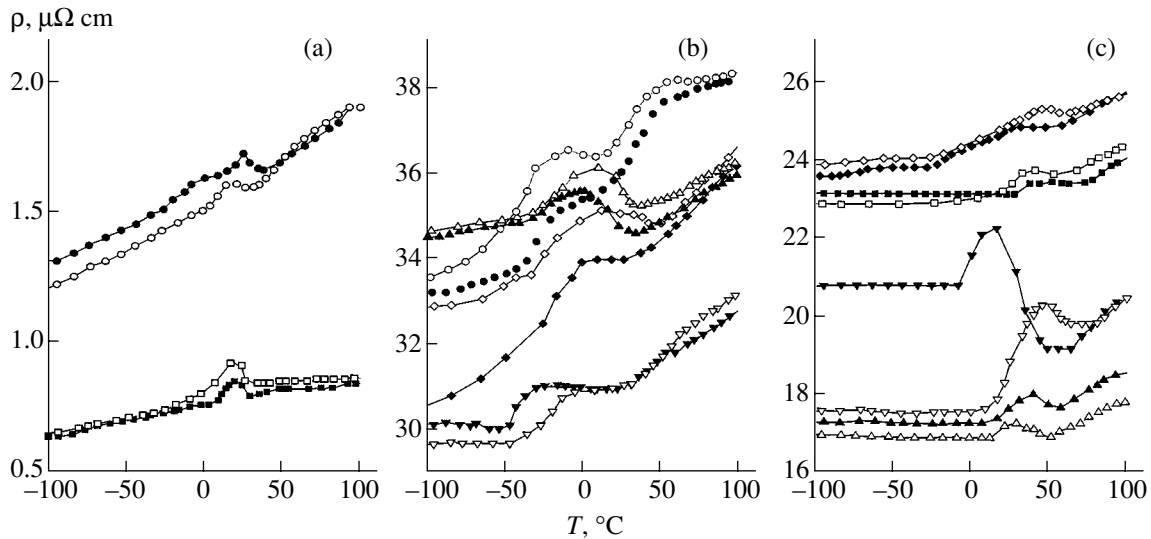
$\rho,\ \mu\Omega$ cm

Fig. 1. Temperature dependences of the resistivity ρ of NiTi samples: (a) cast wire with a diameter of (●) 1.8 and (■) 0.5 mm; (b) porous NiTi monolayers obtained by SHS–SLS of a Ni–Ti powder mixture in regimes (●) 5, (▲) 8, (◆) 9, and (▼) 3; (c) porous NiTi monolayers obtained by SLS of the commercial NiTi powder (PV N55T45) in regimes (◆) 16, (■) 17, (▼) 12, and (▲) 18. Filled and open symbols show the results of measurements performed in the sample heating and cooling modes, respectively.

studied cannot be unambiguously judged based only on the analysis of $\rho = \rho(T, A)$ curves in Figs. 1b and 1c. These data have to be complemented by the results of additional (e.g., X-ray diffraction or mechanical) investigations. However, relying on previous experience [1] and on the methods of analysis of the temperature dependence of the resistivity [7], we may nevertheless use the data presented in Figs. 1b and 1c to reveal the temperature intervals where the appearance of the shape memory effect is most probable. For the porous NiTi samples synthesized in this study (Fig. 1b), the curves measured in the cooling mode suggest that the shape memory effect is probable in the temperature interval from –50 to 0°C. For the porous NiTi samples laser-sintered from the commercial PV N55T45 powder, this most probably takes place in the interval from +25 to +50°C.

To summarize, we have presented and discussed the results of investigations of the temperature dependence of the resistivity, $\rho = \rho(T)$, which show that there are temperature intervals where the laser-sintered porous NiTi monolayers probably exhibit the shape memory effect. The existence of this effect in porous NiTi alloys synthesized layer-by-layer using the SLS technology and in three-dimensional articles of any preset shape (bioMEMS: sensors, clamps, implants) based on these materials will ensure the attainment of a qualitatively new level in orthopedics, by using prostheses with elements capable of self-acting, self-fixing, and self-unfolding at the temperature of the living organism. The porosity may be an additional positive factor

favoring the growth of soft tissues into the implant, thus increasing the biocompatibility and accelerating the healing process [3].

REFERENCES

1. *Medical Materials and Implants with Shape Memory: Collection of Scientific Works of the Institute of Medical Materials and Shape-Memory Implants*, Ed. by V. E. Gunter (Tomsk State University, Tomsk, 1988) [in Russian].

2. D. M. Gureev, O. G. Emelina, L. V. Zhuravel', *et al.*, Fiz. Met. Metalloved. **93**, 80 (2002).

3. D. M. Gureev, A. L. Petrov, and I. V. Shishkovskiĭ, RF Patent No. 2218242 (2003).

4. V. E. Gyunter, Yu. F. Yasenchuk, A. A. Klopotov, and V. N. Khodorenko, Pis'ma Zh. Tekh. Fiz. **26** (1), 71 (2000) [Tech. Phys. Lett. **26**, 35 (2000)].

5. V. N. Khodorenko, V. E. Gyunter, A. N. Monogenov, and Yu. F. Yasenchuk, Pis'ma Zh. Tekh. Fiz. **27** (22), 80 (2001) [Tech. Phys. Lett. **27**, 970 (2001)].

6. A. A. Klopotov, V. E. Gyunter, T. L. Chekalkin, and E. V. Kozlov, Pis'ma Zh. Tekh. Fiz. **28** (19), 17 (2002) [Tech. Phys. Lett. **28**, 803 (2002)].

7. *Physical Metallurgy*, Ed. by R. W. Cahn and P. Haasen (North Holland Physics, Amsterdam, 1983), Vol. 1.

Translated by P. Pozdeev

Metal Oxide Bicrystal Josephson Junctions of a New Type with High Critical Parameters

I. M. Kotelyanskiĭ*, I. V. Borisenko, A. V. Shadrin, G. A. Ovsyannikov, V. A. Luzanov, and F. V. Komissinskiĭ

Institute of Radio Engineering and Electronics, Russian Academy of Sciences, Moscow, 103907 Russia
Chalmers University of Technology, 41296, Göteborg, Sweden
* e-mail: imk216@ire216.msk.su
Received September 28, 2004

Abstract—Film bicrystal Josephson junctions of a new type based on a metal oxide high-T_c superconductor of the $YBa_2Cu_3O_{7-x}$ (YBCO) system are suggested and studied. In junctions of the new type, in contrast to the known ones, the working surfaces situated on the opposite sides of the bicrystal interface have different crystal orientations: one is (001)YBCO, and the other is rotated (misoriented) relative to it by an asymmetric bicrystal angle around a certain axis lying in the substrate plane. The main electrical and dynamic (microwave) characteristics have been determined for junctions of the new type based on $NdGaO_3$ bicrystal substrates with the misorientation angle varying from 13° to 28°. These junctions exhibit high values of the critical parameters at $T = 77$ K, including the critical current density $I_C = (2–5) \times 10^5$ A/cm^2 and the characteristic voltage $V_C = I_C R_N = 0.6–0.9$ mV. Advantages of the bicrystal Josephson junctions of the new type over the known junctions are considered. © 2005 Pleiades Publishing, Inc.

According to the existing models of the bicrystal Josephson junction [1–3], relatively large values of the superconducting order parameter in metal oxide superconductors create prerequisites for the formation of junctions with high values of characteristic voltage (up to several millivolts at $T = 77$ K). As is known, this voltage determines the signal and noise parameters of the Josephson devices. However, metal oxide bicrystal junctions of the well-known (and the only practically used) type based on $YBa_2Cu_3O_{7-x}$ (YBCO) show the real values of V_C at $T = 77$ K not exceeding 300 μV [4]. In the junctions of this type, the working surfaces situated on the opposite sides of the bicrystal interface have the same orientation (001)YBCO and are misoriented by a symmetric bicrystal angle around the [001]YBCO axis (Fig. 1a). A characteristic feature of the junctions of this type is that the misoriented (001)YBCO surfaces occur in the same plane, so that we deal with a planar bicrystal junction (PBJ).

Recently, it was experimentally demonstrated [5, 6] that V_C in bicrystal Josephson junctions with (001)YBCO surfaces also misoriented by a symmetric bicrystal angle, but around the [100]YBCO axis lying in the substrate plane (Fig. 1b), may reach 1.2 mV at $T = 77$ K. Orientations of the working bicrystal surfaces in these junctions are also the same, albeit different from (001)YBCO. Since the (001)YBCO planes in the junctions of this type make a bicrystal angle with each other, the structure is called a tilted bicrystal junction (TBJ) [5]. Unfortunately, the junctions of this type have a significant disadvantage related to the anisotro-

pic electric properties of the working surfaces, which leads to difficulties in the creation of a preset topology of the electric chain involving superconducting electrodes and Josephson microbridges (e.g., the quantization circuits in SQUIDs).

This paper describes film bicrystal Josephson junctions of a new type based on a metal oxide high-T_c
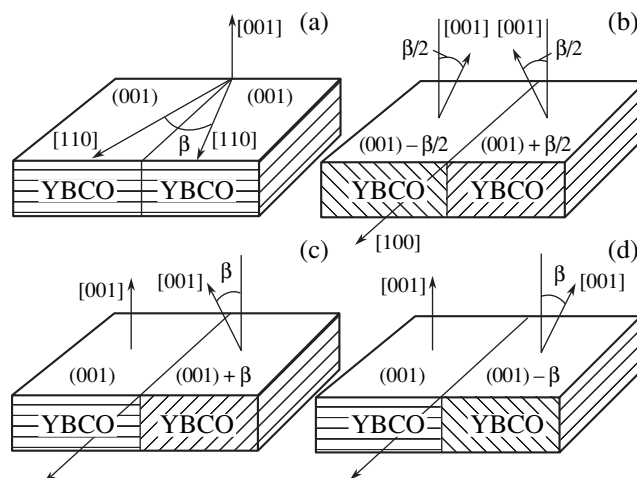

Fig. 1. Schematic diagram showing bicrystal Josephson junctions of various types: (a) planar bicrystal junction (PBJ); (b) tilted bicrystal junction (TBJ) with symmetric misorientation angle; (c, d) tilted asymmetric bicrystal junction (TABJ) with asymmetric bicrystal angles $+\beta$ and $-\beta$, respectively.

Electric parameters of planar (PBJ) and tilted symmetric (TBJ) and asymmetric (TABJ) bicrystal Josephson junctions

Junction type	Bicrystal angle β	Sample No.	$T = 77$ K			$T = 4.2$ K		
			I_C, mA	R_N, Ω	V_C, mV	I_C, mA	R_N, Ω	V_C, mV
PBJ	24°	J1	0.035	0.9	0.032	1.6	0.9	1.4
		J2	0.047	2.1	0.1	1.7	1.9	3.2
		J3	0.065	0.5	0.032	3.7	0.6	2.2
PBJ	28°	J1	0.017	4.4	0.075	–	–	–
		J2	0.012	2.0	0.050	–	–	–
		J3	0.012	2.8	0.033	–	–	–
TBJ	22°	J1	1.25	0.54	0.67	–	–	–
		J2	1.5	0.60	0.90	11	0.6	6.6
		J3	1.5	0.46	0.69	10	0.6	6.0
TBJ	28°	J1	0.11	2.5	0.28	–	–	–
		J2	0.24	1.3	0.31	–	–	–
		J3	0.075	4.5	0.34	–	–	–
TABJ	21°	J1	2.6	0.33	0.87	–	–	–
		J2	1.71	0.4	0.68	–	–	–
		J3	1.5	0.41	0.69	–	–	–
TABJ	28°	J1	0.49	1.64	0.80	4.0	0.7	2.8
		J2	0.26	1.04	0.27	4.1	0.5	2.1
		J3	0.1	1.92	0.19	2.2	1.8	4.0

superconductor of the YBCO system and characterizes the main parameters of this junction.

In contrast to the known junctions of the types described above, the working surfaces situated on the opposite sides of the bicrystal interface of the proposed junction have different crystal orientations: one is (001)YBCO, and the other is rotated (misoriented) relative to it by an asymmetric bicrystal angle around a certain axis lying in the substrate plane (Figs. 1c and 1d). By analogy with the junction described in [5], the new type will be referred to as a tilted asymmetric bicrystal junction (TABJ).

In order to assess the prospects of using tilted asymmetric bicrystal Josephson junctions, we have studied their main electrical and dynamic (microwave) characteristics for various values of the bicrystal angle. In order to provide for an objective judgment, we have also prepared and characterized samples of junctions of the known types with symmetric (planar and tilted) misorientations. The junctions of all three types were prepared using the same technology, based on the (001)YBCO films grown on the corresponding NdGaO$_3$ bicrystal substrates with the misorientation angles β varying from 13° to 28°. The substrates for all junctions were also grown using the same technology [7] and had bicrystal interfaces of almost identical quality. The tilted junctions of both type were misoriented relative to the [100]YBCO axis.

The metal oxide high-T_c superconductor YBCO films with a thickness of 150 nm were deposited by means of the dc cathode sputtering of a stoichiometric YBCO target in oxygen at a pressure of 300–400 Pa. The films were deposited onto substrates heated to 780–800°C and then cooled to room temperature for 1.5 h in the oxygen atmosphere. The obtained heteroepitaxial YBCO films had critical temperatures within $T_C = 87$–89 K. The Josephson bridges across the bicrystal interface had a width of 4 μm and a length of 10 μm and were formed by high-frequency plasma etching in argon, followed by chemical etching in a 0.5% bromine solution in ethanol [8].

The current–voltage (*I–V*) curves were measured at various temperatures in the range from 4.2 to 77 K. The measurements were performed either in the absence of a magnetic field and in a field of up to 100 Oe or on the samples exposed to a monochromatic electromagnetic radiation with a frequency from 30 to 100 GHz. In order to decrease the influence of uncontrolled external fields, the investigation was performed in a screened room, with filtration of all signals in the leads connected to a sample.

The results of determination of the electric parameters of the Josephson junctions of the three types are summarized in the table. As can be seen from these data, the tilted junctions with both symmetric and asymmetric bicrystal angles possess (for the same cross

section areas) significantly (tenfold) higher critical parameters at $T = 77$ K as compared to those for the planar junctions. The critical current densities of the tilted junctions are $I_C = (2–5) \times 10^5$ A/cm^2, and their characteristic voltages are $V_C = I_C R_N = 0.6–0.9$ mV.

Figure 2 shows the $I–V$ curves of the tilted asymmetric junctions with the bicrystal angles $\beta = 21°$ and $28°$. Both curves correspond to a hyperbolic dependence and are analogous to the $I–V$ of the tilted junctions with symmetric bicrystal angles. As is known [8, 9], this dependence is characteristic of a resistive model of the Josephson junction with two channels of the charge transfer: via the current of quasiparticles (V/R_N) and the superconducting current $I_S(\varphi) = I_C \sin\varphi$. It should be noted that the tilted junctions with asymmetric misorientation (as well as the known junctions of two types with symmetric misorientation) for $\beta < 19°$ exhibit nonhyperbolic $I–V$ curves typical of a viscous vortex flow [9]. When the misorientation angle increases above $21°$, the tilted junctions with asymmetric misorientation show a decrease in I_C. The inset in Fig. 2 shows the $I–V$ curves plotted on a greater scale with respect to the voltage. As can be seen, the junction with $\beta = 21°$ exhibits an increase in the resistance upon an eightfold growth in the current density, which is most probably related to the breakage of the superconducting state in the current leads. Thus, the working range of this junction is determined by the relations $I_C < I < 8I_C$.

In the tilted asymmetric junction, the critical current I_C was maximum at a zero applied magnetic field strength and exhibited a nonmonotonic decrease with increasing field, which is analogous to the behavior known for the distributed Josephson junctions [9]. The $I–V$ curves of such junctions exposed to a monochromatic electromagnetic radiation in the millimeter wavelength range, $A\sin(2\pi f_c t)$ with $f_c = 56$ GHz, showed a good agreement between the characteristics measured in the dynamic regime and in the dc mode at $T = 77$ K. A decrease in the temperature gives rise to the excess current and leads to deviation from the resistive model.

The results of our investigations of the main parameters of the bicrystal junctions of the new type indicate that it is possible to obtain Josephson junctions with high critical parameters at $T = 77$ K, $I_C = (2–5) \times 10^5$ A/cm^2 and $V_C = I_C R_N = 0.6–0.9$ mV, which is evidence of good prospects for their use in both microwave and low-frequency superconducting electronics.

It should be noted that bicrystal junctions of the tilted asymmetric type are free of the main disadvantages inherent in the known types. As was demonstrated above, the new junctions provide much better critical parameters at $T = 77$ K as compared to those of the planar junctions. In contrast to the tilted symmetric junctions, one of the working surfaces in the asymmetric junction is a practically isotropic (001)YBCO plane, on which additional elements of the Josephson devices
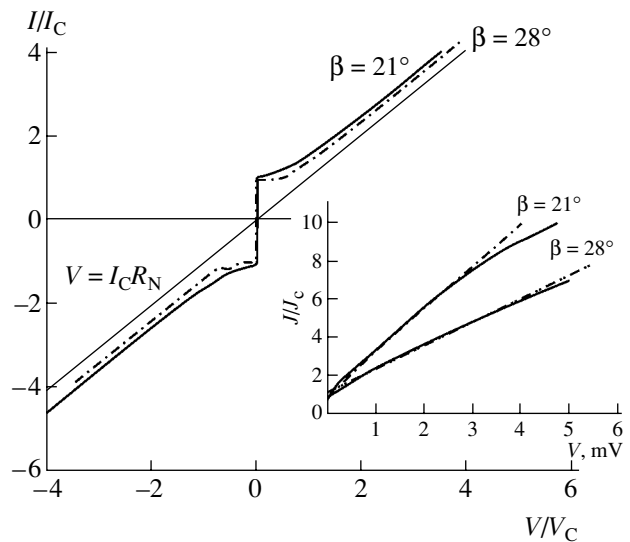

Fig. 2. Typical $I–V$ curves of the tilted asymmetric bicrystal junctions with the misorientation angles $\beta = 21°$ and $28°$ at $T = 77$ K. Thin solid line corresponds to the ohmic behavior. The inset plots the $J–V$ curves on a greater scale with respect to the voltage; dashed lines show the asymptotic behavior of the linear components.

(filters, antennas, voltage control schemes, etc.) can be readily fabricated.

In addition, Josephson junctions of the proposed type can be obtained not only on the bicrystal substrates but on the usual substrates of the so-called biepitaxial configuration as well. This can be achieved by selecting appropriate materials of the dielectric sublayer(s) and substrate and finding the optimum substrate orientation by using the known criteria of mutual orientations for heteroepitaxy (see, e.g., [10]). Despite numerous investigations, only biepitaxial Josephson junctions with one fixed value of the bicrystal angle (45°, which is far from the optimum [11]) have been obtained and characterized so far. According to our estimates, bicrystal junctions of the tilted asymmetric type in biepitaxial configuration can be obtained with a misorientation angle different from 45° and approaching the optimum value. The latter circumstance is extremely important for opening the way to the creation of biepitaxial bicrystal Josephson junctions with high critical parameters based on metal oxide high-T_c superconductors.

REFERENCES

1. R. A. Riedel and P. F. Bagwell, Phys. Rev. B **57**, 6084 (1998).

2. Yu. S. Barash, Phys. Rev. B **61**, 678 (2000).

3. Y. Tanaka and S. Kashiwaya, Phys. Rev. B **53**, R11957 (1996).

4. L. R. Vale, R. H. Ono, and D. A. Rudman, IEEE Trans. Appl. Supercond. **7**, 3193 (1997).

5. U. Poppe, Y. Y. Divin, M. I. Faley, *et al.*, IEEE Trans. Appl. Supercond. **11**, 3768 (2001).

6. Y. Y. Divin, I. M. Kotelyanski, P. M. Shadrin, *et al.*, in *Proceedings of the 6th European Conference on Applied Superconductivity, Sorrento, 2003*, p. 166.

7. Yu. Ya. Divin, I. M. Kotelyanskiĭ, and V. N. Gubankov, Radiotekh. Élektron. (Moscow) **48**, 1238 (2003).

8. G. A. Ovsyannikov, I. V. Borisenko, K. I. Konstantinyan, *et al.*, Pis'ma Zh. Tekh. Fiz. **25** (11), 65 (1999) [Tech. Phys. Lett. **25**, 913 (1999)].

9. K. K. Likharev, Rev. Mod. Phys. **51**, 101 (1979).

10. L. S. Palatnik and I. I. Papirov, *Epitaxial Films* (Nauka, Moscow, 1971) [in Russian].

11. F. Tafuri, F. Carillo, F. Lombardi, *et al.*, Supercond. Sci. Technol. **12**, 1007 (1999).

Translated by P. Pozdeev

Autosoliton in a Structurally Unstable Crystal

E. E. Slyadnikov

*Department for Informatics Problems, Tomsk Scientific Center, Siberian Division, Russian Academy of Sciences,
Tomsk, Russia*
e-mail: slyad@cc.tpu.edu.ru
Received September 21, 2004

Abstract—It is shown that a spatially localized collective excitation of the atomic sublattice (autosoliton) appears and propagates in a structurally unstable crystal occurring in a pretransition state. The autosoliton, on the one hand, is a structural defect comprising two interphase boundaries separated by the second phase, and, on the other hand, it can be considered as a pulse of the inelastic strain field. © 2005 Pleiades Publishing, Inc.

It was experimentally demonstrated that crystals featuring the martensite transformation or occurring in a strained state are susceptible to the formation of structural defects comprising two interphase boundaries separated by the second phase [1, 2]. This implies that, in addition to the structural states of the initial crystal lattice, allowed structural states of another lattice appear in the space of interstitial sites of the crystal [3] in the presence of a variable external factor (temperature, mechanical load).

Recently, it was shown within the framework of a model of the quantum system of pseudospins [4, 5] that a spatially localized collective excitation of the crystal sublattice (soliton) appears and propagates in a structurally unstable crystal occurring in a pretransition state. This soliton is, on the one hand, a structural defect consisting of two interphase boundaries separated by the second phase, and, on the other hand, it can be considered as a pulse of the elastic strain field. A necessary condition for the excitation of solitons in structurally unstable crystals is the presence of an undamped soft mode. However, soft modes in the vicinity of a structural transition are usually overdamped [5], and, hence, the excitation of solitons is impossible. For this reason, it was expedient to study the possibility that spatially localized collective excitations of the crystal lattice—autosolitons—can appear in the vicinity of a phase transition. This paper presents a solution of this problem.

Consider a loaded crystal featuring a structural transition from a pretransition state to, for example, a low-temperature phase, as described by the order parameter S^z [4]. For the crystal in a stress field with the component Ω_a stimulating a decrease in the asymmetry of a double-well potential, the Landau expansion of the thermodynamic potential in the vicinity of the point of structural transition can be written as [4]

$$\Delta\Phi = \alpha(S^z)^2/2 + \delta(S^z)^3/3 + \gamma(S^z)^4/4 \\ + \hbar\Omega_a S^z - (1/2)\lambda\Omega_a^2. \tag{1}$$

The evolution of a homogeneous order parameter S^z is described by the Landau–Khalatnikov equation

$$\dot{S}^z = -\partial\Delta\Phi/\partial S^z = g(S^z) - \hbar\Omega_a, \tag{2}$$
$$g(S^z) = -\alpha S^z - \delta(S^z)^2 - \gamma(S^z)^3.$$

As can be seen from this equation, the rate of variation of the order parameter depends not only on the order parameter S^z but on the stress field component Ω_a as well. This component stimulates a passage to the pretransition state: the greater the Ω_a value, the smaller the order parameter.

At a fixed Ω_a value, propagation of the wave of switching in a structurally unstable crystal is described by the equation

$$\dot{S}^z = g(S^z, \Omega_a) + D\partial^2 S^z/\partial z^2, \tag{3}$$
$$g(S^z, \Omega_a) = -\alpha S^z - \delta(S^z)^2 - \gamma(S^z)^3 - \hbar\Omega_a.$$

The rate and direction of the transition in a propagating switching wave is determined by the quantity $A(\Omega_a) = \int_{S_1^z}^{S_3^z} g(S^z, \Omega_a)dS^s$ [6, 7]. For $A > 0$, the wave propagation leads to switching from the pretransition state with $S_z = S_1^z = 0$ to the low-temperature phase with $S^z < 0$. For $A < 0$, the wave switches the crystal from the low-temperature phase ($S^z < 0$) to the pretransition state $S^z = S_1^z = 0$. As can be seen from Eq. (3), the rate and direction of the switching wave can be controlled by varying the external action. In the case of small values of the external driving force ($\sigma < \sigma_c$), the wave will cause passage to the pretransition state, while sufficiently large external forces ($\sigma > \sigma_c$) will convert the crystal into the low-temperature phase.
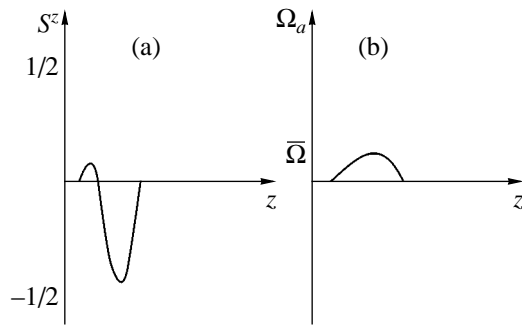
Fig. 1. Plots of (a) the order parameter S^z and (b) the stress field component Ω_a versus the coordinate z.

In the vicinity of the structural transition, the stress field component Ω_a varies with time and exhibits a singularity at $\sigma = \sigma_c$ [4]. Assuming the diffusion of this stress field component to be negligibly small, we can describe the evolution of Ω_a (possessing an inelastic relaxation character) in terms of the Landau–Khalatnikov equation:

$$\dot{\Omega}_a = -\partial\Delta\Phi/\partial\Omega_a = -\hbar S^z + \lambda_0(\sigma_c - \sigma)\Omega_a, \quad (4)$$

which can be conveniently rewritten as

$$\tau\dot{\Omega}_a = \Omega_a - \overline{\Omega}(S^z), \quad \tau^{-1} = \lambda_a(\sigma_c - \sigma),$$
$$\overline{\Omega}(S^z) = \tau\hbar S^z. \quad (5)$$

Here, τ is the relaxation time of the stress field component and $\overline{\Omega}(S^z)$ is the equilibrium value of Ω_a established when a preset value of the order parameter S^z is maintained. Relations (5) show that $\overline{\Omega}(S^z)$ is a monotonically increasing function of S^z. For $\sigma \longrightarrow \sigma_c$, the relaxation time of the stress field component Ω_a can be considered to be much greater than the relaxation time of the order parameter S^z.

Transforming the coordinate as $\xi = z - V_0 t$, we convert Eqs. (3) and (5) into a system of ordinary differential equations:

$$-V_0 S_z' = g(S_z, \Omega_a) + DS_z'', \quad -\tau V_0\Omega_a' = \Omega_a - \overline{\Omega}(S_z). (6)$$

A spatially localized solution to system (6) will be found for the additional conditions that $S_z \longrightarrow S_z^0 = 0$ and $\Omega_a \longrightarrow \Omega_a^0 = 0$ as $\xi \longrightarrow \pm\infty$, where (S_z^0, Ω_a^0) is the stationary homogeneous rest state. The existence of such a solution implies the presence of a separatrix loop of the stationary saddle point (S_z^0, Ω_a^0) corresponding to the rest state [6, 7], which is possible only for a definite value of the parameter V_0 in Eqs. (6). For large τ, the velocity of a solitary pulse (autosoliton) determined by solving the nonlinear eigenvalue problem has the following form:

$$V_0 \approx \nu^*(1 - \zeta\tau^{-1}), \quad (7)$$

where $\nu^* \approx (\delta_0/2\gamma)\nu_{\text{sound}}|T_{\text{MA}} - T|$ is the velocity of the switching wave described by Eq. (3) for $\Omega_a = \Omega_a^0$ and ζ is a coefficient on the order of unity. As can be seen from expression (7), the velocity of the autosoliton in the vicinity of the structural transition is significantly lower than the velocity of sound.

Figure 1 shows a solution of system (6) representing a solitary pulse propagating in a structurally unstable crystal. As can be seen from Fig. 1a, the order parameter S^z exhibits a sharp drop, passes through a minimum, and then performs a steep ascent. The stress field component Ω_a (Fig. 1b) driven by the order parameter first slowly increases and then falls to zero. The pulse front represents the wave of switching from the pretransition state to the low-temperature phase, while the pulse decay corresponds to the reverse switching wave moving at the same velocity.

The above results lead to an important conclusion: in the vicinity of the structural transition cased by an external action, the structurally unstable crystal behaves as an excitable active medium (provided that the relaxation time of the stress field component Ω_a can be considered to be much greater than the relaxation time of the order parameter S^z). Let a fluctuation of the order parameter to arise in a crystal occurring in a pretransition state with the order parameter $S^z = 0$ and the stress field component $\Omega_a = 0$. As a result of this fluctuation, the order parameter decreases ($S^z < 0$) and the stress field component increases ($\Omega_a > 0$). When Ω_a reaches a certain critical level, the order parameter ceases to drop and starts increasing, while the stress field component slowly decays. As a result, the crystal returns to the initial pretransition state. Thus, for $\sigma \longrightarrow \sigma_c$, a spatially localized collective excitation of the atomic lattice (autosoliton) appears and propagates in a structurally unstable crystal occurring in a pretransition state. This autosoliton, on the one hand, is a structural defect comprising two interphase boundaries separated by the second phase, and, on the other hand, it can be considered as a pulse of the inelastic strain field. It should be emphasized that the velocity of the autosoliton in the vicinity of the structural transition is significantly lower than the velocity of sound.

In the particular case of a structural transition of the shear type, the generated autosoliton can play the role of a precursor from which the core of a defect (stacking fault, split dislocation, etc.) will form [1, 2]. It is of primary importance to note that elementary collective exactions of the lattice—autosolitons and solitons [5]—have a general nature, since their appearance is related to the structural transition under the conditions of variable external action, when the crystal loses stability and

exhibits rearrangement into a different structural state. During this transition, the binding forces are not broken, and only a relatively small energy is required to provide for a local transfer of atoms from their positions in one lattice to the sites of a different lattice. However, this is sufficient to induce a local crystallographic shear and to form a fragment of the new lattice structure. In the stress field, such autosolitons propagate by a relay-race mechanism, which accounts for their sufficiently high mobility in the crystal lattice.

REFERENCES

1. V. G. Pushin, V. V. Kondrat'ev, and V. N. Khachin, *Pretransition Phenomena and Martensite Transformations* (Yekaterinburg, 1998) [in Russian].

2. V. E. Panin, V. A. Likhachev, and Yu. V. Grinyaev, *Structural Levels of the Deformation of Solids* (Nauka, Novosibirsk, 1985) [in Russian].

3. V. E. Panin, V. E. Egorushkin, Yu. A. Khon, and T. F. Elsukova, Izv. Vyssh. Uchebn. Zaved. Fiz., No. 12, 5 (1982).

4. E. E. Slyadnikov, Fiz. Tverd. Tela (St. Petersburg) **46**, 1065 (2004) [Phys. Solid State **46**, 1095 (2004)].

5. E. E. Slyadnikov, Fiz. Tverd. Tela (St. Petersburg) **47**, 469 (2005) [Phys. Solid State **47**, 484 (2005)].

6. V. G. Yakhno, *Autowave Processes in Systems with Diffusion* (Inst. Fiz. Poluprovodn., AN SSSR, Gorki, 1981) [in Russian].

7. A. Yu. Loskutov and A. S. Mikhailov, *Foundations of Synergetics* (Nauka, Moscow, 1990; Springer-Verlag, Berlin, 1990).

Translated by P. Pozdeev

Ultrafast Current Switching
Using the Tunneling-Assisted Impact Ionization Front
in a Silicon Semiconductor Closing Switch

S. K. Lyubutin, S. N. Rukin*, B. G. Slovikovsky, and S. N. Tsyranov

Institute of Electrophysics, Ural Division, Russian Academy of Sciences, Yekaterinburg, Russia
* e-mail: rukin@iep.uran.ru
Received July 15, 2004; in final form, November 8, 2004

Abstract—Ultrafast current switching in semiconductors, based on the mechanism of tunneling-assisted impact ionization front, has been experimentally implemented and theoretically studied. A voltage pulse with an amplitude of 220 kV and a front duration of 1 ns was applied to a semiconductor device containing 20 serially connected silicon diode structures. After switching, 150- to 160-kV pulses with a power of 500 MW, a pulse duration of 1.4 ns, and a front duration of 200–250 ps were obtained in a 50-Ω transmission line. The maximum current and voltage buildup rates amounted to 10 kA/ns and 500 kV/ns, respectively, at a switched current density of 13 kA/cm^2. The results of numerical simulation are presented, which show that the current switching is initiated at a threshold field strength of about 1 MV/cm in the vicinity of the p–n junction, where the tunneling-assisted impact ionization begins. © *2005 Pleiades Publishing, Inc.*

Introduction. One of the most rapid means of current switching in semiconductors is based on the formation of a delayed impact ionization wave in the base of a p^+–n–n^+ diode structure, where the velocity of the wave of electron–hole plasma propagation is several times higher than the saturated drift velocity of charge carriers [1, 2]. For the wave excitation, it is required that the rate of the reverse voltage buildup in the diode exceed ~10^{12} V/s. The diode is triggered at a certain delay (2–4 ns), when the field in the vicinity of the p–n junction reaches a level of ~200–300 kV/cm. The electron–hole plasma with a density on the order of 10^{16} cm^{-3} is capable of switching a current density of up to several kA/cm^2 within a time period of several hundred picoseconds.

Recent theoretical investigations by Rodin *et al.* [3, 4] showed that the process of formation and propagation of the ionization wave front substantially changes if the voltage buildup rate increases to 10^{13} V/s and the diode base does not contain free carriers. In this case, the field at the p–n junction reaches ~1 MV/cm within a time of about 1 ns, and then the tunneling ionization of silicon is initiated. The generated free carriers initiate the process of avalanche impact ionization, with the formation of the ionization front. This tunneling-assisted impact ionization front propagates at a velocity several dozens of times higher than the saturated drift velocity of charge carriers and creates plasma with a density above 10^{17} cm^{-3}.

The aim of this study was to realize in experiment the tunneling-assisted impact ionization mechanism of

current switching in silicon diodes and to study this process by methods of numerical simulation.

Experimental. The experimental system is schematically depicted in Fig. 1. Overvoltage in the investigated current interrupter ($S2$) was created using a solid-state generator of short pulses (SM–3NS) with an output SOS-diode-based closing switch and an additional pulse-shaping circuit including a forming line and a pulse sharpener [5]. Figure 1 shows this output part of the charging generator, comprising a 50-Ω forming line ($FL1$) with an outer diameter of 90 mm and a sharpening diode ($S1$) operating in the regime of delayed impact ionization wave. The charging generator was loaded on a 25-mm-long cone-shaped forming line ($FL2$), which played the role of an intermediate capacitive storage and provided matching of the diameters of lines $FL1$ and $FL3$. Transmission line $FL3$ had a wave impedance of 48.6 Ω at an outer diameter of 30 mm and was loaded on a matched resistor (*3*). All lines were filled with transformer oil. The closing switch arranged at the entrance of transmission line $FL3$ comprised an array of 20 serially connected diode structures of the
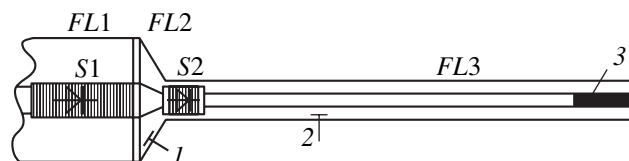

Fig. 1. Schematic diagram of the experimental setup (see the text for explanations).

p^+–p–n–n^+ type, each with a thickness of 320 μm and an area of 0.25 cm². The p–n junctions were buried at a depth of 165 μm. The total interelectrode distance in the switch (including the intermediate copper cooling plates) was about 9 mm.

The voltage pulses in lines $FL2$ and $FL3$ were measured using capacitive voltage dividers (1 and 2 in Fig. 1). The output pulses from these dividers were fed to a 6-GHz digital stroboscopic oscilloscope (TDS 820). The intrinsic signal buildup time in the measuring circuit did not exceed 70 ps. The measurements were performed at a pulse repetition rate from 100 to 200 Hz.

Upon switching the SM–3NS generator on, line $FL1$ was charged within 3 ns to a voltage of ~300 kV, which triggered diode $S1$ and initiated the charging of line $FL2$. The voltage on $FL2$ increased to ~220 kV for a time period of about 1 ns, after which switch $S2$ operated to discharge lines $FL1$ and $FL2$ to the load via line $FL3$.

Figure 2 shows a pulse shape measured on the voltage divider 2 situated in transmission line $FL3$. This pulse had a voltage amplitude of 156 kV, a current amplitude of 3.2 kA, a power of 500 MW, a full width at half-maximum (FWHM) of 1.4 ns, and a current density of about 13 kA/cm². On charging line $FL2$, switch $S2$ transfers a bias current for ~1 ns that creates a prepulse in line $FL3$ with an amplitude of about 10% of that of the main pulse. For this reason, the time of current switching was estimated from oscillograms on a level of 0.2–0.9 of the amplitude. Under these conditions, the output pulse front width was 214 ps. The maximum current and voltage buildup rates in transmission line $FL3$ amounted to 10.4 kA/ns and 504 kV/ns, respectively.

Numerical simulation. A theoretical model was based on the joint solution of the Kirchhoff equations (describing the operation of an electric circuit) and equations describing the dynamics of electrons and holes in the diode structure. It was assumed that the voltage drop was uniformly distributed over serially connected diodes, so that the process of current switching could be calculated for a single semiconductor diode. The calculation was performed taking into account a real distribution of dopants in the structure with a thickness of $W = 320$ μm and an area of $S = 0.25$ cm². The base was n-Si with an initial carrier density of 10^{14} cm⁻³; the p^+ region was formed by boron diffusion (boundary impurity density, 10^{21} cm⁻³; penetration depth, 85 μm); the p region was obtained by aluminum diffusion (10^{17} cm⁻³, 165 μm); and the n^+ region was obtained by phosphorus diffusion (5×10^{19} cm⁻³; 90 μm).

The dynamics of electrons and holes in the diode structure was calculated using a basic system of equations, including the equations of continuity for electrons and holes and the Poisson equation for the electric field. The rate of the tunneling-assisted electron–hole
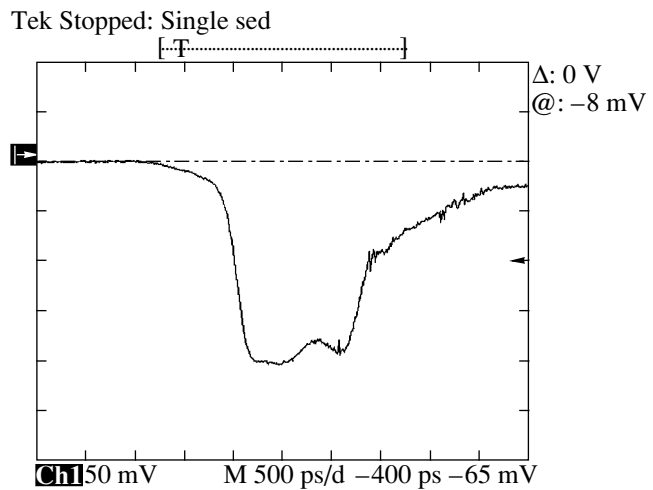
Tek Stopped: Single sed

Δ: 0 V
@: −8 mV

Ch1 50 mV   M 500 ps/d −400 ps −65 mV

Fig. 2. The typical oscillogram of a voltage pulse in transmitting line $FL3$ (abscissa scale, 500 ps/division).

pair generation in the bulk was taken into account by analogy with [3]. The theoretical model was described in more detail previously [6].

The time variation of the voltage acting upon the diode structure was taken from experimental data (Fig. 3, solid curve). This process can be divided into two parts. The initial part is a relatively slow prepulse determined by the bias current passage through diode $S1$ during the charging of line $FL1$. The second part corresponds to the rapid charging of line $FL2$ after the triggering of diode $S1$.

The results of numerical calculations showed that a slow voltage increase to ~2 kV in the first stage within ~3 ns is accompanied by the transfer of major carriers from low-doped p and n regions and the formation of a region of strong electric field with a maximum at the p–n junction. In the second stage, the voltage exhibits a rapid increase (at a rate of 10–15 kV/ns) to reach 11.4 kV within 0.9 ns, followed by a drop to almost zero within ~60 ps, while the current increases up to ~3 kA (Fig. 3, dashed curve).

At the time when the voltage exhibits a maximum, the electric field strength at the p–n junction reaches $E_m \sim 1$ MV/cm. This initiates the tunneling of carriers and leads to their avalanche multiplication, which results in the formation of tunneling-assisted impact ionization wave. The wave propagates away from the p–n junction in both directions, filling the low-doped p and n regions with a high-density plasma. Figure 4 shows the plasma density and the electric field strength profiles in the structure upon the onset of the process of current switching (Fig. 3b, point 1) and upon termination of this process (Fig. 3, point 2). The period of time between the events described in Figs. 4a and 4b (i.e., between points 1 and 2 in Fig. 3b) is about 60 ps. The
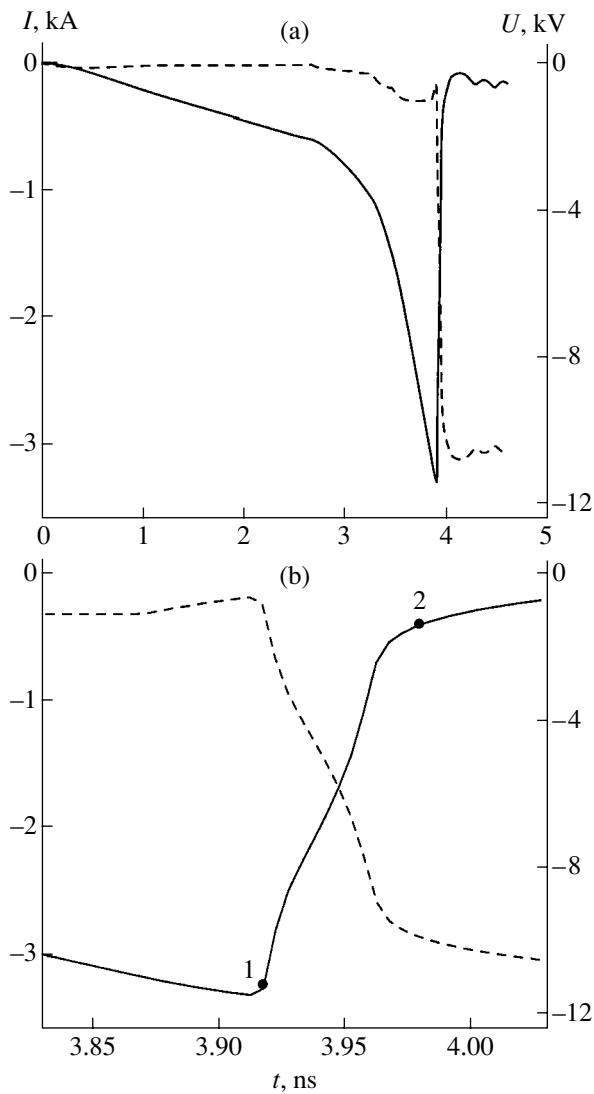
Fig. 3. (a) Numerically calculated temporal profiles of the current (dashed curve) and voltage (solid curve) in the diode structure and (b) the same process on a greater time scale in the region of switching.

average plasma density in the structure is 10^{17} cm^{-3}, which is one order of magnitude higher than the value for the usual impact ionization wave.

The results of our numerical calculations revealed a substantial role of the slow voltage prepulse, which plays the role of the reverse bias, eliminating major carriers from the low-doped regions prior to the onset of rapid voltage buildup. Replacement of the experimental curve of the voltage buildup with a prepulse by a linear increase in the voltage at a rate of 10 kV/ns leads to a situation in which the voltage across the structure does not reach a level corresponding to the onset of the tunneling impact ionization. The avalanche multiplication of carriers begins at a field strength of 200–300 kV/cm and leads to the formation of a usual impact ionization wave with an average plasma density of about 10^{16} cm^{-3}.

Taking into account that (i) the charge in the course of switching in depleted p and n regions is transferred only by the bias current and (ii) the field in these regions cannot exceed E_m corresponding to the onset of the tunneling ionization, we can estimate the velocity of propagation of the field and plasma front as

$$V = \frac{J}{e(N_d - N_a)}, \tag{1}$$

where J is the current density; N_d and N_a are the donor and acceptor concentration, respectively; and e is the electron charge.

As the ionization wave propagates in the p region, an increase in the current density is accompanied by a growth in the acceptor concentration. For this reason, the wave velocity in the p region remains almost unchanged. In the n region, where the donor concentration is constant, the wave velocity grows with the current density to reach a level of $\sim 30V_s$ (where $V_s \sim 10^7$ cm/s is the saturated drift velocity of charge carriers). In our calculations, the average wave velocity was $8V_s$ in the p region and $14V_s$ in the n region, while the total velocity of plasma filling the structure was $22V_s$.

The increase in the wave velocity leads to expansion of the space charge region at the plasma boundary, which increases the maximum field E_m and, hence, the intensity of the avalanche multiplication. In the n region, the E_m value in the stage of rapid current buildup reaches 1.1 MV/cm and the plasma density grows from 1×10^{17} cm^{-3} to 1.2×10^{17} cm^{-3}. The inverse situation is observed in the p region, where the E_m value decreases from 1 to 0.8 MV/cm and the plasma density, from 1×10^{17} to 0.7×10^{17} cm^{-3} (Fig. 4). It should be also noted that the E_m value in our calculation did not decrease below 0.8–0.9 MV/cm, since the charge carriers initiating the avalanche multiplication process can appear only due to the tunneling ionization.

Discussion. Thus, we have experimentally realized the tunneling-assisted impact ionization mechanism of current switching in a silicon diode structure. This provided for record high values of the switching rate: 500 kV/ns with respect to voltage and 10 kA/ns with respect to current, at a current density of 13 kA/cm^2 and a switching time below 250 ps.

The results of numerical simulation showed that the rapid switching process was initiated when an electric field strength in the region of the p–n junction reached a level of 1 MV/cm, corresponding to the onset of the tunneling ionization of silicon. Allowance for the real doping profile in a diode structure with a deeply buried p–n junction showed that two ionization fronts are formed in the system and propagate away from the p–n junction in opposite directions, both in the p and n (base) regions, thus decreasing the total time of filling the structure with the plasma. The total velocity of this
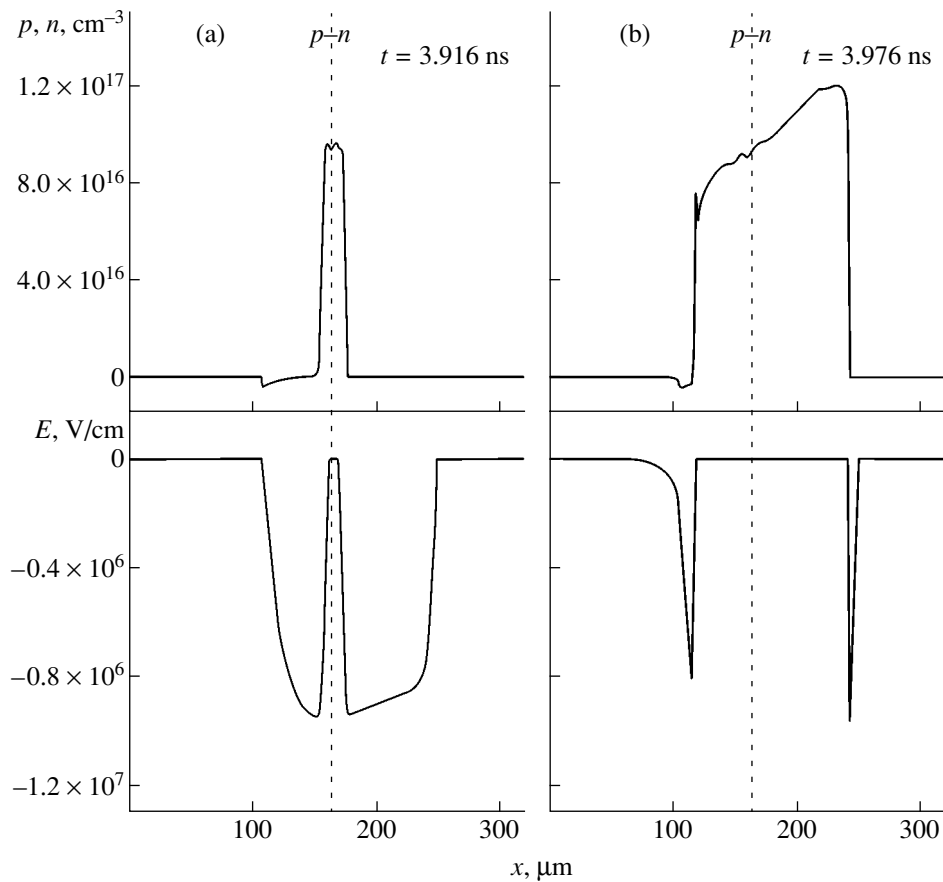
Fig. 4. The plasma density p and the electric field strength E profiles in the structure (a) upon the onset of the process of current switching (Fig. 3b, point 1) and (b) upon termination of this process (Fig. 3, point 2).

process was 22 times the saturated drift velocity of charge carriers.

The values of the voltage drop across the diode structure at which the switching is initiated in the model calculation virtually coincide with the experimental data. The main difference between calculation and experiment is in the time of current switching: 60 and ~200 ps, respectively. This discrepancy is related to the finite length and nonzero inductance of the real $S2$ diode structure. Evaluation of the minimum pulse front duration possible under the experimental conditions studied gave the following results: the time of the electromagnetic wave propagation along the device structure filled with transformer oil (including the time of wave establishment in the transmission line $FL3$) was 95 ps, while the time of the voltage pulse buildup in the transmission line (related to the diode inductance) is 150 ps. Taking into account that the intrinsic signal buildup time in the measuring circuit is about ~70 ps, we may ascertain that the pulse front duration under the

experimental conditions studied cannot be shorter than ~190 ps.

REFERENCES

1. I. V. Grekhov and A. F. Kardo-Sysoev, Pis'ma Zh. Tekh. Fiz. **5**, 950 (1979) [Sov. Tech. Phys. Lett. **5**, 395 (1979)].

2. I. V. Grekhov, A. F. Kardo-Sysoev, L. S. Kostina, and S. V. Shendereĭ, Zh. Tekh. Fiz. **51**, 1709 (1981) [Sov. Phys. Tech. Phys. **26**, 984 (1981)].

3. P. Rodin, U. Ebert, W. Hundsdorfer, and I. Grekhov, J. Appl. Phys. **92**, 958 (2002).

4. P. Rodin, U. Ebert, W. Hundsdorfer, and I. Grekhov, J. Appl. Phys. **92**, 1971 (2002).

5. E. A. Alichkin, S. K. Lyubutin, A. V. Ponomarev, *et al.*, Prib. Tekh. Éksp., No. 4, 106 (2002).

6. S. N. Rukin and S. N. Tsyranov, Pis'ma Zh. Tekh. Fiz. **30** (1), 43 (2004) [Tech. Phys. Lett. **30**, 19 (2004)].

Translated by P. Pozdeev

Optic Parameters of a Middle-Focus Kumakhov Lens for Hard X-rays

A. Yu. Romanov

Institute for Roentgen Optics, Moscow, Russia
e-mail: androm@iroptic.ru
Received August 25, 2004

Abstract—Middle-focus Kumakhov polycapillary lenses for hard X-ray optic systems are created for the first time. The performance of such a lens has been studied for X-rays in the 20–65 keV range. The radiation energy density amplification coefficient of the lens in this energy range falls within four to two orders of magnitude. Thus, the upper boundary of the energy range for effective use of the Kumakhov polycapillary X-ray optics has been increased to over 60 keV. © 2005 Pleiades Publishing, Inc.

The main working energy range of the existing devices of the Kumakhov polycapillary X-ray optics extends approximately from 0.5 to 30 keV, and most of the previous investigations of the performance of Kumakhov lenses were performed in this very range [1–3]. This situation is explained by the fact that (i) the effective transmission of polycapillary lenses sharply decreases with increasing X-ray photon energy and (ii) a part of the radiation penetrates through the capillary walls and contributes to parasitic transmission [4–8]. The development of polycapillary X-ray lenses capable of effectively operating in the range of energies up to 60 keV would open new possibilities for use of the Kumakhov optics in medicine, microelectronics, and other fields. Recently, the first systems of this kind have been created at the Institute for Roentgen Optics (Moscow). The new systems are employed in combination with X-ray sources having a power above 1 kW and a focal spot size within 0.1–0.3 mm. A divergent radiation beam from the X-ray source is transferred via a Kumakhov lens and focused into the spot with a diameter of about 50 μm, which is sufficiently small for many applications. This Letter presents the results of investigation of the performance of a middle-focus Kumakhov polycapillary X-ray lens.

Some parameters of the Kumakhov polycapillary X-ray lens studied are presented in the table, where D_1 is the input diameter of the lens; L is the length; F_1 and F_2 are the front and back focal distances of the lens,

respectively; and Q_1 is the acceptance angle. The X-ray transmission measurements were performed using the radiation of an X-ray tube monochromated by filters so as to retain the hard X-ray component.

Figure 1 shows the dependence of the focal spot size d on the radiation energy at the output of the Kumakhov lens. At each energy, the spot size was determined by scanning the beam cross section with a knife edge at a focal distance F_2 from the lens output. The d value was defined as a full width at half-maximum of the differential intensity distribution. On the whole, the result corresponds to the theoretical estimate $d = 2F_2\vartheta_{cr}$, where ϑ_{cr} is the critical total reflection angle. However, there is some tendency to underestimate the spot size at lower energies, which agrees with the results reported in [1]. An increase in the spot size for higher energies is probably related to the penetration of radiation through the glass capillary walls.

Figure 2 shows a plot of the Kumakhov lens transmission (defined as the ratio of the input and output radiation intensities) for several X-ray photon energies in the range studied.

Using the obtained experimental data, it is possible to calculate the coefficient of amplification, $G(E)$, of the radiation energy density at the focal spot of the lens in the energy range studied. The results of these calculations are presented in the table. The amplification coefficient $G(E)$ is defined as the ratio of the radiation energy density at the focal spot of the lens to the energy

Some parameters and performance characteristics of a middle-focus Kumakhov polycapillary lens for hard X-rays

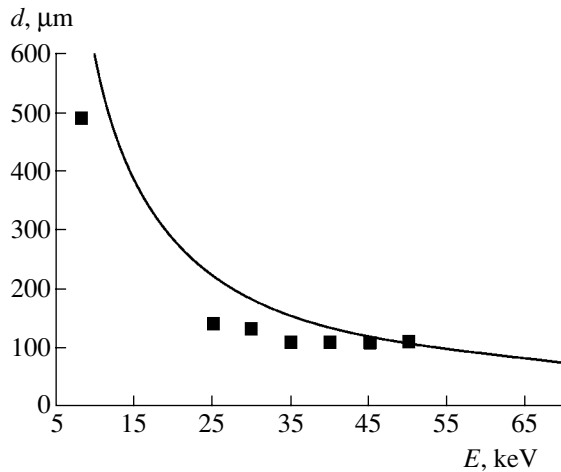| D_1, mm	L, mm	F_1, mm	F_2, mm	Q_1, rad	E, keV	25	30	35	40	45	50	55	60	65
3	265	180	95	0.017	G	2130	1205	976	656	425	318	236	171	130
					R_{eff}, mm	11.6	15.5	17.2	20.9	26	30	34	41	47

Fig. 1. A plot of the focal spot size d versus the X-ray photon energy E for the Kumakhov lens studied. The curve shows the theoretical dependence $y = a/x$; black squares represent the results of experimental measurements.
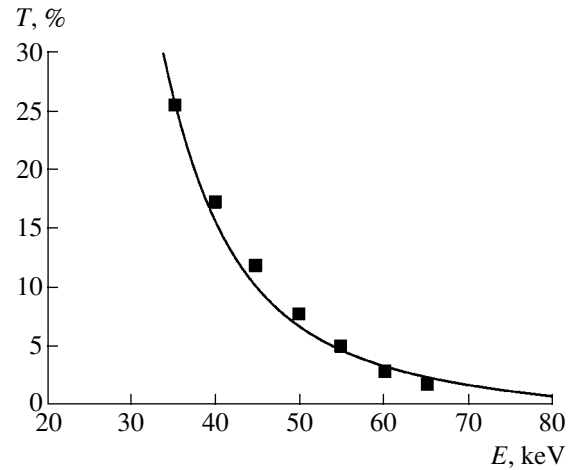

Fig. 2. A plot of the Kumakhov lens transmission T versus the X-ray photon energy E. Black squares represent the experimental data; the curve is drawn so as to provide the best fit to experiment.

density created by the same radiation source in the same plane in the absence of the lens:

$$G = \left(\frac{D_1}{d}\right)^2 \left(\frac{F_1 + L + F_2}{F_1}\right)^2 T. \qquad (1)$$

The G values calculated using this formula fall within four to two orders of magnitude, which implies that the upper boundary of the energy range for effective use of the Kumakhov polycapillary X-ray optics has been increased to over 60 keV.

A more illustrative characteristic is the effective distance R_{eff}, defined as

$$R_{\text{eff}} = \frac{F_1 + L + F_2}{\sqrt{G}}, \qquad (2)$$

which describes an equivalent approach of the irradiated object to the source provided by the lens at various radiation energies (see table).

As can be seen, the amplification characteristics, despite a decrease at high energies, are nevertheless significant in the entire energy range studied. At a distance of ~50 cm, a radiation energy density at the object obtained with the aid of the lens is equivalent to approaching the source to a distance several times shorter. In real systems, this approach is frequently either impossible because of peculiarities in the X-ray tube design or undesirable for certain experimental conditions. Thus, the use of a Kumakhov lens simplifies the problem of arrangement of the equipment. The achieved parameters of X-ray focusing make the Kumakhov lenses useful in physical experiments, microelectronic technologies, medicine, and some other applications. In view of the fact that such lenses significantly attenuate hard X-rays with energies above 80 keV, there is no need to use additional filters.

Thus, significant technological difficulties have been surmounted, and the range of high X-ray photon energies (40–60 keV) is now accessible for the Kumakhov polycapillary X-ray optics.

REFERFENCES

1. S. S. Kazakov, S. V. Nikitina, and V. I. Trefilov, Proc. SPIE **4155**, 13 (2000).

2. S. V. Nikitina, D. I. Gruev, N. S. Ibraimov, *et al.*, Proc. SPIE **4765**, 137 (2002).

3. A. Yu. Romanov, I. V. Dmitriev, and A. Yu. Akulov, Inzh. Fiz., No. 1, 43 (2004).

4. L. Wang and C. A. MacDonald, Proc. SPIE **2519**, 218 (1995).

5. L. Wang, B. K. Rath, W. M. Gibson, *et al.*, J. Appl. Phys. **80**, 3628 (1996).

6. A. N. Nikitin, Proc. SPIE **3115**, 143 (1997).

7. Cari, Suparmi, S. D. Padiyar, *et al.*, Proc. SPIE **4144**, 183 (2000).

8. Suparmi, Cari, L. Wang, *et al.*, J. Appl. Phys. **90**, 5363 (2001).

Translated by P. Pozdeev

Scanning X-ray Microscopy Based on Kumakhov Optics and a Raster X-ray Source

V. D. Gelever and A. Yu. Romanov*

Institute for Roentgen Optics, Moscow, Russia
*e-mail: androm2@yandex.ru
Received August 5, 2004

Abstract—The concept of scanning X-ray microscopy has been practically implemented for the first time using a cylindrical polycapillary structure of the Kumakhov X-ray optics and a scanning microfocus X-ray source. The scanning X-ray microprobe is provided by electron-beam scanning of a focal spot over the target in a transmission X-ray tube equipped with an output cylindrical polycapillary structure. © *2005 Pleiades Publishing, Inc.*

The sample image in X-ray scanning microscopy can be obtained in two ways, whereby either an object is moved relative to the probing beam (object scanning) or the beam is scanned over the object surface (beam scanning). The object scanning is provided by mechanical movement of the object and is used in setups with massive X-ray sources such as synchrotrons. The principle of beam scanning is realized using movable laboratory X-ray sources generating microbeams. A new step in the organization of this scheme is the use of the Kumakhov polycapillary X-ray optics [1–4]. In the system with a transmission X-ray tube, the beam scanning can be realized by moving the point source relative to an immobile cylindrical polycapillary structure, which is provided by electron-beam scanning of a focal spot over the target in the X-ray tube.

This principle is close to the approach used in X-ray topographic imaging of single crystals described in [5, 6], where matrices of parallel collimating capillaries were used in combination with a scanning X-ray tube so as to obtain weakly divergent beams. The possible design of such a tube developed for the X-ray microscopic imaging was described in [7]. This approach was also used in X-ray absorption flaw detectors, where capillaries were arranged behind the probed object [8]. Owing to the principle of image transmission via separate elements, it is possible to increase the sensitivity and to eliminate the need for relative mechanical movements of parts in the setup, which is a valuable circumstance in practice. However, the X-ray beam intensities used in previous investigations were low because of weak X-ray sources and low-transmission optics, which significantly limited the potential of scanning X-ray probe techniques.

It should be noted that all systems described above used the polycapillary structure only as a collimator of the X-ray beam, while the possibility of transmitting X-ray images by means of total external reflection from the inner walls of capillaries was not considered.

A further development of the approach employing microcapillary collimating arrays is the scanning X-ray microscopy using elements of the modern Kumakhov X-ray optics. Using this optics in combination with a microfocus X-ray source, it is possible to obtain quasi-parallel scanning beams of higher intensity and smaller cross section, which is achieved due to the total internal reflection of radiation from the inner walls of capillaries [1, 2]. A decrease in the diameter of the guiding channels and the use of glass reflecting surfaces leads to multiple internal refection, which significantly increases the specific intensity of the probing X-ray beam.

Recently, high-intensity quasi-parallel X-ray microbeams have been obtained [1, 2] with a diameter on the order of 10 μm, a radiation flux density on the order of 10^{10} photons/(s mm^2), and a divergence within several milliradians (which is close to the parameters of synchrotron radiation). The initial radiation was obtained from a microfocus source based on an X-ray tube of the transmission type. The primary divergent beam was converted into a quasi-parallel beam by a cylindrical polycapillary structure of the Kumakhov X-ray optics with micron-diameter channels. The scanning X-ray microscopy scheme described below is the development and realization of these principles of the formation of high-intensity X-ray microbeams.

Another important circumstance is that the computational power of personal computers has significantly increased, which allows all functions of controlling the electron-probe device, monitoring the current parameters, and processing the data to be performed in real time [9]. The increasing performance of computer image processing provides wide possibilities for high-quality and high-precision data extraction from experimental results.

This paper describes an experimental realization of the scanning X-ray microscopy based on quasi-parallel high-intensity X-ray microbeams in a system employing the aforementioned X-ray tube equipped with a cylindrical polycapillary device of the Kumakhov X-ray optics.
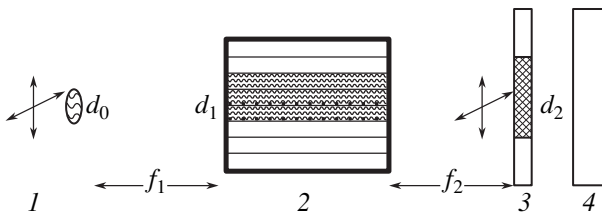
Fig. 1. Schematic diagram of the scanning X-ray microscope using a cylindrical polycapillary structure and a scanning microfocus X-ray source: (*1*) focal spot of the X-ray tube; (*2*) polycapillary structure; (*3*) object; (*4*) detector. See the text for explanations.
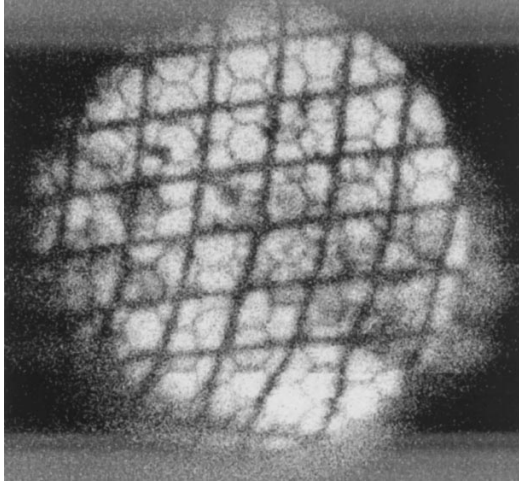

Fig. 2. Image of a copper wire obtained with a scanning X-ray microscope using a cylindrical polycapillary structure and a scanning microfocus X-ray source.

The principle of the proposed method is as follows. A cylindrical polycapillary structure of the Kumakhov X-ray optics is placed as close as possible to the anode of a microfocus scanning X-ray tube. The intense quasi-parallel scanning microbeam obtained at the output of the capillary structure contains the source image in the cross section [3]. The object under investigation is placed as close as possible to the output of the polycapillary structure, and a detector is situated on the optical axis behind the object.

Figure 1 shows the optical scheme of this system, where f_1 is the distance from the capillary structure entrance to the focal spot of the tube, f_2 is the distance from the object to the polycapillary structure exit, d_1 is the input diameter, and d_2 is the probing beam on the object. Using this scheme, it is possible to probe the object with a beam whose diameter d_2 is determined by the effective focal spot of the X-ray tube (d_0), the capillary diameter (d_3), and the distances from the polycapillary structure to the focal spot (f_1) and the object (f_2):

$$d_2 = d_0 + 2d_3 + 2f_1\theta_c + 2\theta_c f_2,$$

where θ_c is the critical angle of the total internal reflection of X-rays from the inner walls of the capillary.

The X-ray source was based on a transmission X-ray tube of the BS-11 type, with the electron beam

focused and scanned by means of a system of magnetic lenses. The scanned image was formed by a video system controlling the electron beam motion over the X-ray tube target by means of programmed variation of the currents in beam-deflecting coils. This scanning was synchronized with the processing of a signal obtained from the detector. The scanned region image was displayed on a computer screen.

The thickness of the beryllium window of the X-ray tube was about 200 μm. The system permitted ultimate approach to the anode. The experiments were performed using a tube with copper anode operating at a voltage of 25 keV and a current of 100 μA. The polycapillary structure had a length of 1 cm, a capillary diameter of 5 μm, and a total diameter of 5 mm. Under these conditions, we obtained a microprobe with a beam cross section diameter at the object on the order of 10 μm and a radiation flux density on a level of 10^{10} photons/(s mm^2), which could be operated in the scanning X-ray microscopy regime.

Figure 2 shows an example of the scanning X-ray microscopy image of the grid made of a copper wire with a diameter of 50 μm. The image reflects, besides the object studied, the structure of the optical system, including the brightness distribution over the anode surface, the walls of capillaries not transmitting X-rays, and the distribution of transmitted radiation over the working area of the polycapillary structure. Undoubtedly, additional optimization of the optical scheme and other components will provide a significant improvement in the quality of images and expand the class of objects studied by this method.

REFERENCES

1. A. Yu. Romanov and I. V. Dmitriev, in *Proceedings of the Meeting on X-Ray Optics, Nizhni Novgorod, 2004*, pp. 221–225.
2. A. Yu. Romanov and I. V. Dmitriev, Pis'ma Zh. Tekh. Fiz. **30** (18), 65 (2004) [Tech. Phys. Lett. **30**, 784 (2004)].
3. A. Yu. Romanov, Izmer. Tekh., No. 7 (2004).
4. A. Yu. Romanov and I. V. Dmitriev, Inzh. Fiz., No. 1 (2004).
5. B. F. Belyaev, Yu. B. Glushanok, V. A. Gushchin, *et al.*, in *Instruments and Methods of X-Ray Analysis: Collection of Articles* (LNPO "Burevestnik," Leningrad, 1980), Issue 24, pp. 137–141 [in Russian].
6. V. P. Efanov, N. I. Komyak, V. G. Luttsau, and N. V. Rabodsei, US Patent No. 3,833,810 (1974).
7. V. A. Gushchin, V. P. Efanov, S. A. Ivanov, and V. G. Luttsau, Prib. Tekh. Éksp., No. 6, 152 (1978).
8. V. P. Efanov, N. I. Komyak, and V. G. Luttsau, Prib. Tekh. Éksp., No. 1, 217 (1975).
9. Yu. A. Demin, E. L. Demchenko, V. A. Il'in, *et al.*, Nauchn. Priborostr. **9** (2), 14 (1999).

Translated by P. Pozdeev

Analytical Solution of the Poisson–Boltzmann Equation in Cases of Spherical and Axial Symmetry

L. G. D'yachkov

Institute for High Energy Densities, Associated Institute for High Temperatures, Russian Academy of Sciences, Moscow, Russia
e-mail: dyachk@iht.mpei.ac.ru
Received September 17, 2004

Abstract—An exact analytical solution of the Poisson–Boltzmann (PB) equation in cases of spherical, axial, and planar geometry has been obtained in the form of the logarithm of a power series. This solution describes an electrostatic potential distribution around a charged macroscopic particle (wire, plane) under conditions of thermal equilibrium at an arbitrary ratio of the density of charge borne by the particles (wires, planes) to the charge density in the surrounding plasma. Previously, an analytical solution of the PB equation was known only in the case of planar geometry. © 2005 Pleiades Publishing, Inc.

One of the main problems in the physics of dusty plasma and colloidal systems in electrolytes is related to the screening of charged macroscopic particles. Under the conditions of thermal equilibrium, the distributions of the electrostatic potential and charge around a macroscopic particle (grain) are described by the Poisson–Boltzmann (PB) equation. In a dusty plasma, such conditions can arise, for example, in the case when grains are charged via a thermionic mechanism. Well-known solutions to the linearized PB equation are given by the Debye–Hückel and Deryaguin–Landau–Verwey–Overbeek potentials [1, 2]. However, in the case of large charges, the screening is substantially nonlinear. For this reason, the PB equation is frequently solved either by numerical methods [3–6] or analytically with allowance for the next terms in the expansion of the Boltzmann exponent [4, 7].

This paper presents an exact analytical solution of the PB equation obtained in the form of the logarithm of a power series, which is valid in cases of spherical, axial, and planar geometry. Previously, analytical solutions of the PB equation were known only for planar problems [1, 8]. The obtained solution is valid for a macroscopic grain bearing a charge of any sign. For definiteness, the charge will be assumed to be positive and the surrounding medium will be called plasma.

The PB equation is as follows:

$$\Delta\Phi = 4\pi e[n_{e0}\exp(e\Phi/kT) - n_{i0}\exp(-e\Phi/kT)], \quad (1)$$

where n_{i0} and n_{e0} are the number densities of the positively and negatively charged plasma particles in the region where the electric potential is $\Phi = 0$. For the sake of simplicity, these particles will be assumed to be singly charged and called ions and electrons, respectively. We also assume that other macroscopic grains do not participate in the screening of the grain under consideration, so that the average distance between grains exceeds the screening radius. In what follows, we use a dimensionless potential defined as $\varphi = e\Phi/kT$ and measure the lengths in units of the Debye electron radius in the region of zero potential: $R_{eD} = (kT/4\pi e^2 n_{e0})^{1/2}$. Then, in cases of spherical ($L = 2$), axial ($L = 1$), and planar ($L = 0$) geometry, Eq. (1) can be written as

$$\frac{d^2\varphi}{dr^2} + \frac{L}{r}\frac{d\varphi}{dr} = e^{\varphi} - \delta e^{-\varphi}, \quad (2)$$

where $\delta = n_{i0}/n_{e0}$. The case of $\delta = 1$ corresponds to a single macroscopic grain (wire, plane) in a quasi-neutral plasma, while $\delta = 0$ corresponds to the case when the entire positive charge is concentrated on the charged grains (wires, planes), for example, in a thermionic plasma.

The boundary conditions for Eq. (2) depend on the particular problem under consideration. For example, in the case of a single spherical macroscopic particle bearing a given charge Z_d, we have

$$\varphi(\infty) = 0, \quad d\varphi/dr|_{r_d} = -z_d/r_d^2, \quad (3)$$

where $z_d = Z_d e^2/kTR_{eD}$ is the dimensionless charge and r_d is the dimensionless radius of the particle. In the case under consideration, it is convenient to set zero conditions at a certain finite distance a, such that

$$\varphi(a) = 0, \quad d\varphi/dr|_a = 0. \quad (4)$$

Conditions (4) are also applicable to the cases of both planar and cylindrical geometry ($L = 0, 1$). Below, we are primarily interested in finding a solution of the PB equation in the case of spherical symmetry ($L = 2$),

but the solutions for $L = 0, 1$ will obtained as well. It should be also noted that conditions (4) correspond to the cell approximation, which is valid when the system of macroscopic particles is strongly nonideal, that is, $(Z_d^2 e^2/kTaR_{eD})^{1/2} \gg 1$ [9]. The boundary conditions will be set at $a = (4\pi N_d/3)^{-1/3}/R_{eD}$, where N_d is the concentration of macroscopic particles in the plasma. If the charge of the particle is known, we can solve Eq. (2) with boundary conditions (4) and select the value of a to obey the second condition in (3). In the case of a single macroscopic particle in a plasma, we take $a \gg 1$.

In order to obtain a solution to Eq. (2) in an analytical form in terms of a power series, let us eliminate the exponent by substituting

$$\varphi = q \ln y, \qquad (5)$$

where q is a certain nonzero integer. Since it is natural to perform expansion in the vicinity of the point $r = a$ (where the boundary conditions (4) are set), let us substitute the variable as

$$r = a(1 - x)^p,$$

where p is a positive integer or half-integer. This eventually yields the equation

$$(1 - x)\left[y\frac{d^2y}{dx^2} - \left(\frac{dy}{dx}\right)^2 \right] - (Lp - p + 1)y\frac{dy}{dx} \qquad (6)$$
$$- \frac{p^2}{q}a^2(1 - x)^{2p-1}(y^{q+2} - \delta y^{2-q}) = 0$$

with the boundary conditions

$$y(0) = 1, \quad dy/dx|_0 = 0. \qquad (7)$$

Let us seek a solution to Eq. (6) in the form of a series:

$$y = \sum_{n=0}^{\infty} b_n x^n. \qquad (8)$$

Boundary conditions (7) immediately yield $b_0 = 1$ and $b_1 = 0$. Substituting expression (8) into Eq. (6), we can obtain a recurrent relation for the coefficients b_n with $n \geq 2$, but, in the general case (for arbitrary p and q), this expression will be rather cumbersome. This poses the problem of selecting the optimum values of these parameters. The value of q determines the degree of nonlinearity in (6), that is, the number of power series in the product and, hence, the multiplicity of sums in the recurrent relation. Thus, in order to simplify the solution, q has to be selected so as to minimize the degree of nonlinearity in Eq. (6), which, in the general

case of $\delta \neq 0$, is achieved for $q = 1$. The convergence of series (8) is worse when $x \longrightarrow 1$, that is, near the surface of small particles ($r_d \ll a$). In this case, it will probably be required to calculate a large number of terms ($\sim 10^3$). The convergence can be accelerated by selecting the parameter p to be sufficiently large, since an increase in p (for the given a and r) decreases the quantity $x = 1 - (r/a)^{1/p}$. On the other hand, large p values complicate Eq. (6).

To compromise, let us chose $p = 2$. For $q = 1$ and $p = 2$, the recurrent relation for the coefficients in series (8) is as follows:

$$b_{n+2} = \frac{2L - 1}{n + 2}b_{n+1} + \frac{1}{(n + 1)(n + 2)} \qquad (9)$$
$$\times \{4a^2[(1 - \delta)b_n + \delta(3b_{n-1} - 3b_{n-2} + b_{n-3})] + S_1\},$$

$$S_1 = \sum_{k=0}^{n-1} \{(k + 1)[(k + 2)b_{k+2}(b_{n-k-1} - b_{n-k})$$

$$+ (n - k + 1)b_{k+1}(b_{n-k+1} - b_{n-k}) + 2Lb_{k+1}b_{n-k}]$$

$$+ 4a^2 b_k(b_{n-k} + S_2)\},$$

$$S_2 = \sum_{k'=0}^{n-k-1} b_{k'}(b_{n-k-k'} - 3b_{n-k-k'-1}$$

$$+ 3b_{n-k-k'-2} - b_{n-k-k'-3}),$$

where all coefficients b_n with negative subscripts, as well as the sums S_1 and S_2 with negative superscripts, should be set zero. The explicit formulas for several initial coefficients are as follows:

$$b_2 = 2a^2(1 - \delta), \quad b_3 = \frac{2}{3}a^2(1 - \delta)(2L - 3),$$

$$b_4 = \frac{a^2}{6}(1 - \delta)[(2L - 1)^2 + 2 + 8a^2(2 - \delta)].$$

Let us consider two limiting cases: $\delta \longrightarrow 1$ and $\delta \longrightarrow 0$. For $\delta \longrightarrow 1$, the density of the positive charge concentrated on the macroscopic particles is negligibly small compared to the charge density in the plasma. This can be due to a decrease in Z_d or N_d. When N_d decreases, the cell size exhibits infinite growth, although at a slow rate. For small macroscopic particles ($r_d \ll 1$), we have $a < 10$ even for $1 - \delta \sim 10^{-5}$. For $\delta = 0$, the entire positive charge is concentrated on the macroscopic particles. In this case, the term $\sim y^{2-q}$ in Eq. (6) vanishes and the optimum parameter is $q = -2$. Then, it

is sufficient to take $p = 1$ and obtain a recurrent relation much simpler than (9):

$$b_{n+2} = \frac{L}{n+2}b_{n+1} + \frac{1}{(n+1)(n+2)} \tag{10}$$
$$\times\left(\frac{a^2}{2}(\delta_{n1} - \delta_{n0}) + S_1\right),$$

$$S_1 = \sum_{k=0}^{n-1}(k+1)\{(k+2)b_{k+2}(b_{n-k-1} - b_{n-k})$$
$$+ b_{k+1}[(n-k+1)b_{n-k+1} - (n-k-L)b_{n-k}]\},$$

where δ_{ij} is the Kronecker delta. The explicit formulas for several initial coefficients are as follows:

$$b_2 = -\frac{a^2}{4}, \quad b_3 = -\frac{a^2}{12}L,$$

$$b_4 = -\frac{a^2}{96}[2L(L+2) - a^2],$$

$$b_5 = -\frac{a^2}{240}L[(L+2)(L+3) - 3a^2].$$

As is known, repeated application of the recurrent formulas may lead to significant errors. For the region at the surface of a small particle ($r/a \sim 0.01$), where the convergence of series (8) is slow and it is necessary to determine up to $\sim 10^3$ terms, the calculations were performed with the usual and with a twice-better precision. A comparison showed that the results coincided to within several decimal digits.

Once the potential $\varphi(r)$ is known, the electric field strength is readily calculated as

$$E(r) = -\frac{d\varphi}{dr} = \frac{qdy/dx}{pa(1-x)^{p-1}y},$$

and the charge inside a sphere or a cylinder of radius r (or a layer of halfwidth r) is

$$z(r) = \begin{cases} E/2\pi, & L = 0, \\ 2^{L-2}Er^L, & L = 1, 2 \end{cases} \tag{11}$$

(for $L = 0$ and 1, the charge refers to a unit area or length, respectively). In the Coulomb field ($E \sim r^{-L}$), function (11) has a constant value. In general, the shape of this function clearly shows the character of screening of the given macroscopic particle (wire, plane). Evidently, $z(r_d) = z_d$.

In the planar case ($L = 0$), the exact analytical solution of Eq. (2) is known [1, 8], which has a simple form for $\delta = 0$ and $\delta = 1$. For $\delta = 0$, the potential is expressed

as $\varphi = \ln\{\cos^{-2}[(a-r)/2^{1/2}]\}$ and, in this case, we have shown that this expression is equivalent to relations (5), (8), and (10).

The average electron density for a cell is given by the formula

$$\bar{n}_e = \frac{L+1}{a^{L+1} - r_d^{L+1}}\int_{r_d}^{a} n_e(r)r^L dr$$
$$= \frac{(L+1)pn_{e0}}{1 - (r_d/a)^{L+1}}\int_0^{x_d} y^q(1-x)^{(L+1)p-1}dx, \tag{12}$$

where $x_d = 1 - (r_d/a)^{1/p}$. For $q > 0$, the integral in expression (12) can be calculated analytically. In the case of $L = 2$, $p = 2$, and $q = 1$, we obtain the average electron density

$$\bar{n}_e = \frac{6n_{e0}}{1 - (r_d/a)^3}\sum_{n=0}^{\infty}b_n\left(\frac{x_d^{n+1}}{n+1} - 5\frac{x_d^{n+2}}{n+2}\right.$$
$$\left.+ 10\frac{x_d^{n+3}}{n+3} - 10\frac{x_d^{n+4}}{n+4} + 5\frac{x_d^{n+5}}{n+5} - \frac{x_d^{n+6}}{n+6}\right) \tag{13}$$

and the average ion density

$$\bar{n}_i = \frac{3}{a^3 - r_d^3}n_{i0}\int_{r_d}^{a}\frac{r^2 dr}{y}, \tag{14}$$

where the latter integral has to be calculated using numerical methods.

Let us consider the potential $\varphi(r)$ and the charge $z(r)$ inside a sphere of radius r, as given by expression (11) for the experimental conditions [10] in a thermally equilibrium plasma at $T = 1700$ K containing CeO_2 dusty particles with a radius of 0.4 μm and a density of $N_d = 5 \times 10^7$ cm^{-3}. The electron density was $n_e \sim 2.5 \times 10^{10}$ cm^{-3} with an uncertainty within 30%, while the ion density was about ten times lower. With neglect of the ion component, the condition of quasi-neutrality yields a dust particle charge of $Z_d \approx 500$. Generally speaking, the measured values of n_e should be compared to a certain electron density averaged over the cell, for example, with that given by formula (12). However, taking into account the error of measurements, let us assume this value to be equal to n_{e0}. Then, $R_{eD} = 18$ μm, and we obtain $r_d = 0.022$, $z_d = 0.27$, and $a = 0.94$. The parameter δ should be taken equal to zero or considered as being small ($\delta \ll 1$).

Figures 1 and 2 show the potential and charge distributions determined for the parameters indicated above and various values of δ. For $\delta = 0$, the problem has no solution: both potential and charge tend to infinity at
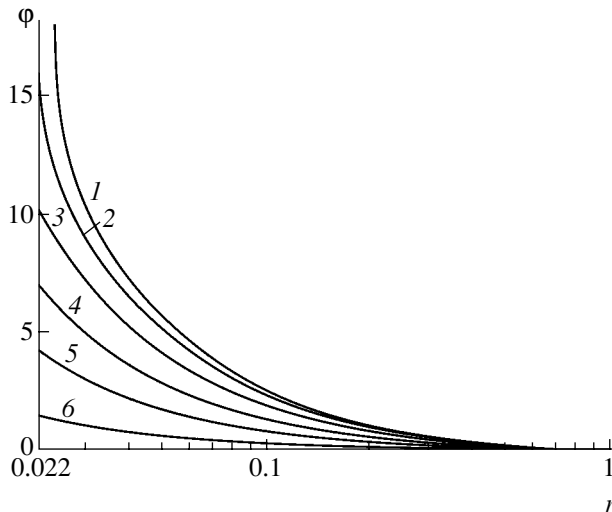
Fig. 1. The spherically symmetric electrostatic potential $\varphi(r)$ around a macroscopic particle in a plasma, calculated for the experimental conditions studied in [10] and various values of the parameter δ: (*1*) 0; (*2*) 0.1; (*3*) 0.28; (*4*) 0.5; (*5*) 0.7; (*6*) 0.9.
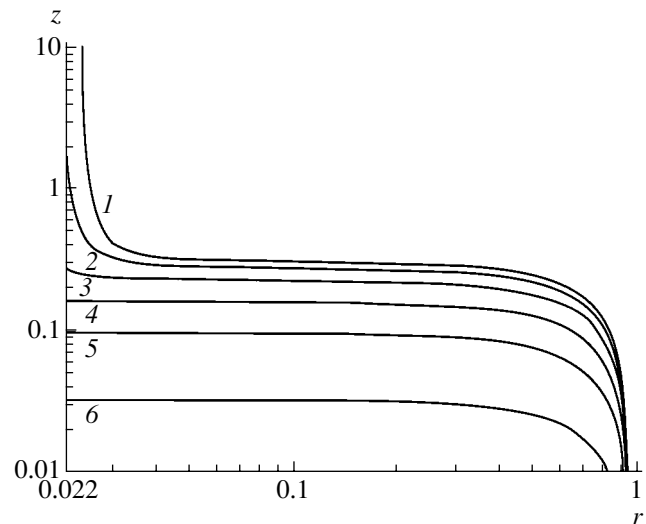

Fig. 2. The spherically symmetric charge distribution inside a sphere of radius r around a macroscopic particle in a plasma, calculated for the experimental conditions studied in [10] and various values of the parameter δ: (*1*) 0; (*2*) 0.1; (*3*) 0.28; (*4*) 0.5; (*5*) 0.7; (*6*) 0.9.

$r = 0.0243$. For $\delta = 0.1$, a solution exists, but the charge ($Z_d \approx 4000$) is one order of magnitude greater than the experimental value observed for $\delta = 0.28$ (for comparison, the solutions for still greater δ values are presented as well). According to formulas (13) and (14), $\overline{n}_e = 1.25 n_{e0} = 3.1 \times 10^{10}$ cm^{-3} and $\overline{n}_i = 0.95 n_{e0}\delta = 0.66 \times 10^{10}$ cm^{-3}. As can be seen from Fig. 2, the curves for all δ exhibit a rather broad range where $z(r)$ is almost constant. In this region, the potential has practically a Coulomb shape with an effective charge equal to $z(r)$. For small δ (where the macroscopic particle has a large charge z_d), the effective charge is much smaller than this value. As the δ value grows, the particle charge decreases and becomes almost equal to the effective value.

REFERENCES

1. B. V. Derjaguin and L. D. Landau, Acta Physicochim. URSS **14**, 633 (1941); L. D. Landau, *Collected Works* (Nauka, Moscow, 1969), Vol. 1, pp. 386–411.
2. E. J. W. Verwey and J. Th. G. Overbeek, *Theory of the Stability of Lyophobic Colloids* (Elsevier, Amsterdam, 1948).
3. E. G. Gibson, Phys. Fluids **9**, 2389 (1966).
4. A. P. Nefedov, O. F. Petrov, and S. A. Khrapak, Fiz. Plazmy **24**, 1109 (1998) [Plasma Phys. Rep. **24**, 1037 (1998)].
5. S. I. Yakovlenko, Kratk. Soobshch. Fiz., No. 1, 9 (2002).
6. V. A. Gundienkov and S. I. Yakovlenko, Zh. Éksp. Teor. Fiz. **122**, 1003 (2002) [JETP **95**, 864 (2002)].
7. J. Vranješ, M. Y. Tanaka, B. P. Pandey, and M. Kono, Phys. Rev. E **66**, 037401 (2002).
8. S. I. Yakovlenko, Pis'ma Zh. Tekh. Fiz. **27** (9), 83 (2001) [Tech. Phys. Lett. **27**, 389 (2001)].
9. I. T. Yakubov and A. G. Khrapak, Sov. Technol. Rev. B **2**, 269 (1989).
10. V. E. Fortov, A. P. Nefedov, O. F. Petrov, *et al.*, Zh. Éksp. Teor. Fiz. **111**, 467 (1997) [JETP **84**, 256 (1997)].

Translated by P. Pozdeev

Controlling the Josephson Contact Parameters in a Semiconductor–Superconductor Eutectic Composition

G. I. Isakov

Institute of Physics, National Academy of Sciences of Azerbaijan, Baku, Azerbaijan
e-mail: gudrat@physics.ab.az
Revised manuscript received July 1, 2004

Abstract—The current–voltage (I–U) curve was studied for the Josephson contact in a GaSb–V_2Ga_5 eutectic composition comprising parallel whiskers of a superconducting V_2Ga_5 phase formed by oriented crystallization in a semiconducting GaSb matrix. It is established that the parameters of the I–U curve can be controlled by varying the angle between the direction of electric current and the axis of whisker orientation. Using the Josephson relation $h\omega = 2eV$ and considering the parallel connection of infinite Josephson clusters in the structure studied, a formula is derived, $n_0 Nh\omega = 2eV$, which can be used for estimating the electromagnetic radiation frequency ω of the Josephson weak links, the number N of infinite Josephson clusters, and the number $n_0 N$ of Josephson weak links in the semiconductor–superconductor eutectic compositions obtained by means of oriented crystallization. © 2005 Pleiades Publishing, Inc.

Introduction. The creation and investigation of Josephson junctions and related integrations with controlled parameters are among the basic problems studied by modern experimental, theoretical, and applied physics. Most of the disadvantages inherent in various Josephson junctions can be eliminated in structures involving superconducting bridges of constant and variable widths (S–S'–S) and systems of the superconductor–semiconductor–superconductor type (S–Sm–S) type [1]. Among the numerous Josephson junctions, the S–Sm–S type structures are also distinguished by to the possibility of controlling the properties of the semiconductor layer by doping and by applying electric and magnetic fields [2–7]. This poses the important problem of searching for and studying Josephson media with optimum combinations of the semiconducting and superconducting properties.

In an early work [8], the Josephson effect was observed in a semiconductor–superconductor (GaSb–V_2Ga_5) eutectic composition, where the superconducting phase (V_2Ga_5) is formed in the semiconducting matrix (GaSb) in the form of long parallel whiskers. Later [9, 10], the possibilities of controlling the tensometric and superconducting properties of this semiconductor–superconductor eutectic composition were established. In a continuation of the previous investigations, this paper presents original data on the possibility of controlling the parameters of the current–voltage (I–U) curve of the Josephson contact and evaluating the numbers of infinite Josephson clusters and Josephson weak links in the given semiconductor–superconductor eutectic composition.

Experimental results. The I–U curves of the Josephson contacts in GaSb–V_2Ga_5 eutectic composi-tions were measured for various angles α between the directions of electric current (I) and whiskers (X). For this purpose, the samples were cut in the form of squares (Fig. 1a) and disks (Fig. 1b). Then, tin contact pads were applied to the sides of the rectangular plates and to the center and circumference of the disks so that the angle α had the values $0° = \alpha_1 < \alpha_2 < \alpha_3 < \alpha_4 < (\alpha_5 = 45°) < (\alpha_6 = 60°) < \alpha_7 = 90°$. In the case of disks, the angles were $\alpha = 0°, 15°, 30°, 45°, 60°, 75°$, and $90°$. The I–U measurements were performed between electrodes 0–1, 0–2, …, 0–7. It should be noted that the sample plates converted to the superconducting state for all values of α.

Figure 2a shows the I–U curves of the square sample measured at $T = 2$ K for various whisker orientation angles indicated above. As can be seen, the shape of the I–U curve for all α values is typical of the Josephson effect. However, an increase in the angle α leads to a significantly decrease in the critical current: $I_{C1} > I_{C2} > I_{C3} > I_{C4} > I_{C5, C6, C7}$. On the contrary, the final voltage corresponding to the breakage of the superconducting state significantly increases: $U_{C1} < U_{C2} < U_{C3} < U_{C4} < U_{C5, C6, C7}$. For the electrodes 5–7 (i.e., for $45° \leq \alpha \leq 90°$), the I–U curves coincide to within the experimental uncertainty. In addition (for all angles), the I–U curves exhibit hysteresis and the superconductivity is restored in a jumplike manner. The voltage corresponding to restoration of the superconductivity increases in the following order: $U'_{C1} < U'_{C2} < U'_{C3} < U'_{C4} < U'_{C5, C6, C7}$.

The inset in Fig. 2a shows the initial part of the I–U curve measured between electrodes 0 and 7 of the
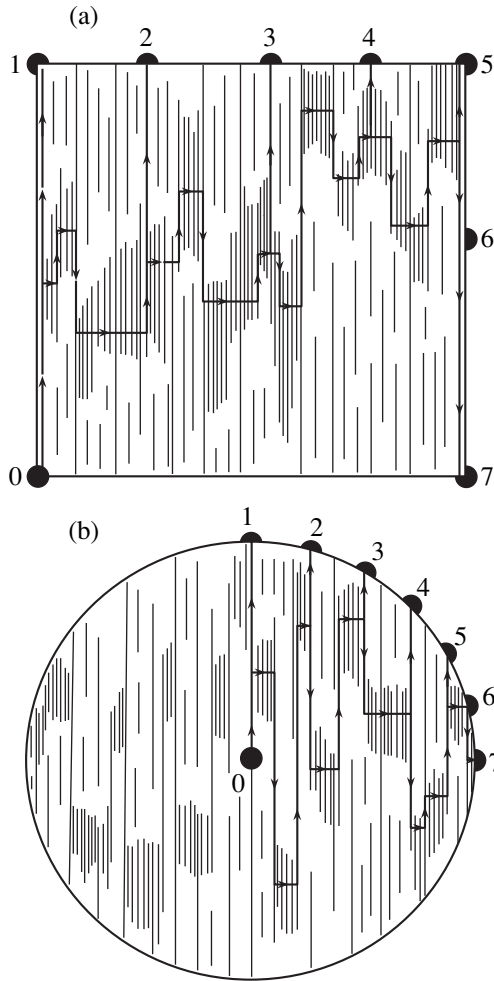
Fig. 1. Schematic diagrams illustrating the structure of (a) square and (b) disk-shaped samples cut from a GaSb–V_2Ga_5 eutectic composition. Thin bars represent whiskers of the superconducting phase, while thick lines show the possible superconducting pathways (or superconducting clusters). Arrows indicate the current directions, numbered black points indicate tin electrodes applied to the samples.

Fig. 2. I–U curves of (a) square and (b) disk-shaped samples cut from a GaSb–V_2Ga_5 eutectic composition. The inset presents the initial part of the curve measured between electrodes 0–7 of the square sample (dashed lines show the negative differential resistances).

square sample. Analogous multistep curves were also observed for electrodes 0–3, 0–4, …, and 0–6. Dashed lines represent the negative differential resistances. Figure 2b shows the I–U curves of the disk-shaped sample measured for various α at $T = 2$ K. As can be seen, the I_C, U_C, and U'_C in this sample for large α angles do not coincide: $I_{C1} > I_{C2} > I_{C3} > I_{C4} > I_{C5} > I_{C6} > I_{C7}$; $U_{C1} < U_{C2} < U_{C3} < U_{C4} < U_{C5} < U_{C6} < U_{C7}$; $U'_{C1} < U'_{C2} < U'_{C3} < U'_{C4} < U'_{C5} < U'_{C6} < U'_{C7}$. It should be noted that, prior to the appearance of a large voltage jump, the curves for the disk-shaped sample also exhibit the sequences of small steps in the current and voltage without external high-frequency radiation and external magnetic field.
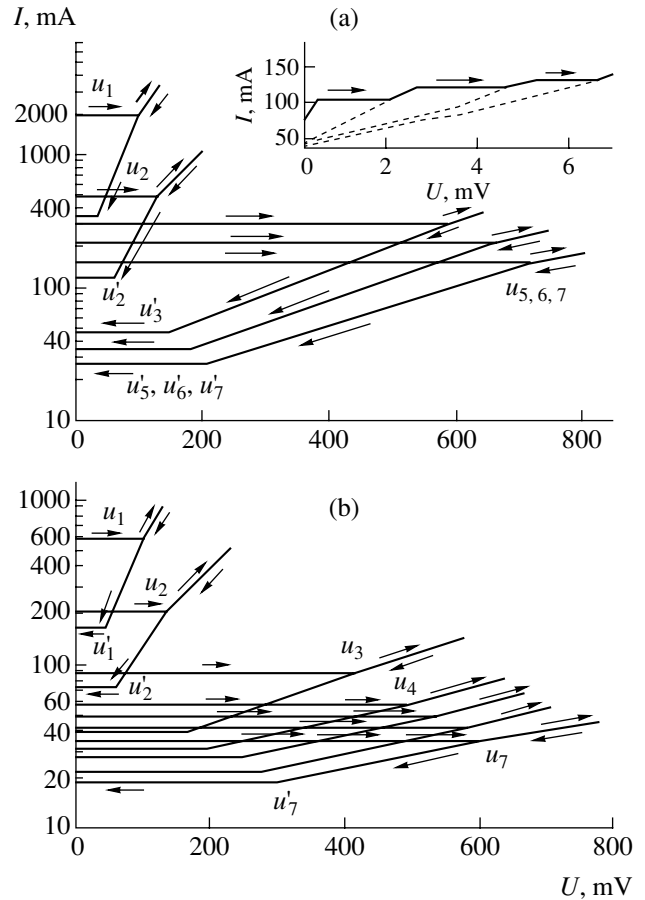
Discussion of results. It was previously demonstrated [10] that, in the case of $I \parallel X$ ($\alpha = 0°$), the superconducting current is transferred predominantly via whiskers representing the Josephson bridges of variable thickness. Some of these whiskers form infinite clusters (by-pass channels) threading through the whole sample. These are clusters of the S–S'–S–S'–S… type (where S is a superconducting whisker or bank, and S' is a narrowing of the whisker or the Josephson microbridge of variable thickness). For $\alpha \neq 0°$, the superconducting current passes via long whiskers connecting the regions of closely spaced short whiskers and via contacts of the S–Sm–S type. In this case, the infinite clusters represent chains of the S–S'–S–Sm–S–S'–S… type (where Sm are semiconducting spacers between superconducting whiskers).

For $I \parallel X$ ($\alpha = 0°$), the total number of Josephson microbridges of variable thickness can be expressed as

$$n = n_0 N, \qquad (1)$$

where n_0 is the number of such microbridges in one whisker and N is the number of whiskers per unit area in the sample cross section (for $I \parallel X$, $N \approx 10^4$ mm^{-2}). Evidently, an increase in the α value leads to a decrease in the density of whiskers involved in the current transfer. Taking into account that $I_C \sim f(N)$, we infer that $0° < \alpha_1 < \alpha_2 < \ldots < 90° = N_i$ corresponds to $N_1 > N_2 > \ldots > N_i$. It should be noted that, in the hierarchy of weak links, clusters of the $S–S'–S–S'–S\ldots$ type are "stronger" than those of the $S–S'–S–Sm–S–S'–S\ldots$ type. Thus, for $\alpha \neq 0°$, the dominating pathways of the superconducting current passage via whiskers with increasing α are replaced by weaker contacts of the $S–Sm–S$ type. Therefore, the parameters of the $I–U$ curve of the Josephson junction can be controlled by changing the α value.

In a system of N infinite Josephson clusters connected in parallel, the total superconducting current is given by the sum

$$I = I_1 + I_2 + \ldots + I_N. \quad (2)$$

Taking into account that currents passing via statistically equivalent clusters are equal to each other, we obtain

$$I_C = N I_{CN}, \quad (3)$$

where I_{CN} is the critical current passing via a single infinite Josephson cluster. Since it is known that $N \approx 10^4$ mm^{-2}, we can use the corresponding $I–U$ curves (Figs. 2a and 2b, curve 1) for estimating I_{CN} (the current corresponding to the breakage of the superconducting state) and the corresponding critical current density J_{CN}. The estimates obtained using formula (3) showed that $I_{CN} = 0.2$ mA and $J_{CN} = 6 \times 10^3$ A/cm^2. As was noted above, the superconducting current passes at $\alpha \neq 0$ via infinite clusters of the $S–S'–S–Sm–S–S'–S\ldots$ type. The presence of superconducting whiskers S and narrowings S' in these pathways shows that the critical current I_{CN} and the critical current density J_{CN} cannot exceed the values indicated above for $\alpha \neq 0$. Therefore, substituting these I_C and I_{CN} values into formula (3), we can also estimate the number of infinite Josephson clusters per unit area. Estimates obtained for the samples of two types are as follows (mm^{-2}): $8 \times 10^2 \leq N \leq 10^4$ (square plate) and $3.7 \times 10^2 \leq N \leq 10^4$ (disk).

It should be noted that multistep $I–U$ curves are typical of whiskers [1, 11, 12]. However, a comparison of the experimental $I–U$ curves observed for the GaSb–V$_2$Ga$_5$ eutectic composition to the data for single tin and aluminum bridges of variable thickness [1, 12] shows that the voltage steps observed in this study have "giant" dimensions. Indeed, the values of the voltage in each step of the multistep curve (see the inset to Fig. 2a) are greater by three orders of magnitude, and those in the single-step curves are five orders (Figs. 2a and 2b) of magnitude greater than the steps in the curves for a single bridge or a single Josephson contact.

We suggest that the giant voltage steps observed in these experiments are caused by synchronization of the Josephson weak links of the same type. In this case, the voltage at each step for a sample in the resistive state ($V \neq 0$) with a sequence of Josephson weak links (see inset to Fig. 2a) over one infinite cluster can be expressed as

$$V = V_1 + V_2 + \ldots + V_{n_0}, \quad (4)$$

where n_0 is the number of sequential synchronized weak links corresponding to each voltage step. Taking into account that the synchronized Josephson weak links are of the same type, we obtain

$$V = V_1 = V_2 = \ldots = V_{n_0}, \quad (5)$$

$$V = n_0 V_{n_0}. \quad (6)$$

The multistep $I–U$ curves for the Josephson contacts were mostly observed under the action of either high-frequency electromagnetic radiation or an external magnetic field [1]. The giant steps in the $I–U$ curves obtained in this study were observed in the absence of external magnetic fields and high-frequency radiation.

Apparently, it is an internal high-frequency electromagnetic field that produces the effect analogous to that of the external high-frequency radiation. The basic Josephson relation

$$h\omega = 2eV \quad (7)$$

is equally valid for Josephson contacts and Josephson weak links of any type. Therefore, all such contacts and weak links for $V \neq 0$ generate high-frequency radiation with a frequency ω. Using expression (6) and basic Josephson relation (7), we may conclude that, in a sequence of Josephson weak links over a single infinite cluster, the radiation energy corresponding to each step can be expressed as

$$n_0 h\omega = 2eV. \quad (8)$$

It should be noted that the superconducting current in a composition passes via N Josephson clusters connected in parallel. Therefore, with allowance for all the Josephson weak links, each voltage step is described by the formula

$$n_0 N h\omega = 2eV. \quad (9)$$

The results of electron-microscopic observations showed that, for $\alpha = 0°$ and a sample length of 4–5 mm, we have $n_0 = 5$ and $n_0 N = 5 \times 10^4$. The estimates obtained using a single-step $I–U$ curve (Fig. 2a, curve 1) and formula (9) in the case of $I \parallel X$ show that the synchronized Josephson weak links generate a high-frequency electromagnetic radiation with $\omega \approx 10^9$ Hz. Assuming that the radiation frequency of the Josephson weak links for various α is approximately the same, a multistep $I–U$ curve (inset in Fig. 2a) can be used for determining the total number of such links $n_0 N$. For example, in the case of $V = 0.1$, 1, and 2 mV, we obtain

$n_0 N = 5 \times 10^2$, 5×10^3, and 10×10^3, respectively. For large voltage steps, $n_0 N$ varies within $5 \times 10^5 - 3.5 \times 10^6$.

Conclusions. The parameters of the I–U curve of the Josephson contacts in a GaSb–V$_2$Ga$_5$ eutectic composition can be controlled by changing the angle α between the direction of electric current I and the axis X of the superconducting whisker orientation in the composition. The parameters in a disk-shaped sample can be controlled in the entire angular interval $0° \leq \alpha \leq 90°$. In a square sample, the I–U curves practically coincide to within the experimental error for $45° \leq \alpha \leq 90°$ and, hence, the I_C, U_C, and U'_C values can be effectively controlled only in the interval $0° \leq \alpha \leq 45°$. This is related to the fact that the Josephson contacts in the square sample for $45° \leq \alpha \leq 90°$ are "equivalent" and that they are connected via an infinite cluster of the S–S'–S–S'–S… type to microbridges S', which are "stronger" than Sm spacers. In the disk-shaped samples for $0° \leq \alpha \leq 90°$, no electrodes (except 0–1 for $\alpha = 0°$) are connected by an infinite cluster of the S–S'–S–S'–S… type.

A formula is suggested for estimating the electromagnetic radiation frequency ω of the Josephson weak contacts, the number of infinite Josephson clusters N, and the number of Josephson weak contacts $n_0 N$ in semiconductor–superconductor eutectic compositions obtained by oriented crystallization.

REFERENCES

1. A. Barone and G. Paterno, *Physics and Applications of the Josephson Effect* (Wiley, New York, 1982).

2. L. G. Aslamazov and M. V. Fistul', Zh. Éksp. Teor. Fiz. **81**, 382 (1981) [Sov. Phys. JETP **54**, 206 (1981)].

3. L. G. Aslamazov and M. V. Fistul', Zh. Éksp. Teor. Fiz. **83**, 1170 (1982) [Sov. Phys. JETP **56**, 666 (1982)].

4. L. G. Aslamazov and M. V. Fistul', Zh. Éksp. Teor. Fiz. **84**, 1516 (1984) [Sov. Phys. JETP **59**, 887 (1984)].

5. Th. Schapers, R. P. Muller, A. Kaluza, *et al.*, Appl. Phys. Lett. **75**, 391 (1999).

6. M. I. Petrov, D. A. Balaev, K. A. Shaĭkhutdinov, *et al.*, Fiz. Tverd. Tela (St. Petersburg) **39**, 829 (1997) [Phys. Solid State **39**, 735 (1997)].

7. M. I. Petrov, D. A. Balaev, K. A. Shuikhutdinov, and K. S. Aleksandrov, Supercond. Sci. Technol. **14**, 788 (2001).

8. M. I. Aliev, G. I. Isakov, F. U. Aliev, and A. T. Eminzade, Dokl. Akad. Nauk SSSR **306**, 583 (1989) [Sov. Phys. Dokl. **34**, 454 (1989)].

9. G. I. Isakov, Pis'ma Zh. Tekh. Fiz. **22** (24), 70 (1996) [Tech. Phys. Lett. **22**, 1032 (1996)].

10. G. I. Isakov, Pis'ma Zh. Tekh. Fiz. **29** (19), 40 (2003) [Tech. Phys. Lett. **29**, 810 (2003)].

11. B. I. Ivlev and N. B. Kopnin, Usp. Fiz. Nauk **142**, 435 (1984) [Sov. Phys. Usp. **27**, 206 (1984)].

12. J. D. Meyer, Appl. Phys. **2**, 303 (1973).

Translated by P. Pozdeev

Widely Tunable Multiwavelength Filter Based on Cascaded Long Period Fiber Gratings[¶]

S. Chen[a,b,*], Q. Zhao[a], L. Liu[a], D. Zhang[a], Y. Yan[a], and X. Dong[a]

[a] Institute of Modern Optics, Nankai University, Tianjin 300071, P.R. China
[b] Mathematics and Physics Department, University of Petroleum, Beijing 102249, P.R. China
* e-mail: sh_h_chen@yahoo.com.cn
Revised manuscript received October 15, 2004

Abstract—A temperature-controlled, continuously and linearly tunable multiwavelength filter based on cascaded long period fiber gratings has been realized. For the first time, a tunable wavelength range of 2.1 nm has been achieved with a temperature variation of 62°C and a regression coefficient of 0.997. The experimental results are in good agreement with the theory. © 2005 Pleiades Publishing, Inc.

Introduction. Since being invented in 1995 by Vengsarkar *et al.* [1], long period fiber gratings (LPGs) have been successfully used as equalizers in erbium-doped fiber amplifiers (EDFAs) [2] and in band rejection filters [2] due to a wide-band transmission in the absence of back reflection. However, because of the wide-band rejection, the LPGs cannot be used as narrow-band filters, especially of the multiwavelength type. Later, cascaded LPGs were suggested [3], which possess several well-separated interference peaks of high extinction ratio. At the same time, this device is among the most promising candidates for multiwavelength generation of dense-wavelength division multiplexing (DWDM) communication networks [4].

Recently, Lee *et al.* [5] tuned the wavelength by applying axial strain [5]. However, even for a strain as large as 3000 με, the tuning range was only 1 nm, which is insufficient to meet requirements to the filters for systems with a channel separation wider than 1 nm.

This paper suggests tuning the filter wavelength by controlled variation of the temperature. For the first time, a tunable range of 2.1 nm has been achieved by varying the temperature from 34 to 96°C, with a regression coefficient of $r = 0.997$. This range can be further increased by expanding the interval of temperature variation. The experimental results agree well with the theoretical simulation. If the channel space matches the ITU grid (i.e. 100 GHz or 50 GHz), it is possible to select a separating fiber of proper length so that the device can perform as a tunable DWDM filter. At the same time, when the tunable range is half of the channel space, it can be designed to operate as an interleaver filter with appropriate temperature variation.

The principle of cascaded LPGs. In order to simplify the consideration, we assume that only two completely uniform LPGs are cascaded. The principle of

beam transmission through cascaded LPGs is qualitatively explained in Fig. 1. A part of the incident core mode is coupled to the cladding mode by the first LPG, which can be recoupled to the core mode by the second LPG. The recoupled core mode interferes with the uncoupled one, and the interference spectrum is the transmission curve of cascaded LPGs.

According to the coupling equations [6], the amplitude of the core $a_{01}^{co}(d)$ and the cladding $a_m^{cl}(d)$ modes of the LPG can be expressed as [7, 8]

$$
\begin{pmatrix} a_{01}^{co}(d) \\ a_m^{cl}(d) \end{pmatrix} = e^{j\frac{(\beta_{01}^{co}+\beta_m^{cl})}{2}d} \begin{pmatrix} e^{j\frac{K}{2}d} & 0 \\ 0 & e^{-j\frac{K}{2}d} \end{pmatrix} \begin{pmatrix} t & r \\ r & t^* \end{pmatrix} \begin{pmatrix} 1 \\ 0 \end{pmatrix},
$$
(1)

with the boundary conditions $a_{01}^{co}(0) = 1$ and $a_m^{cl}(0) = 0$. In Eq. (1), β_{01}^{co} and β_m^{cl} are the corresponding transmission constants; $K = 2\pi/\Lambda$ is the LPG constant; Λ and d are the LPG period and length, respectively; and t, r are
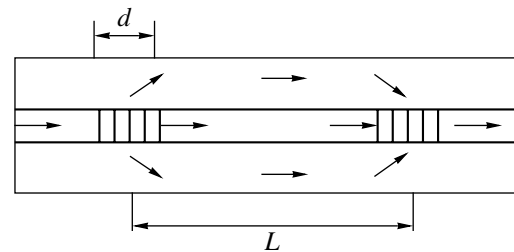

Fig. 1. Schematic diagram of a beam transmitted through a cascaded LPG (see the text for explanations).

[¶] This article was submitted by the authors in English.

the transmission coefficients of the core and cladding modes, respectively, which can be expressed as

$$t = \cos(s_m d) + j \frac{\delta_m}{s_m} \sin(s_m d),$$

$$r = j \frac{\kappa_m}{s_m} \sin(s_m d),$$

(2)

where $s_m = \sqrt{\kappa_m^2 + \delta_m^2}$, $|t|^2$ and $|r|^2$ are the transmission ratios of the corresponding modes,

$$\delta_m = (1/2)(\beta_{01}^{co} - \beta_m^{cl} - 2\pi/\Lambda)$$

is the detuning coefficient, and κ_m is the coefficient of coupling between the core and cladding modes.

After propagating through cascaded LPGs, the amplitudes of the core and cladding modes can be described as follows:

$$\begin{pmatrix} a_{01}^{co}(2d+L) \\ a_m^{cl}(2d+L) \end{pmatrix} = e^{j(\beta_{01}^{co}+\beta_m^{cl})d} \begin{pmatrix} e^{j\frac{K}{2}d} & 0 \\ 0 & e^{-j\frac{K}{2}d} \end{pmatrix} \begin{pmatrix} t & r \\ r & t^* \end{pmatrix}$$

(3)

$$\times \begin{pmatrix} e^{j\beta_{01}^{co}L} & 0 \\ 0 & e^{j\beta_m^{cl}L} \end{pmatrix} \begin{pmatrix} e^{j\frac{K}{2}d} & 0 \\ 0 & e^{-j\frac{K}{2}d} \end{pmatrix} \begin{pmatrix} t & r \\ r & t^* \end{pmatrix} \begin{pmatrix} 1 \\ 0 \end{pmatrix},$$

where L defines the fiber length splicing the LPGs (see Fig. 1). The transmission or extinction ratio $|a_{01}^{co}(2d + L)|^2$ can be simulated according to Eq. (3).

Figure 2 shows the transmission curves of single and cascaded LPGs simulated using Eq. (3). As can be seen, the spectrum of a cascaded LPG is a periodic sine curve with high extinction ratio, modulated by the spectrum of a single LPG and completely symmetrical with respect to the notch peak of the latter spectrum.

Theory of the temperature tuning of the wavelength. As can be seen from Fig. 1, the wavelength of a cascaded LPG will shift upon a change in the phase difference between the core and cladding modes caused by the variation of L. This distance can be readily varied by changing the temperature of the fiber length between two LPGs. The LPG temperature remains unchanged, which simplifies the experimental situation and the theoretical analysis.

Figure 3 shows a plot of the shift of transmission peaks versus temperature. The shift is the same for all peaks, with a temperature coefficient of 0.035 nm/K and a regression coefficient of $r = 0.999$.

In fact, it is very difficult to obtain two completely homogeneous LPGs. For this reason, we have also simulated the transmission curve of cascaded LPGs with slightly different notch spectra. In this case, the interference is weak and the extinction ratio is decreased as
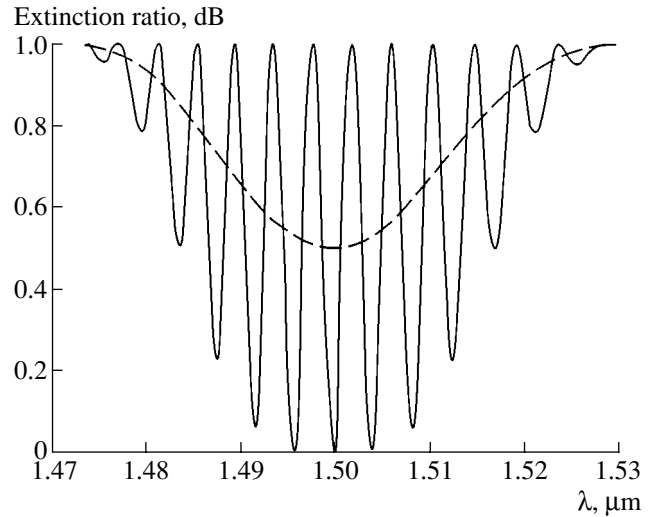

Fig. 2. Transmission curves of single (dashed curve) and cascaded (solid curve) LPGs simulated for $\Lambda = 750$ μm, $\kappa_m d = \pi/4$, $d = 3.75$ cm, and $L = 6d$.
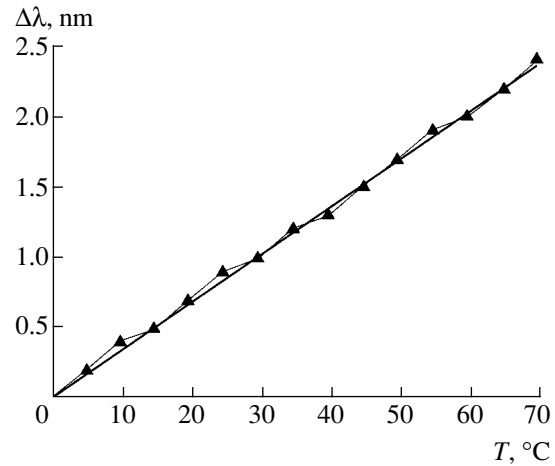

Fig. 3. A plot of the wavelength shift of cascaded LPGs versus temperature. Symbols present the experimental data; the solid line shows the regression curve ($r = 0.999$).

compared to those in Fig. 2. However, the temperature tuning principle remains entirely the same as that for the cascaded LPGs with homogeneous notch spectra. This can be readily explained. Indeed, during the experiment, the LPGs are always kept unaffected by the outside environment and only the temperature of the splicing fiber varies. Thus, the filter wavelength shift is only determined by the properties of the fiber and is independent of the notch spectra of the two LPGs (i.e., of their central notch wavelengths, the band width, and the notch contrast).

Experimental. We have fabricated two LPGs with a length of 1.5 cm, notch peak wavelengths of 1529.6 and 1530.0 nm, and transmission ratios of 14 and 13 dB, respectively. They were connected by an ordinary 59-cm-long single-mode fiber to cascaded LPGs, as in Fig. 1.
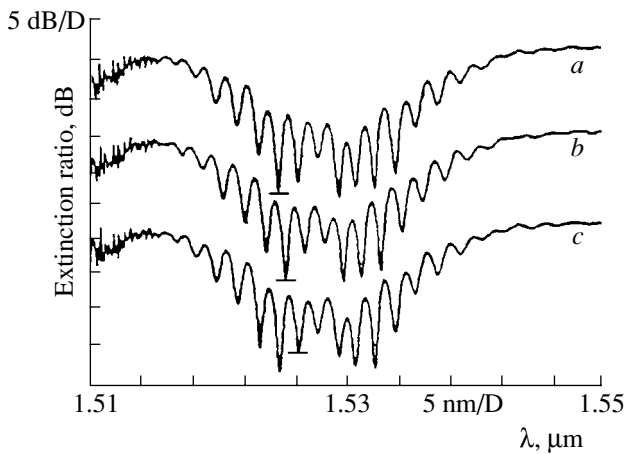
Fig. 4. The experimental transmission spectra of cascaded LPGs measured at (*a*) 34, (*b*) 64, and (*c*) 96°C.
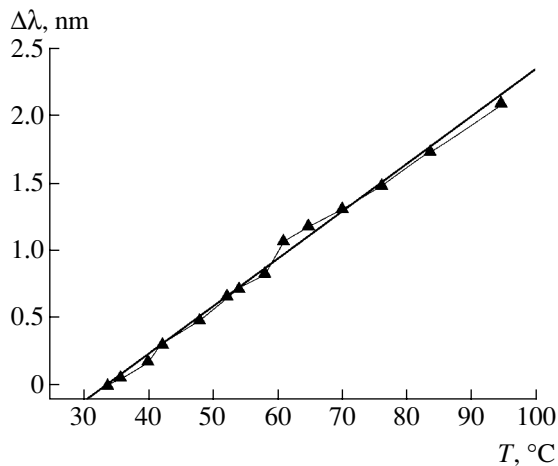

Fig. 5. Experimental plot of the wavelength shift of the 7th notch versus temperature in the interval from 34 to 96°C. Symbols present the experimental data; the solid line shows the regression curve ($r = 0.997$).

The fiber was placed into a controlled temperature cabinet, while the LPGs stayed outside this device. The light from an amplified spontaneous emission (ASE) source based on an erbium doped fiber entered the cascaded LPGs, and the transmitted light was detected by a Q8383 optical spectrum analyzer (OSA) with a resolution of 0.1 nm. When the temperature was slowly varied, a stable interference spectrum was obtained at the output.

Figure 4 shows the transmission spectra of the system measured at 34, 64 and 96°C (for the sake of clarity, the spectra are shifted along the ordinate axis). For the seventh notch, the central loss wavelengths are 1524.3, 1525.5, and 1526.4 nm, respectively. As can be seen from Fig. 4, the largest extinction ratio is only about 8 dB, and the shape of the interference curve is different from that in Fig. 2. These differences are caused by dissimilar characteristics of the two LPGs.

When the temperature increases, all the interference peaks linearly shift toward longer wavelengths.

Figure 5 shows an experimental plot of the wavelength shift of the seventh notch versus temperature in the interval from 34 to 96°C. As can be seen, the maximum shift is 2.1 nm for the full temperature variation, which is wider than the channel space of 1.5 nm. The temperature coefficient (shift sensitivity) is 0.034 nm/°C, and the regression coefficient is $r = 0.997$, in good coincidence with the results of theoretical simulations presented in Fig. 3.

An increase in the fiber temperature is accompanied by some bending of the fiber. However the spectrum shift caused by this factor is less than 0.2 nm, which is much smaller than that the effect of the temperature and can be ignored.

By selecting a separating fiber of proper length, the channel space can be matched to the ITU grid (i.e., 100 GHz or 50 GHz), and the cascaded LPGs can be designed as linearly tunable DWDM filters controlled by the fiber temperature. At the same time, when the wavelength shift is half of the channel space with proper temperature variation, the DWDM filters will perform as interleaver ones.

Conclusions. A temperature-controlled tunable multiwavelength filter based on cascaded LPGs is developed. The tuning curve has a sensitivity of 0.034 nm/°C with a regression coefficient of 0.997, which is consistent with the theory. The tunable multiwavelength filter has wide prospects for use in DWDM filters. However, the tuning rates for both temperature and strain are still too low, which restricts the range of possible applications of the tunable DWDM filter. Works on the fast (or dynamic) tuning of a multiwavelength filter are currently in progress.

REFERENCES

1. A. M. Vengsarkar, P. J. Lemaire, U. B. Judkins, *et al.*, J. Lightwave Technol. **14**, 58 (1996).
2. A. M. Vengsarkar, J. R. Pedrazzani, J. B. Judkins, *et al.*, Opt. Lett. **21**, 336 (1996).
3. X. J. Gu, Opt. Lett. **23**, 509 (1998).
4. J. Chow, G. Town, B. Eggleton, *et al.*, IEEE Photonics Technol. Lett. **8**, 60 (1996).
5. J.-H. Lee, W.-T. Han, U.-C. Paek, *et al.*, Meas. Sci. Technol. **12**, 778 (2002).
6. T. Erdogan, J. Lightwave Technol. **15**, 1277 (1997).
7. B.-H. Lee, Y.-J. Kim, Y.-J. Chung, *et al.*, IEICE Trans. Electron. **E84-C**, 621 (2001).
8. Y. Liu, J. S. R. Williams, L. Zhang, and I. Bennion, Opt. Commun. **164**, 27 (1999).

High-Temperature X-ray Diffraction Study of La$_{0.6}$A$_{0.2}$Mn$_{1.2}$O$_{3\pm\delta}$ (A^{2+} = Sr^{2+}, Pb^{2+}) Metal Oxide Ceramics Exhibiting Colossal Magnetoresistance

I. V. Zhikharev*, V. M. Gromenko, and A. G. Sil'cheva**

Lugansk National Pedagogical University, Lugansk, Ukraine
*e-mail: * i_z@ua.fm; ** annasilcheva@ua.fm*
Received September 6, 2004

Abstract—The temperature dependence of the lattice parameters in lanthanum manganite oxides doped with strontium and lead ions has been studied by high-temperature X-ray diffraction. The lattice parameters exhibit anomalous behavior, which is probably related to the dissolution of cluster compounds in the matrix structure with increasing temperature. Additional annealing in oxygen led to a significant change in the lattice parameters but did not influence the magnetoresistance of samples. © 2005 Pleiades Publishing, Inc.

The phenomenon of colossal magnetoresistance (CMR) found in lanthanum manganite perovskites (LaMnO$_3$) doped with rare earth ions has stimulated extensive research aimed at the elucidation of the nature of this effect (especially at the temperatures of phase transitions) and the application of CMR materials in microelectronics [1, 2]. Of special interest in this respect are materials containing an excess (superstoichiometric) manganese, since these ions mostly determine the magnetic and transport properties of manganites.

Most researchers believe that various (micro-, meso-, and macroscopic) structural inhomogeneities are among the important factors influencing the magnetic and electrical properties of metal oxides [3–5]. The microscopic defects include embedded atoms and vacancies; the mesoscopic inhomogeneities are flaws of the cluster type; macroscopic inhomogeneities violate the phase composition of samples.

We have studied doped lanthanum manganite oxides with a perovskite structure and the general formula

$$\text{La}_{0.6}\text{A}_{0.2}\text{Mn}_{1.2}\text{O}_{3\pm\delta} \ (\text{A}^{2+} = \text{Sr}^{2+},\ \text{Pb}^{2+}).$$
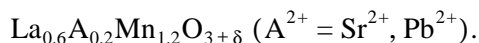
Samples in the form of disks with a diameter of ~10 mm and a height of ~1.5 mm were prepared using the standard ceramic technology and subsequently annealed in oxygen.

The temperature dependence of the lattice parameters was studied by method of high-temperature X-ray diffraction. The measurements were performed on a diffractometer (DRON-UM-1) equipped with a special high-temperature chamber (UVD-2000) and provided with a special sample holder (Fig. 1a). A preset temperature in the working volume of the chamber was measured using a thermocouple (PPR) and maintained by an automated temperature control system. The chamber accommodated a heating element and a system of thermal screens ensuring the maximum uniform indirect heating of a sample to the preset temperature.

Standard sample holders did not allow satisfactory diffraction patterns to be obtained in the course of heating, which was related to variations of the sample surface shape and volume as a result of thermal expansion and chemical reactions in the sample occurring in the high-temperature chamber. For this reason, we have used a specially designed alundum holder provided with a set of adjustment alundum ring spacers (Fig. 1b). This device allowed prolonged (up to several dozens of hours) X-ray diffraction investigations to be performed *in situ* at high temperatures without violation of the measurement geometry.

The ceramic samples, mounted in the special holder and placed into the high-temperature chamber, were
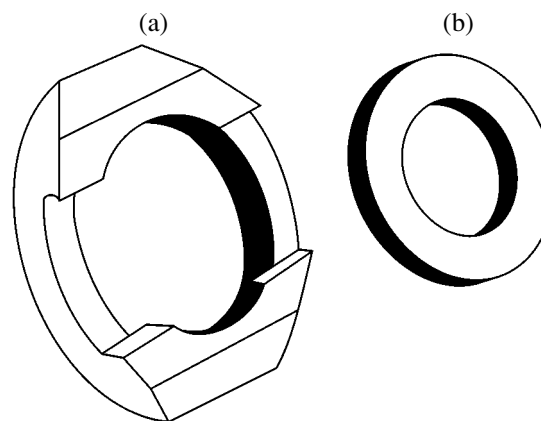

Fig. 1. Schematic diagram of (a) the special sample holder and (b) the adjustment ring.
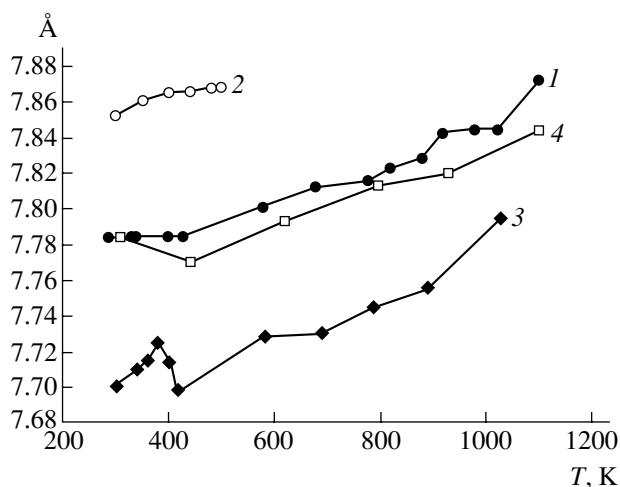
Fig. 2. The temperature dependence of the lattice parameter a of (*1*, *2*) $La_{0.6}Pb_{0.2}Mn_{1.2}O_{3\pm\delta}$ and (*3*, *4*) $La_{0.6}Sr_{0.2}Mn_{1.2}O_{3\pm\delta}$ ceramics (*1*, *3*) in the initial state and (*2*, *4*) upon additional annealing in oxygen.

heated at a rate of 1 K/min. At the moments of measurement, the heating was suspended and the sample temperature was stabilized. The X-ray diffraction measurements were performed in a range of sample temperatures from 300 to 1200 K. Then, the samples were additionally annealed in oxygen at 1073 K in a step regime and slowly cooled (also in an oxygen atmosphere) [6]. The annealed samples were also studied by high-temperature X-ray diffraction. Special attention was paid to measurements at the points close to the temperatures of metal–semiconductor (T_{ms}) and ferromagnet–paramagnet (T_c) phase transitions and to the peak of magnetoresistance (T_p).

According to the room-temperature X-ray diffraction data, the initial samples were practically single-phase and contained compounds of the close type (hausmannite and kurnakite phases). The structure of doped samples, as well as of the undoped ones [7], belonged to a rhombohedrally distorted $R\bar{3}c$ type.

The results of high-temperature X-ray diffraction measurements revealed an anomalous behavior of the lattice parameters (Fig. 2) near the temperatures of phase transitions. For the Sr-containing samples, the anomaly was observed in the temperature interval from 374 to 424 K; for the Pb-doped samples, the anomalies were observed at 900–1000 and 1150–1200 K. In these

temperature intervals, the lattice parameters of the samples exhibited violation of a relatively monotonic increase and showed a decrease with increasing temperature.

The anomalous behavior of the lattice parameter can be explained by dissolution of the cluster compounds in the matrix structure. This process is likely to be irreversible and nonequilibrium. We suggest that cooling of the samples may be accompanied by a partial restoration of clusters in the matrix structure, but this is not manifested in the X-ray diffraction patterns. In addition, it was found that the angle α changes toward 90°, which implies that the sample structure approaches a cubic (*Pm3m*) type.

The additional annealing in oxygen led to a significant increase in the lattice parameter: namely, from 7.706 to 7.782 Å (at 292 K) for $La_{0.6}Sr_{0.2}Mn_{1.2}O_{3\pm\delta}$ ($\frac{\Delta a}{a} = 0.9\%$) and from 7.798 to 7.853 Å (at 292 K) for $La_{0.6}Pb_{0.2}Mn_{1.2}O_{3\pm\delta}$ ($\frac{\Delta a}{a} = 0.7\%$). However, this was not accompanied by any significant changes in the magnetoresistance. Therefore, the annealing in oxygen does not influence the density of free charge carriers accounting for the CMR effect; that is, the increasing defectness of the sample structure does not lead to an increase in the magnetoresistance of doped lanthanum manganites.

REFERENCES

1. E. L. Nagaev, Usp. Fiz. Nauk **166**, 833 (1996) [Phys. Usp. **39**, 781 (1996)].
2. D. M. Edwards, Adv. Phys. **51**, 1256 (2002).
3. M. T. Causa, G. Alejandro, R. Zysler, *et al.*, J. Magn. Magn. Mater. **196–197**, 506 (1999).
4. V. P. Pashchenko, A. N. Ul'yanov, A. A. Shemyakov, *et al.*, Neorg. Mater. **35**, 1509 (1999).
5. V. P. Pashchenko, I. V. Zhikharev, V. K. Prokopenko, *et al.*, Metallofiz. Noveishie Tekhnol. **23**, 1309 (2001).
6. B. Ya. Sukharevskiĭ, I. V. Zhikharev, S. I. Khokhlova, *et al.*, Kristallografiya **35**, 727 (1990) [Sov. Phys. Crystallogr. **35**, 424 (1990)].
7. V. P. Pashchenko, S. I. Khartsev, O. P. Cherenkov, *et al.*, Neorg. Mater. **35**, 1509 (1999).

Translated by P. Pozdeev

Electronic and Optical Properties
of Granular Amorphous Carbon Films

V. N. Varyukhin, T. A. D'yachenko, V. D. Okunev*, N. N. Pafomov,
A. L. Plekhov, and E. I. Shemchenko

Donetsk Physicotechnical Institute, National Academy of Sciences of Ukraine, Donetsk, 83114 Ukraine
e-mail: * okunev@mail.fti.ac.donetsk.ua
Received October 12, 2004

Abstract—Amorphous carbon (a-C⟨N⟩) films on glass substrates are obtained by magnetron sputtering of a graphite target in nitrogen. The temperature dependence of the electric conductivity ($\ln \sigma \sim T^{1/2}$ at temperatures $T < 280$ K) of the films is typical of a granular structure. The results of measurements of the thermo emf, conductivity, and optical absorption of the a-C⟨N⟩ films suggest that the granular structure comprises nanodimensional clusters of γ-carbon phase with metallic conductivity distributed in a graphitelike carbon matrix. The concentration of such clusters in the matrix increases with the substrate temperature. © *2005 Pleiades Publishing, Inc.*

Amorphous carbon films, offering a unique combination of properties, have received considerable attention of researchers [1]. Good prospects are related, in particular, with nitrogen-doped diamondlike carbon films. The main effort in this direction of research is devoted to the development of technology of β-C_3N_4 carbon nitride coatings [2–4].

In the problem of obtaining diamondlike carbon films, of special interest from the standpoint of nanoelectronics is the formation of clusters with metallic conductivity in a dielectric matrix [5, 6]. The widely used approach consists in using the tendency to clusterization known for carbon atoms with the same type of coordination (sp^3, sp^2, and sp hybrid states) [7, 8]. In the presence of linear (chain), planar, and diamondlike structural fragments, the carbon base structure of the films plays the role of a stabilizing matrix. Occurring in this matrix, metallic clusters possess a minimum density of surface states and acquire both thermodynamic and chemical stability [5]. The results obtained in this study show that a system of clusters possessing metallic conductivity in a dielectric matrix of amorphous carbon can be obtained without introducing metal impurities, merely by synthesizing carbon films in a nitrogen atmosphere.

The nitrogen-containing amorphous carbon (a-C⟨N⟩) films with thicknesses from 0.9 to 5.0 μm were obtained on glass substrates by magnetron sputtering of a graphite target in pure nitrogen at a pressure of 75−100 mTorr. The films deposited under such conditions usually possess a graphitelike structure with sp^2 bonds [9]. The substrate temperature T_s during deposition was varied from 20 to 450°C.

In the electric fields $F < 30$ V/cm, the samples had linear current–voltage (I–V) curves and exponential temperature dependences of the conductivity,

$$\sigma \approx \exp\left[-\left(\frac{T_0}{T}\right)^{\xi}\right], \tag{1}$$

with an exponent of $\xi \simeq 1/2$ (Fig. 1). According to a differential method based on the analysis of the dimensionless activation energy $\omega(T) = T^{-1}\partial\ln\rho(T)/\partial T^{-1} = m + \xi(T_0/T)^{\xi}$ (where $\rho = 1/\sigma$) [10], the exact values of the
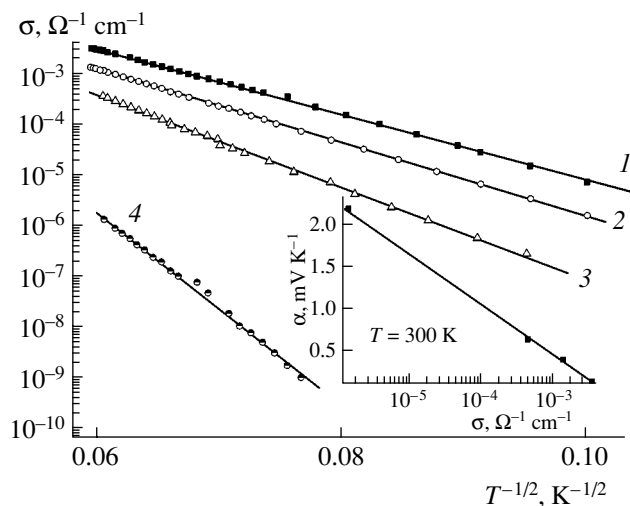

Fig. 1. Temperature dependences of the conductivity σ of a-C⟨N⟩ films deposited at various substrate temperatures $T_s = 450$ (*1*), 350 (*2*), 250 (*3*), and 20°C (*4*). The inset shows a plot of the thermo emf ($T = 300$ K) versus conductivity ($T = 300$ K) for the same samples.
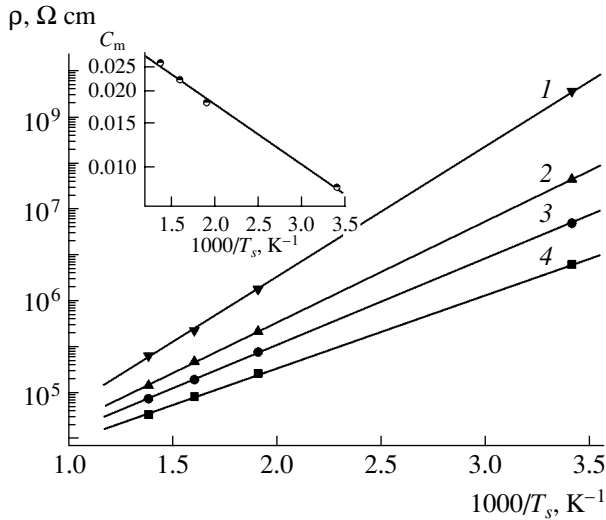
Fig. 2. Plots of resistivity ρ versus substrate temperature T_s for various temperatures $T = 156$ (*1*), 204 (*2*), 237 (*3*), and 277 K (*4*). The inset shows a plot of the metallic phase concentration C_m versus T_s for the same temperatures.

exponent ξ for the samples deposited at $T_s = 20$, 250, 350, and 450°C were 0.48, 0.45, 0.46, and 0.45, respectively. A simpler method [11], based on the analysis of the function $\ln(\ln\rho) = f(\ln T) = \xi \ln T_0 - \xi \ln T + \ln[1 + (T/T_0)^\xi \ln\rho_0]$, gives for the same temperatures the exponents $\xi = 0.49$, 0.46, 0.46, and 0.45, respectively, which are also close to 0.5. The dependence of $\ln\sigma \sim -T^{-1/2}$ is observed for $T < 280$ K. As the substrate temperature T_s is increased further, the conductivity grows by four ($T = 300$ K) or even seven ($T = 100$ K) orders in magnitude and the parameter T_0 decreases from 2×10^5 to 2×10^4 K.

The nature of the $\xi = 1/2$ law is most probably related to the electron tunneling between small clusters with metallic conductivity, which is typical of granular media [12]. An alternative mechanism (also with $\xi = 1/2$) of conductivity in disordered systems with a Coulomb gap in the spectrum of states is operative at temperatures $T < 80$ K [13, 14], for which the gap is not smeared by thermal excitations.

In the space of dimensionality ν, the mechanism of conductivity by hopping with variable range yields $\sigma(T) = \sigma_0 \exp[-(T_0/T)^\xi]$ with $\xi = 1/(\nu + 1)$ [15], which also corresponds to $\xi = 1/2$ for $\nu = 1$. However, one-dimensional hopping conductivity in carbynes with one-dimensional chains and very high resistivity is observed for $T < 40$ K [16].

Describing the resistance of films in terms of a simple model [17] of charge carrier tunneling between metallic clusters having a linear size D and a thickness γD and forming a regular lattice, we can write $\rho = \rho_0 \exp(d/d_0)$, where $d = D[(C_m/\gamma)^{-1/3} - 1]$ is the average distance between metallic clusters. For a cluster con-

centration of C_m, we have $d = D[(C_m/\gamma)^{-1/3} - 1]$ and, hence,

$$\rho = \rho_0 \exp\left[\frac{D}{d_0}\left(\frac{1}{\gamma}C_m\right)^{-1/3} - 1\right]. \qquad (2)$$

The observed decrease of ρ with increasing substrate temperature T_s (for the same $\rho(T)$ behavior of the type $\ln\rho \sim T^{-1/2}$) [12] suggests that

$$C_m = C_m^0 \exp\left(-\frac{T^*}{T_s}\right), \qquad (3)$$

where T^* is a parameter independent of T_s. Then,

$$\rho = \rho_0 \exp\left\{\frac{D}{d_0}\left[\left(\frac{1}{\gamma}C_m\right)^{-\frac{1}{3}} - 1\right]\right\}$$

$$= \rho_0 \left\{\exp\left[\left\{\frac{1}{\gamma}C_m^0\exp\left(-\frac{T^*}{T_s}\right)\right\}^{-\frac{1}{3}} - 1\right]\right\}^{\frac{D}{d_0}}. \qquad (4)$$

Expanding the exponent and using the first approximation $\exp(x) \simeq 1 + x$, we obtain

$$\rho \cong \rho_0\left\{1 + \left[\frac{1}{\gamma}C_m^0\exp\left(-\frac{T^*}{T_s}\right)\right]^{-\frac{1}{3}} - 1\right\}^{\frac{D}{d_0}}$$

$$= \rho_0\left[\left(\frac{1}{\gamma}C_m^0\right)\exp\left(-\frac{T^*}{T_s}\right)\right]^{-\frac{D}{3d_0}}. \qquad (5)$$

For the model under consideration, ρ must exponentially increase with decreasing substrate temperature T_s,

$\log\rho = \log\rho_0 - D/3d_0[\log(C_m^0/\gamma) - T^*/2.3T_s]$, in agreement with experiment (Fig. 2).

The values of C_m were estimated using the Mott concept of a minimum metallic conductivity [15]. According to this, $\sigma_{min} = \pi e^2/4z\hbar a[B/V_0]^2_{crit}$, where z is the coordination number, a is the distance between impurity centers, V_0 is the amplitude of the random potential, and B is the band width [15]. For the films under consideration, we have $\sigma_{min} \simeq 300 \ \Omega^{-1} \ cm^{-1}$, which is 5–10 orders of magnitude greater than the experimental values of conductivity. The concentration of the metallic clusters can be estimated using the values of σ_{min}, the critical concentration C_m^{crit} of the metallic phase (percolation threshold) for thin-film systems, and data on the electric conductivity. Assuming that σ is close to σ_{min} near the percolation threshold $C_m^{crit} = 0.5$ characteristic of thin-film samples [13, 18], and that

tunneling is the only mechanism of electric conductivity in the samples studied, so that $\sigma_i = \sigma_0\exp\{-D/d_0[(C_m^{(i)}/\gamma)^{-1/3} - 1]\}$ $(i = 1, 2, 3, 4)$, we obtained a system of equations

$$(C_m^{(i)})^{-\frac{1}{3}} - (C_m^{(j)})^{-\frac{1}{3}} = \frac{d_0}{D}\left(\frac{1}{\gamma}\right)^{-\frac{1}{3}}\ln\left(\frac{\sigma_j}{\sigma_i}\right), \qquad (6)$$

and graphically determined $(C_m^{(i,j)})$. The values of $1/\gamma = 2$ and $D/d_0 = 6$ were selected so as to match the tunneling $(d = 0)$ and percolation $(C_m^{crit} = 0.5)$ approximations at the threshold. The calculations were performed for the experimental values of σ determined at $T = 277$ K. For $d = 0$, we used the calculated value of $\sigma_{min} = 300$ Ω^{-1} cm^{-1}. As can be seen in the inset to Fig. 2, $C_m = 8.8 \times 10^{-3}$–2.8×10^{-2} and exponentially depends on $1/T_s$ (in agreement with formula (3) and Fig. 2).

The optical absorption edge is smeared (Fig. 3) and exhibits a distorted Urbach shape, $\alpha(\hbar\omega) = \alpha_0\exp(\Gamma\hbar\omega)$, which is determined by the built-in electric fields [19–22]. The coefficient $\Gamma = d(\ln\alpha)/d(\hbar\omega) = 2.4$–$3.7$ eV^{-1} is close to the values for amorphous CdGeAs^2⟨Fe⟩ films (1.6–2.9 eV^{-1}) [19] containing metallic clusters in a diamondlike matrix. For undoped amorphous semiconductors, $\Gamma = 15$–22 eV^{-1} [15]. The $\alpha(\hbar\omega)$ curves exhibit no periodic variations (interference pattern) characteristic of optically homogeneous media. For the carbon films, such a smoothened interference pattern in the spectra is reliable evidence of their spatial inhomogeneity [6] and is usually related to metallic nanoclusters dispersed in a dielectric matrix [5, 6]. The optical spectra were measured in the range of $\hbar\omega < 1.4$ eV, where the absorption due to the diamondlike structure is absent and the main role is played by the clusters with metallic conductivity.

The peculiarities observed in the spectra at $\hbar\omega \simeq 0.6$ and 0.8 eV are most likely related to the excitation of surface plasmons in the metallic clusters [5, 6, 23, 24]. The difference spectra (Fig. 3, curve *3*) reveal two additional weak maxima at $\hbar\omega \simeq 0.7$ and 1.0 eV and exhibit a sharp growth of $\Delta\alpha$ for $\hbar\omega > 1.2$ eV.

The results of thermo emf measurements showed that the amorphous films are characterized by clearly pronounced hole conductivity. The absolute values of the Seebeck coefficient η show a logarithmic decrease with increasing σ (see the inset to Fig. 1). This agrees with the behavior of classical semiconductors for which $\eta = k/e\{\varphi(\zeta) + \ln[2(2\pi m^*kT)^{3/2}/ph^3]\}$, where φ is the function of $\zeta = (6\rho_I/\rho_L)^{1/2}$; ρ_I and ρ_L are the resistivity components due to the scattering on impurities and lattice vibrations, respectively; p and m^* are the hole density and effective mass, respectively; and k is the Boltzmann constant. In a simplified case, $\varphi(\zeta) \simeq 2$ [25].
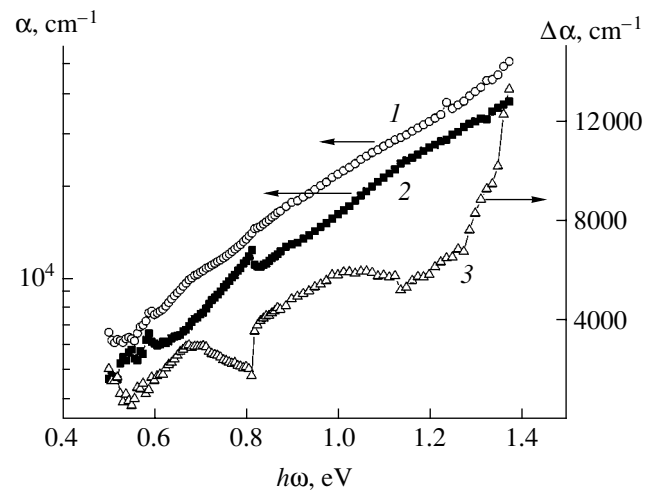

Fig. 3. Optical absorption spectra of the a-C⟨N⟩ films deposited at $T_s = 350$ (*1*) and $250°$C (*2*); curve *3* is the difference spectrum $\Delta\alpha(\hbar\omega) = \alpha(T_s = 350°\text{C}) - \alpha(T_s = 250°\text{C})$.

The technology of a-C⟨N⟩ films excluded the appearance of uncontrolled impurities in significant amounts. The most probable source of holes is nitrogen, whose solubility increases with the film deposition temperature. The hole conductivity is possible for all configurations of bonds, but the conductivity σ must exceed σ_{min}. Taking into account the susceptibility of charge carriers to localization and the high resistivity of carbynes, the formation of a hole metallic phase involving one-dimensional chains with sp hybrid bonds is unlikely [16]. Although the incorporation of trivalent nitrogen into diamondlike clusters with sp^3 configuration of bonds is a classical scheme of hole formation in diamondlike semiconductors, the metallic conductivity in such a system is hardly possible. Thus, the most probable factor accounting for the metallic conductivity in the films studied is the formation (under the action of nitrogen) of small γ-carbon clusters [26]. The appearance of metallic conductivity in amorphous substances with diamondlike structure under the action of impurities is well known. The corresponding change in the local structure is accompanied by an increase in the coordination number from 4 to 12 [19, 27].

REFERENCES

1. F. W. Smith, J. Appl. Phys. **55**, 764 (1984).

2. A. Y. Liu and M. L. Cohen, Science **245**, 841 (1989).

3. H. Sjostrom, S. Stafstrom, M. Boman, *et al.*, Phys. Rev. Lett. **75**, 1336 (1995).

4. E. I. Shemchenko, R. V. Shalaev, and E. G. Pashinskaya, Fiz. Tekh. Vys. Davleniĭ **11**, 83 (2001).

5. E. A. Smorgonskaya, T. K. Zvonareva, E. I. Ivanova, and I. I. Novak, Fiz. Tverd. Tela (St. Petersburg) **45**, 1579 (2003) [Phys. Solid State **45**, 1658 (2003)].

6. V. I. Ivanov-Omskiĭ, I. N. Krivorotov, and S. G. Yastrebov, Zh. Tekh. Fiz. **65** (9), 121 (1995) [Tech. Phys. **40**, 930 (1995)].

7. V. I. Ivanov-Omskiĭ, A. V. Tolmachev, and S. G. Yastrebov, Fiz. Tekh. Poluprovodn. (St. Petersburg) **35**, 227 (2001) [Semiconductors **35**, 220 (2001)].

8. A. Ilie, A. C. Ferrari, T. Yagi, *et al.*, J. Appl. Phys. **90**, 2024 (2001).

9. S. E. Rodil, A. C. Ferrari, J. Robertson, and W. I. Milne, J. Appl. Phys. **89**, 5425 (2001).

10. A. G. Zabrodskiĭ and K. N. Zinov'eva, Zh. Éksp. Teor. Fiz. **86**, 727 (1984) [Sov. Phys. JETP **59**, 425 (1984)].

11. N. B. Brandt, S. V. Demishev, A. A. Dmitriev, *et al.*, Zh. Éksp. Teor. Fiz. **86**, 1446 (1984) [Sov. Phys. JETP **59**, 847 (1984)].

12. E. Z. Meilikhov, Zh. Éksp. Teor. Fiz. **115**, 1484 (1999) [JETP **88**, 819 (1999)].

13. B. I. Shklovskii and A. L. Éfros, *Electronic Properties of Doped Semiconductors* (Nauka, Moscow, 1979; Springer-Verlag, New York, 1984).

14. A. V. Dvurechenskiĭ, I. A. Ryazantsev, V. A. Dravin, and A. I. Yakimov, Pis'ma Zh. Éksp. Teor. Fiz. **43**, 46 (1986) [JETP Lett. **43**, 59 (1986)].

15. N. F. Mott and E. A. Davis, *Electronic Processes in Non-Crystalline Materials* (Clarendon Press, Oxford, 1971).

16. S. V. Demishev, A. A. Pronin, V. V. Glushkov, *et al.*, Pis'ma Zh. Éksp. Teor. Fiz. **78**, 984 (2003) [JETP Lett. **78**, 511 (2003)].

17. V. D. Okunev, Z. A. Samoilenko, A. Abal'oshev, *et al.*, Phys. Lett. A **325**, 79 (2004).

18. A. B. Khanikaev, A. B. Granovskiĭ, and J. P. Clerc, Fiz. Tverd. Tela (St. Petersburg) **44**, 1537 (2002) [Phys. Solid State **44**, 1611 (2002)].

19. V. D. Okunev, Fiz. Tverd. Tela (Leningrad) **34**, 1263 (1992) [Sov. Phys. Solid State **34**, 667 (1992)].

20. V. L. Bonch-Bruevich, Usp. Fiz. Nauk **140**, 583 (1983) [Sov. Phys. Usp. **26**, 664 (1983)].

21. D. Redfield, Solid State Commun. **44**, 1347 (1982).

22. M. Silver, L. Pautmeier, and H. Bässler, Solid State Commun. **72**, 177 (1989).

23. Yu. I. Petrov, *Physics of Small Particles* (Nauka, Moscow, 1984) [in Russian].

24. U. Kreibig, J. Phys. F **4**, 999 (1974).

25. P. I. Baranskiĭ, V. P. Klochkov, and I. V. Potykevich, *Semiconductor Electronics* (Naukova Dumka, Kiev, 1975) [in Russian].

26. L. S. Palatnik, M. B. Guseva, V. G. Gabaev, *et al.*, Zh. Éksp. Teor. Fiz. **87**, 914 (1984) [Sov. Phys. JETP **60**, 520 (1984)].

27. V. D. Okunev and Z. A. Samoilenko, Pis'ma Zh. Éksp. Teor. Fiz. **53**, 42 (1991) [JETP Lett. **53**, 44 (1991)].

Translated by P. Pozdeev

Spatiotemporal Chaos Synchronization in Beam–Plasma Systems with Supercritical Current

P. V. Popov, R. A. Filatov, A. A. Koronovskiĭ, and A. E. Hramov*,[1]

Saratov State University, Saratov, Russia
* e-mail: aeh@cas.ssu.runnet.ru
Received October 15, 2004

Abstract—It is established that coupled beam–plasma systems with supercritical current can feature the phenomenon of chaotic synchronization. As the coupling between subsystems increases, a distributed beam–plasma system exhibits the transition from asynchronous behavior via phase synchronization to the state of complete chaotic synchronization. The phenomenon of chaotic synchronization is studied using a method developed previously on the basis of the introduction of a continuous manifold of phases of the chaotic signal. © 2005 Pleiades Publishing, Inc.

In recent years, the phenomenon of synchronization of chaotic dynamical systems with small numbers of the degrees of freedom has been extensively studied [1]. According to modern classification, there are several types of chaotic synchronization, including generalized [2], phase [1], lag [3], and complete synchronization [4]. The interest in these phenomena is related, in particular, to the possibility of data transmission by means of chaotic oscillations [5]. The generalized synchronization implies that there exists a certain function $\mathbf{F}[\mathbf{x}_1(t)]$ relating the states of chaotic oscillators such that $\mathbf{x}_2(t) = \mathbf{F}[\mathbf{x}_1(t)]$, where $\mathbf{x}_{1,2}$ are the state vectors of the two coupled systems. The phase synchronization is described in terms of the phase $\phi(t)$ of a chaotic signal and implies that the phases of the chaotic signals are entrained, while their amplitudes remain uncorrelated and appear chaotic. By the lag synchronization, we imply a regime in which the dynamics of one subsystem is characterized by a certain delay time τ relative to another: $\mathbf{x}_1(t) \approx \mathbf{x}_2(t - \tau)$. Finally, the complete synchronization means fully identical dynamics of two chaotic oscillators: $\mathbf{x}_1(t) \approx \mathbf{x}_2(t)$.

Previously, it has been shown [6, 7] that the generalized, phase, lag, and complete synchronization regimes are closely related, being essentially various manifestations of the same type of synchronous dynamics of coupled oscillators, referred to as the time scale synchronization. The character of a particular regime (featuring phase, lag, or complete synchronization) is determined by the number of synchronized time scales s introduced by means of a continuous wavelet transform [8]. Since the time scale s is related to a certain frequency, the synchronization of chaotic oscillations implies the appearance of phase coupling between the components ω of the Fourier spectra $S(\omega)$ [9].

As was noted above, the main results in investigations of the chaotic synchronization were obtained for the dynamical systems with a small number of degrees of freedom. However, it would also be of interest to study this phenomenon in spatially distributed systems featuring chaotic behavior. Most of the investigations in this direction were performed for the phenomenological models of systems comprising lattices of coupled oscillators [10, 11] or standard equations in partial derivatives (e.g., of the Ginzburg–Landau [12, 13] or Kuramoto–Sivashinsky [14] types). Detailed investigations of the chaotic synchronization in beam–plasma systems were very few (e.g., [15]). The transitions between different types of chaotic synchronization in such systems were not studied, and the analogies with these phenomena known in systems with a small number of degrees of freedom have not been revealed so far.

This paper reports on the results of investigation of the chaotic synchronization in coupled beam–plasma systems with supercritical current representing hydrodynamical models of the Pierce diode [16, Lecture 4], which are of considerable interest as the models of plasma systems featuring various types of chaotic behavior [16, 18–23].

In a model Pierce diode, an initially monoenergetic electron beam with a constant space charge density (neutralized by an immobile ion background) moves between two grounded grids. The only control parameter determining the system dynamics is the Pierce parameter $\alpha = \omega_p L / v_0$ representing the unperturbed angle of electron motion (ω_p is the plasma frequency, L is the distance between grids, and v_0 is the initial electron velocity at the system input). For $\alpha > \pi$, the so-called Pierce instability is developed in the system that leads to the formation of a virtual cathode and the
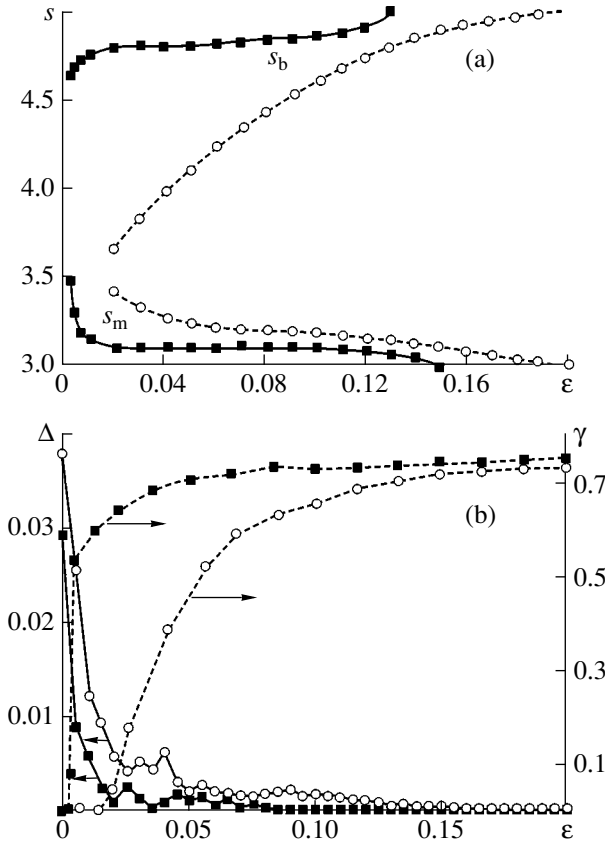

Fig. 1. Plots of (a) the lower (s_m) and upper (s_b) boundaries of the interval of synchronized time scales and (b) the parameter of identity (Δ) and relative energy (γ) of the synchronized spatiotemporal oscillations versus coupling parameter ε for the two coupled Pierce diodes with small ($\alpha_1/\pi = 2.860$, $\alpha_2/\pi = 2.861$ (■)) and large ($\alpha_1/\pi = 2.860$, $\alpha_2/\pi = 2.858$ (○)) detunings.

establishment of a multiflow state in the beam (for details, see [16, 22]). However, a complete transmission of the electron beam is possible for $\alpha \sim 3\pi$, which makes possible description of the system within the framework of a hydrodynamical approximation [16, 18, 20]. This description shows that various types of chaotic oscillations can be observed in this beam–plasma system [16–20, 23].

Let us consider two coupled Pierce diodes described within the framework of the hydrodynamical approximation by a self-consistent system including the equation of motion, the equation of continuity, and the Poisson equation in dimensionless variables [16]

$$\frac{\partial v_{1,2}}{\partial t} + v_{1,2}\frac{\partial v_{1,2}}{\partial x} = \frac{\partial \varphi_{1,2}}{\partial x}, \tag{1}$$

$$\frac{\partial \rho_{1,2}}{\partial t} + v_{1,2}\frac{\partial \rho_{1,2}}{\partial x} + \rho_{1,2}\frac{\partial v_{1,2}}{\partial x} = 0, \tag{2}$$

$$\frac{\partial^2 \varphi_{1,2}}{\partial x^2} = \alpha_{1,2}^2(\rho_{1,2} - 1), \tag{3}$$

with the boundary conditions

$$v_{1,2}(0, t) = 1, \quad \rho_{1,2}(0, t) = 1, \quad \varphi_{1,2}(0, t) = 0, \tag{4}$$

where subscripts 1 and 2 refer to the first (master) and second (slave) systems, respectively. Equations (1)–(4) for the hydrodynamical model of the Pierce diode are written in the dimensionless variables of the space charge field potential φ, charge density ρ, electron beam velocity v, spatial coordinate x, and time t (for details, see [16]).

The coupling between the two systems under consideration is provided through variation of the dimensionless potential at the right-hand boundaries of the systems:

$$\varphi_{1,2}(x = 1.0, t)$$
$$= \varepsilon(\rho_{2,1}(x = 1.0, t) - \rho_{1,2}(x = 1.0, t)), \tag{5}$$

where ε is the coupling parameter and $\rho_{1,2}(x = 1.0, t)$ are the oscillations of the dimensionless space charge density at the system output. In what follows, we will consider the dynamics of the system at a fixed value of the parameter α_1 ($\alpha_1 = 2.860\pi$) for the variable control parameter α_2.

The results of investigations show that weak detuning between coupled chaotic systems leads to the establishment of a time scale synchronization, which can be determined by introducing a continuous manifold of phases $\phi_s(t)$ of the chaotic signal on various time scales s with the aid of a continuous wavelet transform [6, 7]. The time series of the coupled systems were analyzed in terms of chaotic oscillations in the space charge densities $\rho_{1,2}(x = 0.2, t)$.

The dynamics of the coupled systems under consideration is illustrated in Fig. 1a constructed for $\alpha_1 = 2.860\pi$ and $\alpha_2 = 2.861\pi$, which shows the variation of the range of synchronous scales s_m and s_b with an increase in the coupling parameter ε [6]. As can be seen, time scales on which the system dynamics is synchronized appear at $\varepsilon > 0.0007$. It was demonstrated previously [7] that this state corresponds to phase synchronization of the chaotic oscillations. As the coupling parameter ε grows, the interval of synchronized scales increases and at $\varepsilon \approx 0.08$–0.1 the system dynamics is synchronized in virtually the entire range of time scales. Here, the coupled beam-plasma systems occur in a regime close to the state of lag synchronization with a delay time of $\tau \approx 0.07$. The further growth in ε leads to a decrease in the delay between oscillations, and the system tends to the state of complete chaotic synchronization characterized by nearly identical dynamics of each system ($\tau \approx 0$).

At a greater detuning of the parameters of coupled beam-plasma systems, which corresponds to a significantly more complex spectral composition of oscillations in the electron beam, the onset of synchronism between the time scales is observed for greater values of the coupling parameter. Figure 1a also shows the corresponding boundaries $[s_m, s_b]$ in the case of $\alpha_1 = 2.860\pi$ and $\alpha_2 = 2.858\pi$. As ε increases, the coupled systems tend to the state of complete chaotic synchronization.

The degree of identity of the spatiotemporal behavior oscillations in the two distributed systems is conveniently analyzed as dependent on ε in terms of the parameter Δ defined as [13]

$$\Delta = \langle |\rho_1(x, t) - \rho_2(x, t)| + |v_1(x, t) - v_2(x, t)| + |\phi_1(x, t) - \phi_2(x, t)| \rangle, \quad (6)$$

where the angle brackets $\langle \ldots \rangle$ denote averaging over both time and space. The results of this analysis are illustrated in Fig. 1b, which shows that the function $\Delta(\varepsilon)$ rapidly decreases and tends to zero with increasing ε. As can be seen from Fig. 1b, the value of Δ for a greater detuning between the two beam–plasma systems ($\circ$) remains nonzero (yet being sufficiently small for $\varepsilon > 0.17$) in contrast to the case of small detuning ($\blacksquare$) where Δ practically vanishes. It is the oscillation regimes with $\Delta(\varepsilon) \approx 0$ which are referred to as the states of complete chaotic synchronization.

An important energy characteristic of the synchronization of coupled chaotic systems is provided by the measure of synchronization introduced previously [6, 7] and defined as the energy fraction γ of the wavelet spectrum corresponding to the synchronized time scales (for details, see [6]). Figure 1b shows the $\gamma(\varepsilon)$ curves for the two sets of control parameters $\alpha_{1,2}$ considered above. As can be seen, an increase in the coupling parameter is accompanied by an increase in the fraction of energy of the spatiotemporal oscillations corresponding to the synchronized time scales.

Figure 2 shows the boundary of the region of complete chaotic synchronization on the plane of control parameters (α_2, ε) for the constant value of $\alpha_1 = 2.861\pi$. As can be seen, the coupled systems exhibit complete synchronization for any detuning between the control parameters $\alpha_{1,2}$ for a sufficiently large coupling parameter. This refers both to weakly chaotic oscillations in the case of small detuning and to the well developed chaos in systems with strongly different control parameters. Minimum values of the coupling parameter for which the regime of complete chaotic synchronization is possible are naturally observed for weakly decoupled subsystems.

To summarize, we have demonstrated for the first time that coupled beam–plasma systems with supercritical current (coupled Pierce diodes) may feature sequential establishment of different regimes of chaotic
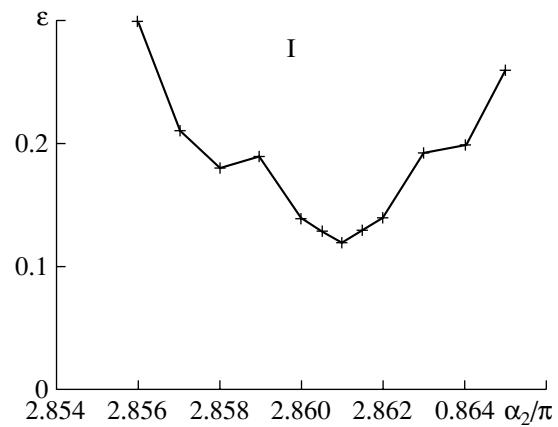

Fig. 2. The boundary of the region (I) of complete chaotic synchronization between two coupled distributed beam–plasma systems (Pierce diodes) on the plane of control parameters $(\alpha_2/\pi, \varepsilon)$ for the constant value of $\alpha_1 = 2.861\pi$.

synchronization (from phase to complete), which can be described as various cases of the time scale synchronization [6, 7]. The possibility of establishing the regime of complete synchronization of chaotic spatiotemporal oscillations in beam–plasma systems implies that such autooscillatory media can be used in systems of data transmission in the microwave range.

REFERENCES

1. A. Pikovsky, M. Rosenblum, and J. Kurths, *Synchronization: A Universal Concept in Nonlinear Sciences* (Cambridge Univ. Press, Cambridge, 2001).

2. N. Rulkov, M. Sushchik, L. Tsimring, and H. Abarbanel, Phys. Rev. E **51**, 980 (1995).

3. M. Rosenblum, A. Pikovsky, and J. Kurths, Phys. Rev. Lett. **78**, 4193 (1997).

4. L. Pecora, T. Carroll, G. Jonson, and D. Mar, Chaos **7**, 520 (1997).

5. A. S. Dmitriev and A. I. Panas, *Dynamic Chaos: Novel Information Carriers for Communication Systems* (Fizmatlit, Moscow, 2002) [in Russian].

6. A. A. Koronovskiĭ and A. E. Hramov, Pis'ma Zh. Éksp. Teor. Fiz. **79**, 391 (2004) [JETP Lett. **79**, 316 (2004)].

7. A. E. Hramov and A. A. Koronovskiĭ, Chaos **14**, 603 (2004).

8. A. A. Koronovskiĭ and A. E. Hramov, *Continuous Wavelet Analysis and Its Applications* (Fizmatlit, Moscow, 2003) [in Russian].

9. A. A. Koronovskiĭ, O. I. Moskalenko, and A. E. Hramov, Pis'ma Zh. Éksp. Teor. Fiz. **80**, 25 (2004) [JETP Lett. **80**, 20 (2004)].

10. L. Kosarev, Z. Tasev, T. Stojanovski, and U. Parlits, Chaos **7**, 635 (1997).

11. I. Leyva, E. Allaria, S. Boccaletti, and F. T. Arecchi, Phys. Rev. E **68**, 066209 (2003).

12. S. Boccaletti, J. Bragard, F. T. Arecchi, and H. Mancini, Phys. Rev. Lett. **83**, 536 (1999).

13. J. Bragard, F. T. Arecchi, and S. Boccaletti, Int. J. Bifurcation Chaos Appl. Sci. Eng. **10**, 2381 (2000).

14. Z. Tasev, L. Kocarev, L. Junge, and U. Parlitz, Int. J. Bifurcation Chaos Appl. Sci. Eng. **10**, 869 (2000).

15. E. Rosa, W. Pardo, C. Ticos, *et al.*, Int. J. Bifurcation Chaos Appl. Sci. Eng. **10**, 2551 (2000).

16. D. I. Trubetskov and A. E. Hramov, *Lectures on Microwave Electronics for Physicists* (Fizmatlit, Moscow, 2003), Vol. 1 [in Russian].

17. J. Pierce, J. Appl. Phys. **15**, 721 (1944).

18. B. Godfrey, Phys. Fluids **30**, 1553 (1987).

19. S. Kuhn and A. Ender, J. Appl. Phys. **68**, 732 (1990).

20. H. Matsumoto, H. Yokoyama, and D. Summers, Phys. Plasmas **3**, 177 (1996).

21. T. Klinger *et al.*, Phys. Plasmas **8**, 1961 (2001).

22. M. V. Kuzelev, A. A. Rukhadze, and P. S. Strelkov, *Relativistic Plasma Microwave Electronics* (Bauman Moscow State Technical University, Moscow, 2002) [in Russian].

23. A. E. Hramov and I. S. Rempen, Int. J. Electron. **91**, 1 (2004).

Translated by P. Pozdeev

Propagation Losses in Curved Integrated Optical Waveguides Based on Oxidized Porous Silicon

V. P. Bondarenko[a,*], A. A. Klyshko[a], M. Balucani[b], and A. Ferrari[b]

[a] *Belarussian State University of Informatics and Radioelectronics, Minsk, Belarus*
[b] *La Sapienza University, Rome, Italy*
* e-mail: vitaly@bsuir.edu.by
Received October 13, 2004

Abstract—The propagation losses are evaluated for the first time in curved integrated (buried) optical waveguides (WGs) based on oxidized porous silicon. In the visible red range, the losses decrease from 20 to 5 dB per 90° bending (for about 0.4 dB/cm loss in the straight WG) when the WG curvature radius increases from 125 to 2500 μm. The main component of the total bending losses in WGs is related to the coupling loss on the passage from straight to curved WG parts. Additional losses are introduced by the regions of incompletely oxidized porous silicon on the walls of curved WGs. © 2005 Pleiades Publishing, Inc.

The integrated (buried) waveguides (WGs) based on oxidized porous silicon were originally developed in 1992 [1]. Provided that a low level of optical losses is reached, such WGs can be used in optoelectronic integrated circuits, silicon-based optical arrays, and sensors. The first samples of oxidized porous silicon WGs (OPSWGs) were characterized by optical losses on the order of a several dB/cm in the visible spectral range [2]. OPSWGs have been extensively studied [3–6]. Owing to optimization of the OPSWG technology, the optical losses in straight WGs were significantly reduced (to 0.4–0.5 dB/cm in the visible spectral range [7]). However, successful application of integrated OPSWGs is possible only provided that both straight and curved WGs with good characteristics can be fabricated.

This Letter reports on the synthesis of curved OPSWGs and the first characterization of propagation losses in these WGs.

The integrated OPSWGs were fabricated using a modified variant of the process described in [7]. The initial materials were (100)-oriented single crystal silicon wafers (KES-0.01 grade) with a resistivity of 0.01 Ω cm. After the standard cleaning by etching in a hydrogen peroxide–hydrochloric acid solution, the wafers were implanted with 60-keV antimony ions to a total dose of 250 μC/cm^2 in order to suppress the negative influence of swirl defects on the WG characteristics [8]. After implantation, the wafers were once again subjected to chemical etching and then oxidized in dry oxygen at 1220°C for the activation of antimony ions and the formation of a 0.5-μm-thick SiO$_2$ film. Then, the pattern of desired WG channels was created in the oxide film by means of conventional photolithography and plasma etching. The window width in the mask was 7 μm. The surface of silicon in the windows was selectively anodized in a mixture of 48/% HF and ethylene glycol (2 : 3, v/v). The WG core and the cladding layer were obtained using a two-stage anodizing procedure (40 mA/cm^2 for 4 min followed by 80 mA/cm^2 for 45 s). The final step was a three-stage thermal oxidation performed as described in [7]. The WG layer thickness was 7.5 μm, and the cladding layer was 2.5 μm thick. The WG width was 22 μm. The refractive indices of the core and cladding layers were 1.4575 and 1.4460, respectively (with a contrast of 0.78%).

The WG bending losses were studied using test WG matrices. Each matrix crystal contained 20 WGs with a 90° bending, whose radii varied from $R = 125$ to 2500 μm at a 125-μm step, and one reference straight WG. The level of bending losses was measured using an original method employing mirrors self-formed at the WG ends in the course of aniodization and oxidation [9]. Radiation of a He–Ne laser was sequentially introduced into each WG, beginning with the straight one, and the output radiation power was measured at the WG edge on the mirror-cleaved face. All WGs formed in the same test matrix differed only in the length and radius of the curved region and, hence, the relative bending losses could be determined by comparing the output signal powers.

Figure 1 shows the results of the optical loss measurements for twenty WGs with various radii of curvature. The curve has an exponential shape reflecting an increase in the propagation losses from 6 dB per 90° bending for $R = 2500$ μm up to 20 dB for the minimum radius. The losses in straight WGs did not exceed 0.4 dB/cm. The measurements were performed in the visible red range, where the OPSWGs operated in a multimode regime.

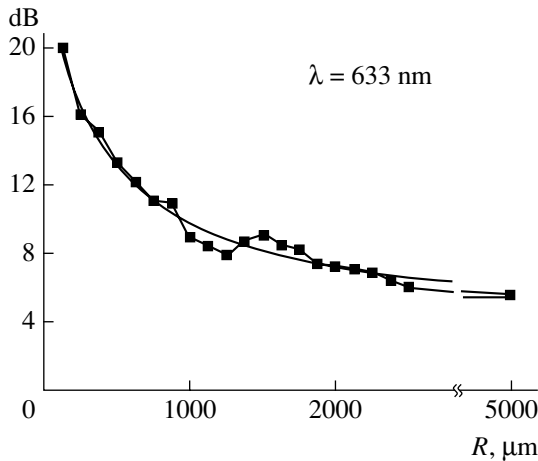As is known, silicon oxide based optical WGs with low index contrast guide light in the core due to the

Fig. 1. Experimental plot of the optical losses versus curvature radius for integrated OPSWGs.
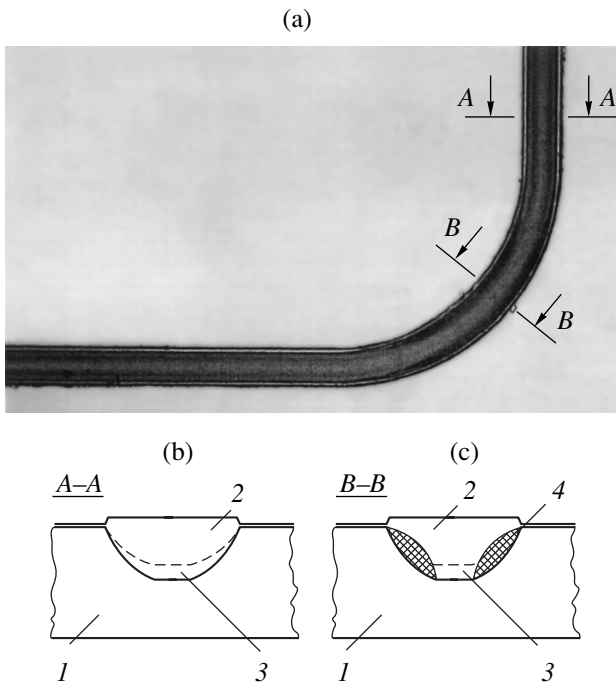
(a)

(b)   (c)

Fig. 2. (a) A microphotograph of an integrated OPSWG with a curvature radius of 125 μm; (b, c) schematic diagrams of the transverse sections in the (*A–A*) straight and (*B–B*) curved regions, respectively, showing (*1*) a silicon substrate, (*2*) the WG core, (*3*) the cladding layer, and (*4*) the regions of incompletely oxidized porous silicon.

total internal reflection and, hence, bending of the core may lead to significant optical losses. It was shown [10] that losses in the curved region of an optical WG consist of two main parts: (i) conversion losses at the mode coupling interfaces and (ii) radiation losses in the curved region. Thus, the data presented in Fig.1 represent total losses, including the double conversion losses (due to the mode conversion on the passage from straight to curved WG region and back) and the radiation losses per 90° bending.

The conversion losses are described in terms of the conversion loss factor c^2 characterizing the fundamental WG mode power transfer to high-order modes [10]. For multimode fiber, this quantity is given by the formula

$$c^2 = \left(\frac{\pi n_0 a^3}{\lambda^2 R} \right)^2,$$

where n_0 is the core refractive index, a is the core width, and R is the curvature radius. The values of c^2 significantly greater than unity are indicative of high conversion losses. In our OPSWGs, the c^2 factor was additionally increased as a result of relatively large WG width (compared to the R and λ values). Indeed, c^2 was about 21 even for $R = 2500$ μm and significantly increased with the curvature (with decreasing R). As for the pure bending losses, this contribution is small even in cases of $c^2 \gg 1$.

It should be noted that, even with allowance for high c^2 values, the losses in obtained curved OPSWGs have proved to be greater than expected. For comparison, in the silicon oxide WGs with a width of 6 μm, a depth of 6 μm, and an index contrast of $\Delta n = 0.75\%$ [11], the losses were below 0.1 dB for a curvature radius of 5000 μm. Assuming the dependence of losses on the curvature radius to be exponential and extrapolating the experimental curve to the values of R exceeding 10000 μm, we obtain not less than 4 dB per 90° bending. This result indicates that there are additional factors of optical losses in our OPSWGs.

The factor leading to additional losses in the curved regions of OPSWGs was established by visual microscopic examination of the samples. Figure 2a presents a microphotograph of an OPSWG with a curvature radius of 125 μm. The image reveals dark inhomogeneous bands at the WG walls. An analysis of the cleaved samples showed that these bands correspond to regions of incompletely oxidized porous silicon. Figures 2b and 2c show schematic diagrams of the transverse sections of straight and curved WGs. As can be seen, the incompletely oxidized regions are situated on the walls and partly involve the cladding layer. As is known, the light guided in straight portions of the optical WGs is confined predominantly to the core, while in curved regions a significant role is played by the quality of walls (cladding). The presence of incompletely oxidized porous silicon introduces additional inhomogeneity that results in additional scattering. We believe that the incomplete oxidation of porous silicon is caused by local changes in properties of the substrate material. Indeed, the process of anodizing through windows in the mask involves, besides the porous silicon formation in depth of the substrate, the lateral anodizing under the mask. The anodizing process has been well elaborated for silicon crystal orientations on the

straight portions of WGs, but a change in the orientation (such as in the curved regions) leads to the formation of porous silicon regions with different characteristics. Apparently, these regions are incompletely oxidized in the course of subsequent high-temperature oxidation.

The results presented above demonstrate the principal possibility to obtain curved integrated WGs based on oxidized porous silicon. In order to reduce the optical losses in such WGs to an acceptable level, it is necessary to eliminate the regions of incompletely oxidized porous silicon on the curved walls. An increase in the refractive index contrast (e.g., by doping the WG core with titanium) must improve the confinement of light in the core and, hence, additionally reduce the bending losses.

REFERENCES

1. V. Bondarenko, V. Varichenko, A. Dorofeev, *et al.*, Pis'ma Zh. Tekh. Fiz. **19** (7), 73 (1993) [Tech. Phys. Lett. **19**, 463 (1993)].

2. V. Bondarenko, A. Dorofeev, and N. Kazuchits, Microelectron. Eng. **28**, 447 (1995).

3. G. Maiello, S. La Monica, A. Ferrari, *et al.*, Thin Solid Films **297**, 311 (1997).

4. M. Takahashi and N. Koshida, J. Appl. Phys. **86**, 5274 (1999).

5. T. Benson, H. Arrand, P. Sewell, *et al.*, Mater. Sci. Eng., B **69**–**70**, 92 (2000).

6. N. Vorozov, L. Dolgyi, V. Yakovtseva, *et al.*, Electron. Lett. **36**, 722 (2000).

7. M. Balucani, V. Bondarenko, N. Vorozov, and A. Ferrari, Physica E **16**, 574 (2003).

8. M. Balucani, V. Bondarenko, N. Vorozov, and A. Ferrari, Physica E **16**, 586 (2003).

9. M. Balucani, V. Bondarenko, L. Dolgyi, *et al.*, Mater. Sci. Semicond. Process. **3**, 351 (2000).

10. E. A. J. Marcatili, Bell Syst. Tech. J. **48**, 2103 (1969).

11. M. Kawachi, Opt. Quantum Electron. **22**, 391 (1990).

Translated by P. Pozdeev

Phototropic Centers in Lasers Systems Based on Rare Earth Garnet Crystals

L. I. Shchepina*, O. V. Borodina, and L. I. Ruzhnikov

Institute of Applied Physics, Irkutsk State University, Irkutsk, Russia
* e-mail: schepina@api.isu.ru
Received October 12, 2004

Abstract—The emission from Cr^{3+} ions at 730 nm is enhanced under the action of the second harmonic radiation of a neodymium laser, while the intensity of emission at 1.54 μm from Cr^{4+} ions in tetrahedral positions remains unchanged. This result casts doubt on the interpretation of absorption bands at 0.775–1.26 μm and the luminescence bands at 1.103–1.67 μm in the spectra of rare earth garnets, which have been previously assigned to electron transitions in Cr^{4+} ions occupying tetrahedral positions in the garnet structure. © 2005 Pleiades Publishing, Inc.

The interest in phototropic centers in garnets is related to the fact that their absorption bands fall within the region of lasing transitions in Nd^{3+} ion, which is one of the most widely used laser ions. Garnet crystals have been successfully used for implementing the regimes of passive mode synchronization and passive Q switching in neodymium lasers and for establishing the possibility of obtaining effective lasers tunable in a wavelength range of 1.4–1.6 μm. Most researchers [1–4] believe that phototropic centers in garnets represent $(Cr^{4+})_{tetr}$, that is, tetravalent chromium ions replacing Al^{3+} or Ga^{3+} ions in garnet based crystals and occurring in a tetrahedral environment of oxygen ligands. These $(Cr^{4+})_{tetr}$ centers account for the absorption band peaked at 1.06 μm and for the luminescence in the 1.52–1.56 μm range [5]. Il'ichev *et al.* [6] were the first who expressed doubt in this interpretation and suggested an alternative model of the phototropic center, as Cr^{3+} surrounded by an unidentified defect. According to another standpoint, the phototropic centers are related to Cr^{2+} ions [7].

This study was aimed at obtaining additional information concerning the properties of phototropic centers and the processes involved in the interaction of rare earth (RE) garnets with high-power laser radiation.

The experiments were performed with single crystal RE garnets of two types: gadolinium scandium aluminum garnet (GSAG) doped with Ca^{2+} and Cr^{3+} ions ($Gd_3Sc_2Al_3O_{12}$) and gadolinium scandium gallium garnet (GSGG) doped with Cr^{3+} and Nd^{3+} ions ($Gd_3Sc_2Ga_3O_{12}$). Impurities uncontrolled in the course of crystal growth were determined by emission spectral analysis (see table). Since we are mostly interested in the nature of optical absorption in the vicinity of 1.06 μm, let us compare the absorption coefficients of GSAG-Ca^{2+},Cr^{3+} ($K = 9.45$ cm^{-1}) and GSGG-Cr^{3+},Nd^{3+} ($K = 6.9$ cm^{-1}). The concentrations of defects in the two crystals differ insignificantly (by a factor of ~1.37). Taking into account that no special preliminary measures (such as intentional Me^{2+} introduction and oxidative annealing in the course of growth) were taken for introducing Cr^{4+} into the GSGG crystal, it is impossible to assign the absorption at 1.06 μm entirely to the presence of Cr^{4+} ions related to the appearance of uncontrolled Me^{2+} impurities. The sample crystals were exposed to the coherent second harmonic (2ω) and fourth harmonic (4ω) radiation of a neodymium laser. The concentration of Cr^{3+} ions was determined using the intensity of photoluminescence (PL) at $\lambda_m = 730$ nm (for $\lambda_{ex} = 532$ nm) at the moment of excitation with the second harmonic of a YAG-Nd laser. Simultaneously, the concentration of Cr^{4+} ions was determined at the moment of laser action (by monitoring a change in the luminescence intensity at 1.54 μm for $\lambda_{ex} = 532$ nm and in the free lasing regime).

The content of impurities (%) in RE garnet crystals studied (by data of emission spectroscopy)

Crystal	Mg	Ca	Cu	Ti	Si	B
GSAG-Ca,Cr ($Gd_3Sc_2Al_3O_{12}$)	$<3 \times 10^{-4}$	0.1	2×10^{-4}–6×10^{-4}	–	$<10^{-3}$	–
GSGG-Cr,Nd ($Gd_3Sc_2Ga_3O_{12}$)	$<10^{-3}$	–	10^{-4}–3×10^{-4}	$<10^{-3}$	$\approx 10^{-3}$	10^{-3}

Using optical spectroscopy and polarization techniques, we obtained the following experimental results:

(1) The absorption spectra of samples exhibit signals corresponding to the excited states $^4T_2$ and $^4T_1$ (630 and 452 nm) of $(Cr^{3+})_{oct}$ ions; $^3T_2$ (520 nm) of $(Cr^{4+})_{oct}$ ions; and $^3T_1$ (660 nm), $^1A_1$ (504 nm), $^1T_2$ (475 nm), $^1T_1$ and $^3T_1$ (410 nm) of $(Cr^{4+})_{tetr}$ ions [2]. The PL spectra display a broad emission band at $\lambda = 730$ nm related to the transition from the excited state $^4T_2$ to the ground state $^4A_2$ of Cr^{3+} ions and another broad emission band ($\lambda = 1.54$ μm) excited in the region of 1.06 μm. An analysis of the spectra shows that chromium ions may occur in both Cr^{3+} and Cr^{4+} states, while no evidence of chromium in the divalent state was found.

(2) Additional information about the structure of phototropic centers was obtained by measuring the spectra of polarized emission from RE garnet crystals. Figure 1 shows the azimuthal dependence of the emission at $\lambda = 1.54$ μm and the degree of polarization for the $GSGG(Cr^{3+},Nd^{3+})$ sample. These data confirm that the emitting oscillator is oriented along a fourth-order (C_4) axis. As is known, the crystals of cubic symmetry (typical of the garnets studied) contain three such axes parallel to the cube edges. Therefore, three groups of linear oscillators with $\lambda_m = 1.54$ μm can align in these directions. This behavior is most likely for Cr^{3+} ions occurring in an octahedral environment, rather than for Cr^{4+} ions in a tetrahedral environment.

(3) Taking into account the forbidden bandwidths of the RE garnets studied (5.56–6.2 eV) and the photon energies of 4ω (4.66 eV) and 2ω (2.33 eV) modes of the YAG-Nd laser, it was possible to observe recharge of the impurity ions under the action of coherent laser radiation. Figure 2 shows the curves of the Cr^{3+} PL intensity versus time of irradiation with 4ω and 2ω harmonics of the YAG-Nd laser for both garnet crystals studied. In the course of laser action, the emission from Cr^{3+} ions in the $GSAG(Ca^{2+},Cr^{3+})$ crystal increases. A growth in the concentration of Cr^{3+} ions may take place as a result of the interaction of electrons with Cr^{4+} ions. If this were the case, we would observe a decrease in the concentration of Cr^{4+} ions. However, the curves in Fig. 2 show that the concentration of these ions remains unchanged. Another possible mechanism of the optical conversion is, for example, $Cr^{2+} + h \longrightarrow Cr^{3+}$. However, it was noted above that divalent chromium ions were not found in the garnet crystals studied. Therefore, the observed luminescence with a maximum at 1.54 μm excited in the region of 1.06 μm is not related to electron transitions in tetravalent chromium ions.

Let us consider the transformations of impurity ions in $GSGG(Cr^{3+},Nd^{3+})$ in more detail. The ionization potential of Cr^{3+} is 49.0 eV. The laser photon energies for the 4ω and 2ω modes are 4.66 and 2.33 eV, respectively. The multiphoton processes are unlikely, since
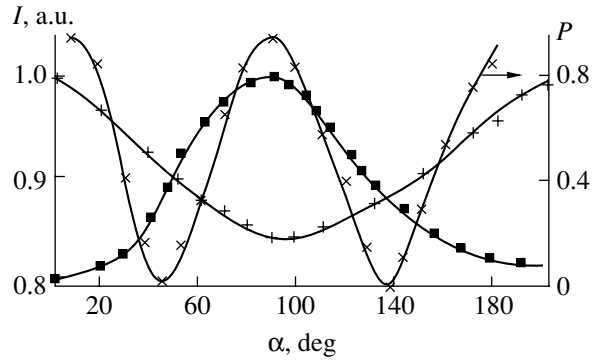

Fig. 1. Azimuthal dependences of the intensity I and the degree of polarization P of the PL at $\lambda = 1.54$ μm for the $GSGG(Cr^{3+},Nd^{3+})$ crystal.
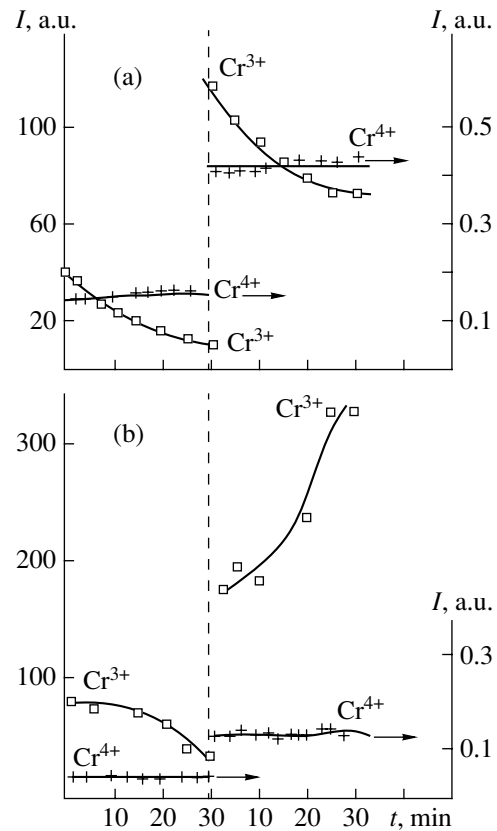

Fig. 2. Time variation of the intensity of PL from Cr^{3+} ($\lambda_m = 730$ nm) and Cr^{4+} ($\lambda_m = 1.54$ μm) ions in (a) $GSGG(Cr^{3+},Nd^{3+})$ and (b) $GSAG(Ca^{2+},Cr^{3+})$ crystals under the action of fourth (4ω, $t < 30$ min) and second (2ω, $t > 30$ min) harmonics of YAG-Nd laser.

their probabilities drop with an increasing number of photons. Therefore, the decay of Cr^{3+} ions is mediated by a hole jumping over the excited states of these ions. The efficiency of this decay is a quadratic function of the average power of the second harmonic radiation of the YAG-Nd laser. Thus, Cr^{3+} ions decay according to a

two-step mechanism. For Cr^{4+} ions incorporated into the RE garnet crystal lattice in the course of growth (as in GSAG-Ca,Cr crystals) or induced as a result of the laser action (as in GSGG-Cr,Nd crystals), the possible reactions are as follows: (i) $Cr^{4+} + e(Cr^{3+})^* \longrightarrow h\nu + Cr^{3+}$; (ii) $Cr^{3+} + h \longrightarrow Cr^{4+}$. The two processes occurring simultaneously lead to the establishment of a balance in the concentration of Cr^{3+} ions. This balance can be violated if the concentration of tetravalent chromium ions in the crystal exceeds that of the trivalent ions. In this case, the emission from Cr^{3+} will increase, as is the case in GSAG(Ca^{2+},Cr^{3+}) samples (Fig. 2). On the contrary, if the concentration of Cr^{3+} ions in the crystal exceeds that of the photoinduced Cr^{4+} ions, the emission from Cr^{3+} will decrease, as in GSGG(Cr^{3+},Nd^{3+}) samples (Fig. 2). During the repeated laser action, the balance in enhanced emission from Cr^{3+} is observed already upon a 20-min exposure. This behavior is violated if the sample is exposed to coherent second harmonic radiation of the YAG-Nd laser at a low temperature (77 K). Therefore, an electron under these conditions passes to an excited ion level via the conduction band, rather than exhibiting tunneling from an electron trap to an excited level of Cr^{4+} (otherwise the process would be temperature-independent). An analysis of the curves of the efficacy of the Cr^{3+} PL intensity enhancement at various temperatures allowed us to estimate the thermal energy as $kT = 0.011$ eV. Taking into account the quadratic dependence of the efficacy of the Cr^{3+} PL intensity enhancement on the average laser power, we also estimate the depth of electron traps relative to the valence band bottom as 4.671 eV.

REFERENCES

1. Chen Xiao-Bo, Wang Ling, Lü Lan-Bin, *et al.*, Chin. Phys. **12**, 1246 (2003).
2. L. I. Krutova, N. A. Kulagin, V. A. Sandulenko, *et al.*, Fiz. Tverd. Tela (Leningrad) **31** (7), 170 (1989) [Sov. Phys. Solid State **31**, 1193 (1989)].
3. V. I. Garmash, V. A. Zhitnyuk, A. G. Okhrimchuk, *et al.*, Izv. Akad. Nauk SSSR, Neorg. Mater. **26**, 1700 (1990).
4. l. G. Popov, Candidate's Dissertation (Irkutsk, 1994).
5. J. A. Caird, E. F. Krupke, M. D. Shinn, *et al.*, in *Proceedings of the Conference on Lasers and Electro-Optics, Optical Society of America, Baltimore, 1985*, p. 232.
6. N. N. Il'ichev, A. V. Kir'yanov, P. P. Pashinin, and S. H. Shpuga, Zh. Éksp. Teor. Fiz. **105**, 1426 (1994) [JETP **78**, 768 (1994)].
7. M. N. Demchuk, V. P. Mikhailov, *et al.*, Zh. Prikl. Spektrosk. **47**, 669 (1987).

Translated by P. Pozdeev

Luminescence of Crystals under the Action of a Subnanosecond Electron Beam

E. I. Lipatov*, V. F. Tarasenko, V. M. Orlovskiĭ, S. B. Alekseev, and D. V. Rybka

Institute of High-Current Electronics, Siberian Division, Russian Academy of Sciences, Tomsk, Russia
* e-mail: lipatov@loi.hcei.tsc.ru
Received October 25, 2004

Abstract—Subnanosecond avalanche electron beams formed in air at atmospheric pressure ensure intense luminescence of synthetic ruby and natural spodumene crystals. © *2005 Pleiades Publishing, Inc.*

Introduction. Investigation of the luminescence of crystals caused by various external factors is an important stage in the spectral analysis of solids, which allows the chemical composition and structure (including the presence of defects and internal stresses) to be determined [1]. Measuring the emission induced by electron beams (cathodoluminescence, CL), it is possible to perform the room-temperature spectral analysis of almost all nonmetallic solids. However, the classical CL measurements require placing the sample in vacuum and ensuring leakage of the electron-beam-induced current from the sample surface [2], which complicates the experimental procedure.

It was demonstrated [2–5] that, using high-current pulsed electron beams of nanosecond duration for the excitation of CL pulses, it is possible to perform the investigations in air at atmospheric pressure. The CL spectra measured under such conditions, as well as the PL spectra measured at cryogenic temperatures, are characterized by high resolution and reveal the fine structure [4]. However, along with this advantage, the pulsed CL technique has a significant drawback, since accelerated electron beams were obtained using vacuum diodes requiring continuous pumping, while sealed-off electron tubes had a short working life. This circumstance limited the implementation of pulsed CL techniques for rapid diagnostics of solid samples.

Recently [6–9], we have developed a new method for the formation of subnanosecond avalanche electron beams [7] in gas-filled diodes, where the beam current amplitude can reach tens and hundreds of amperes. The diodes can be filled by various gases, including air at atmospheric pressure. Thus, it is now possible to obtain high-density electron beams in the same gaseous medium where the crystal sample is situated.

This study was aimed at assessing the possibility of using subnanosecond avalanche electron beams in air at atmospheric pressure for the measurement of luminescence spectra of solids. In our experiments, pulsed CL was excited by such beams in synthetic ruby and natural spodumene crystals.

Experimental. The pulsed CL in crystal samples was excited using a small-size setup of the NORA type [10], in which the X-ray source was replaced by a gas-filled diode. The diode design was described previously [8]. In these experiments, the diode was filled with air from the surrounding atmosphere. The electron beam was extracted via a foil or a grid. Using this accelerator, it was possible to obtain pulsed electron beams with a duration (full width at half maximum, FWHM) of 0.2 ns at a pulse repetition rate of ~3 Hz. A beam current density at the diode output for a 40-μm-thick aluminum–beryllium foil was ~40 A/cm^2 [9]. Figure 1 shows the typical electron energy distribution measured at a distance of 5 cm from the foil. The maximum of this curve corresponds to an electron energy of ~80 keV.

The samples were synthetic ruby (α-Al$_2$O$_3$ containing Cr^{3+} impurity ions) and natural spodumene (LiAlSi$_2$O$_6$ with Mn^{2+} and Cr^{3+} ions). The ruby crystal of pink color had the shape of a long rod (160 mm long, with a diameter of 8 mm). The light gray spodumene
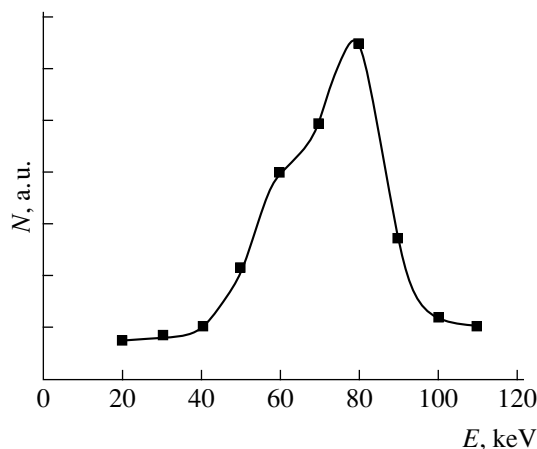

Fig. 1. Electron energy distribution measured at a distance of 5 cm from an output foil of the gas-filled diode of a NORA electron accelerator.

(a)

660   680   700   720   740 nm

(b)

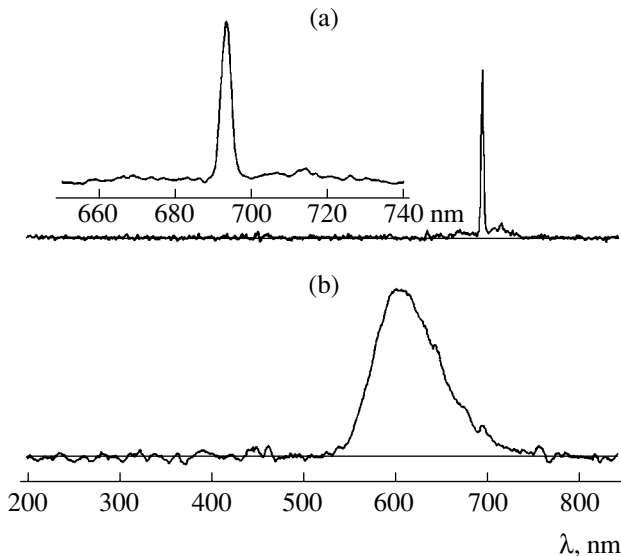200   300   400   500   600   700   800

λ, nm

Fig. 2. The spectra of pulsed CL of (a) synthetic ruby and (b) natural spodumene crystals excited using a NORA electron accelerator. The inset in (a) shows the wavelength interval from 650 to 740 nm on an expanded scale.

crystal had an irregular shape with dimensions $60 \times 20 \times 10$ mm; one edge of this crystal was polished.

The sample was placed at a distance of 5 cm from the diode output foil. The CL measurements were performed in air under normal conditions. The emission pulse was transmitted via an optical fiber to an EPP-2000C (StellarNet Inc.) spectrograph linked with a computer. This setup allowed the emission spectra to be measured in a wavelength range from 200 to 850 nm at a spectral resolution of 1.5 nm. Each CL spectrum was obtained by accumulating 100 emission pulses. The spectra were corrected by subtracting the dark component and taking into account the spectral sensitivity of the spectrograph and the fiber transmission function. The CL spectra were well reproduced in sequential experiments (10 independent runs).

Results and discussion. Figure 2 shows the spectra of pulsed CL measured for the synthetic ruby (a) and natural spodumene (b). The spectrum of ruby displays a narrow band peaked at 693 nm with FWHM = 3.5 nm. This band consists of overlapping *R* lines of emission from chromium ions [2–5]. In addition, there is a broad plateau extending from 655 to 735 nm with a relative intensity not exceeding 10% of the main peak height. This plateau can be assigned to weakly overlapping *N* and *S* lines of chromium [2, 4, 5]. The emission from the ruby crystal has visually appeared as red.

The spectrum of pulsed CL from the spodumene crystal had the shape of a broad band ranging from 520 to 760 nm with a peak at 600–608 nm and WFHM = 80 nm. This band is due to Mn^{2+} ions present as an impurity in the natural spodumene [2, 5]. The long-wave wing of this band exhibits a weak feature at 693 nm, which is probably related to Cr^{3+} ions (also

present as an impurity in the natural crystal). In order to reliably observe the emission from chromium ions, it is necessary to cool the sample below 100 K [11]. The pulsed emission from the spodumene crystal has visually appeared as having the orange color.

Conclusions. We have demonstrated for the first time that it is possible to use subnanosecond avalanche electron beams for studying the structure of nonmetallic solids in air under normal conditions. The CL spectra of synthetic ruby and natural spodumene crystals excited with a subnanosecond electron beam were obtained by accumulating 100 output emission pulses.

It should be noted that the pulsed CL spectra obtained for both synthetic ruby and natural spodumene crystals excited by subnanosecond pulses are practically the same as the analogous spectra obtained using pulsed electron beams of nanosecond duration [2, 5].

Subnanosecond electron beams can find use for the rapid analysis of luminescence spectra of various natural and synthetic materials. The short duration of the probing pulses may allow additional information to be obtained in the case of insulating and semiconducting substances.

REFERENCES

1. A. S. Marfunin, *Spectroscopy, Luminescence and Radiation Centers in Minerals* (Nedra, Moscow, 1975; Springer-Verlag, Berlin, 1979).

2. V. I. Solomonov, Doctoral Dissertation (Institute of Electrophysics, Ural Division, Russian Academy of Sciences, Yekaterinburg, 1996).

3. S. G. Mikhaĭlov, V. V. Osipov, and V. I. Solomonov, Zh. Tekh. Fiz. **63** (2), 52 (1993) [Tech. Phys. **38**, 85 (1993)].

4. G. A. Mesyats, V. I. Solomonov, S. G. Mikhaĭlov, and V. V. Osipov, Dokl. Akad. Nauk **339**, 757 (1994) [Phys. Dokl. **39**, 862 (1994)].

5. V. I. Solomonov, S. G. Mikhaĭlov, and A. M. Deĭkun, Opt. Spektrosk. **80**, 447 (1996) [Opt. Spectrosc. **80**, 398 (1996)].

6. S. B. Alekseev, V. M. Orlovskiĭ, and V. F. Tarasenko, Pis'ma Zh. Tekh. Fiz. **29** (10), 29 (2003) [Tech. Phys. Lett. **29**, 679 (2003)].

7. V. F. Tarasenko, V. M. Orlovskiĭ, and S. A. Shunaĭlov, Izv. Vyssh. Uchebn. Zaved., Fiz., No. 3, 94 (2003) [Russ. Phys. J. **46**, 325 (2003)].

8. V. F. Tarasenko, V. G. Shpak, S. A. Shunaĭlov, *et al.*, Pis'ma Zh. Tekh. Fiz. **29** (21), 1 (2003) [Tech. Phys. Lett. **29**, 879 (2003)].

9. S. B. Alekseev, V. P. Gubanov, V. M. Orlovskiĭ, and V. F. Tarasenko, Pis'ma Zh. Tekh. Fiz. **30** (20), 35 (2004) [Tech. Phys. Lett. **30**, 859 (2004)].

10. G. A. Mesyats, *Pulsed Power Engineering and Electronics* (Nauka, Moscow, 2004) [in Russian].

11. G. Walker, A. El Jaer, R. Sherlock, *et al.*, J. Lumin. **72–74**, 278 (1997).

Translated by P. Pozdeev

Hydrogen Sorption by Carbon-Based Substances Formed in Carbon–Helium Plasma

G. N. Churilov*, E. M. Kostinevich, S. A. Marchenko, G. A. Glushchenko, N. V. Bulina, A. I. Zaĭtsev, and N. G. Vnukova

Kirensky Institute of Physics, Siberian Division, Russian Academy of Sciences, Krasnoyarsk, Russia
* e-mail: churilov@iph.krasn.ru
Received September 17, 2004

Abstract—Hydrogen sorption by various carbonaceous products formed during arc discharge in carbon–helium plasma has been studied. The main product fractions included a fullerene-containing soot, a fullerene mixture extract, a condensate containing carbon nanotubes, and carbonized aluminum oxide. Molecular hydrogen is most effectively sorbed by single-wall carbon nanotubes contained in the carbon condensate fraction. © 2005 Pleiades Publishing, Inc.

Economic and technological development, with due allowance of ecological safety, require the search for and implementation of new energy sources. Considerable attention in this respect is devoted to the development of hydrogen power engineering, where the key problems are related to the safe storage and transport of hydrogen. It is believed that the most promising solutions are offered by carbon-based sorbents [1]. Unfortunately, published data on sorption efficiency, even for the same substance, are frequently contradictory [2, 3]: the relative amount of hydrogen per unit weight of sorbent may range from a fraction of a percent to tens of percent. The discrepancies may be related to differences in the structure of objects studied by various researchers.

This Letter reports the results of the investigation of hydrogen sorption by various carbonaceous products formed during arc discharge in carbon–helium plasma. The main product fractions were as follows: (F) a fullerene mixture containing 60% C_{60}, 25% C_{70}, and 15% of higher fullerenes; (T) a condensate including 15–20% of multiwall carbon nanotubes (MWNTs) of 120- to 160-nm diameter and turbostratic graphite [4] (with interplanar spacing in both MWNTs and graphite being 0.342 nm); (S_1) a fullerene-containing soot including about 9% fullerenes and more than 40% of single-wall carbon nanotubes (SWNTs); (S_2) a fullerene-containing soot including about 8% of fullerenes and 15% of carbon nanotubes; and (A) carbonized aluminum oxide (Al_2O_3 containing about 2 wt % of carbon) with a particle size of 5–40 μm and a specific surface of 119 m^2/g [5].

The samples of S_1, F, T, and A fractions were synthesized in a flow of carbon–helium plasma at atmospheric pressure in a setup described in detail elsewhere [6]. The discharge was operating between an external (cylinder) and an internal (rod) graphite electrodes. The sample of fraction S_1 was taken from a liquid-nitrogen trap purifying the gas flow at the output of the chamber in the course of synthesis. Fraction T was collected on the external electrode, where a carbonaceous deposit was formed in the course of synthesis. Fraction F was obtained by extraction with benzene from sample S_1. Fraction A was collected upon the introduction of Al_2O_3 particles into the flow of carbon–helium plasma. The sample of fraction S_2 was obtained in a setup for the fullerene synthesis according to the Kratschmer method [7].

The experiments on hydrogen sorption in the samples of carbonaceous products described above were performed as follows. Each sample was heated to 600°C in a vacuum of 10^{-4} Torr created by roughing (mechanical) and oil-diffusion pumps via a liquid-nitrogen trap. Then, the pumping stage was disconnected and the chamber was filled by hydrogen at a pressure of 100 bar. The hydrogen pressure was maintained constant while the sample was cooled to −180°C and kept under these conditions for 20 min. In order to desorb the stored hydrogen, the sample was gradually heated to 800°C. The amount of liberated hydrogen was measured under normal conditions with the aid of a U-shaped manometer.

The temperature dependence of the mass of hydrogen desorbed from various samples is presented in the figure. As can be seen, the amount of liberated hydrogen in all cases increased with the sample temperature. The maximum yield was observed for the samples of fraction S_1. A relatively small degree of hydrogenation observed for Al_2O_3 can be explained by the process of aluminum reduction competing with the sorption process. Thermogravimetric analysis of the samples of fraction S_2 in the initial state and upon hydrogen sorption showed that heat evolution in the hydrogenated
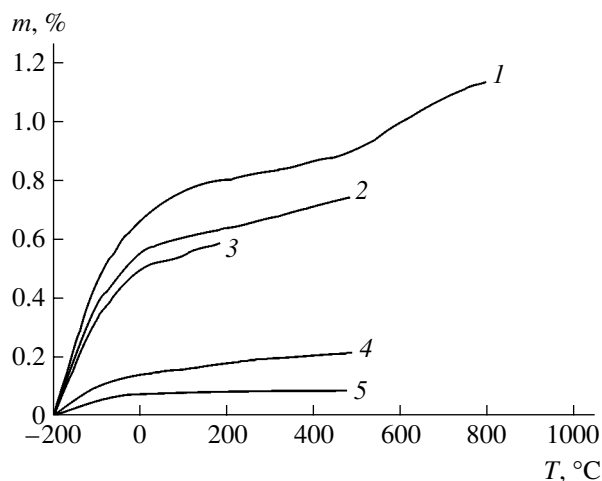
The temperature dependence of the relative mass of hydrogen (percentage of the sorbent weight) desorbed from various samples: (*1*) S_2; (*2*) S_1; (*3*) T; (*4*) F; (*5*) A.

sample is higher than in the initial state and agrees with the amount of sorbed hydrogen.

Thus, the results of our investigation showed that the most effective sorption of molecular hydrogen takes place by a fraction containing single-wall carbon nanotubes.

REFERENCES

1. Yu. S. Nechaev and O. K. Alekseeva, in *Proceedings of the 8th International Conference on Hydrogen Materials Science and Chemistry of Carbon Based Nanomaterials, Sudak, 2003*, pp. 776–780.

2. I. O. Bashkin, V. E. Antonov, A. V. Bazhenov, *et al.*, in *Proceedings of the 8th International Conference on Hydrogen Materials Science and Chemistry of Carbon Based Nanomaterials, Sudak, 2003*, pp. 798–799.

3. A. V. Eletskii and A. F. Pal, in *Proceedings of the 1st International Symposium on Carbon for Catalysis, Lausanne, 2004*, pp. 179–180.

4. G. N. Churilov, L. A. Solovyov, Y. N. Churilova, *et al.*, Carbon **37**, 427 (1999).

5. G. N. Churilov, E. A. Petrakovskaya, and N. V. Bulina, in *Proceedings of the 1st International Symposium on Carbon for Catalysis, Lausanne, 2004*, pp. 181–182.

6. G. N. Churilov, Prib. Tekh. Éksp., No. 1, 5 (2000).

7. W. Kratschmer, L. D. Lamb, K. Fostiropoulos, *et al.*, Nature **347**, 354 (1990).

Translated by P. Pozdeev

Midinfrared Injection-Pumped Laser Based on a III–V/II–VI Hybrid Heterostructure with Submonolayer InSb Insets

V. A. Solov'ev*, I. V. Sedova, O. G. Lyublinskaya, A. N. Semenov, B. Ya. Mel'tser, S. V. Sorokin, Ya. V. Terent'ev, and S. V. Ivanov

Ioffe Physicotechnical Institute, Russian Academy of Sciences, St. Petersburg, 194021 Russia
* e-mail: vasol@beam.ioffe.rssi.ru
Received November 11, 2004

Abstract—Lasing at 3.075 μm ($T = 60$ K) in a regime of pulsed injection pumping has been obtained in an AlGaAsSb/InAs/CdMgSe double hybrid heterostructure with the active region comprising an InAs layer with submonolayer InSb insets. The electroluminescence (EL) spectrum of the heterostructure has been studied for various values of the pumping current up to the stimulated emission threshold. An increase in the pumping current leads to a short-wavelength shift and a change in the EL band structure, which is explained by the occupation of higher states by the charge carriers in InSb quantum dots and/or in the adjacent InAsSb layer. © 2005 Pleiades Publishing, Inc.

In the past decade, considerable effort was devoted to the creation of injection-pumped lasers operating in the mid-IR range (3–5 μm). Such lasers are in demand for a broad spectrum of commercial applications, including chemical monitoring of atmospheric exhausts, contactless probing in medicine, IR spectroscopy, leak detection, laser surgery, etc. [1]. However, the maximum working temperature of existing lasers based on $A^{III}B^V$ semiconductor compounds under cw operation conditions is significantly below room temperature. This is mostly related to a considerable leak of the hole injection current via a *p–n* junction because of insufficiently high barriers bounding the active region of lasers based on such narrow-bandgap $A^{III}B^V$ semiconductors.

Recently, we have developed a new approach to the creation of mid-IR lasers [2, 3], which is based on the use of pseudomorphous AlGaAsSb/InAs/CdMgSe hybrid heterostructures grown on InAs substrates. These structures contain an $A^{III}B^V/A^{II}B^{VI}$ heterovalent junction at one boundary of the InAs active region. A significant (~1.5 eV) discontinuity of the valence band at the InAs/CdMgSe interface blocks the holes in InAs, thus preventing the carriers from leaking out of the active region. Despite the presence of a rather high density of defects (~10^6–10^7 cm^{-2}) at the CdMgSe/InAs interface and the use of a "bulk" InAs as the active region, such hybrid structures grown by molecular beam epitaxy (MBE) on InAs substrates allowed us to obtain lasing at ~2.78 μm (100 K) in the regime of pulsed injection pumping at a threshold current density $I_{th} \sim 3$–4 kA/cm^2 [4, 5]. Another important advantage of the proposed hybrid structures is their practically ideal

optical confinement in the InAs active region, which is related to a large difference between the refractive indices of InAs and CdMgSe ($n_{IsAs} = 3.5$, $n_{CdSe} = 2.55$). Thus, the hybrid structures offer a unique combination of properties that cannot be obtained using only $A^{III}B^V$ compounds.

In order to obtain lasing at even longer wavelengths, reduce the Auger recombination losses, and decrease the threshold current density, we suggest to employ the active laser region in the form of an InAs layer containing submonolayer InSb insets, which would provide an effective channel of radiative recombination of charge carriers. Such structures were grown by MBE and, despite the fact that InSb/InAs interfaces belong to type II heterojunctions, they exhibited intense photoluminescence (PL) within 3.4–4.3 μm in a broad temperature range (77–300 K) [6]. The formation of InSb layers was due to the substitution of antimony atoms for arsenic on the InAs surface exposed to a flow of antimony. The nominal thickness of InSb increased from 0.6 to 1 monolayer (ML) when the substrate temperature was decreased from 485 to 400°C. Investigation of the obtained submonolayer InSb deposits by transmission electron microscopy showed that these insets contain quantum-dimensional islands enriched with InSb. The lateral size of islands was 2.5 ± 1.5 nm and their surface density exceeded 10^{12} cm^{-2} [7].

In this Letter, we report on the obtaining of stimulated emission at ~3.075 μm ($T = 60$ K) in a regime of pulsed injection pumping in AlGaAsSb/InAs/CdMgSe double hybrid heterostructures with the active region comprising an InAs layer with submonolayer InSb insets.
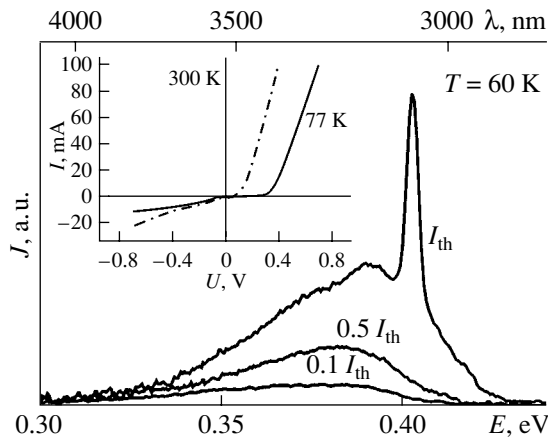
Fig. 1. The low-temperature EL spectra of the hybrid laser diode structure measured for various values of the pumping current density. The inset shows the *I–U* characteristics measured at 77 and 300 K.
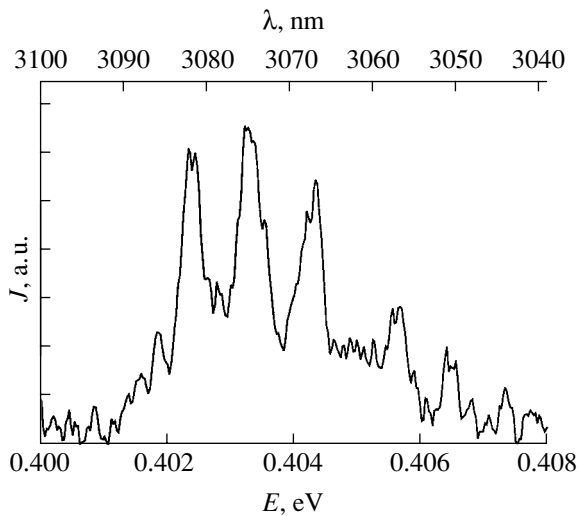

Fig. 2. The coherent emission spectrum of the laser heterostructure in the pulsed injection pumping regime.

The laser heterostructure was grown on a p^+-InAs(001) substrate by sequential MBE in two separate setups. In contrast to the previously described heterostructures without InSb insets (referred to below as the "reference" structures) [4], the lower p-emitter was a 2.5-μm-thick $Al_{0.8}Ga_{0.2}As_{0.15}Sb_{0.85}$:Be layer with increased aluminum content, while the waveguide was provided by an 0.6-μm-thick InAs layer containing a three-period structure comprising ultra-thin (submonolayer) InSb insets and 20-nm-thick InAs barriers. The region including InSb insets and a part of the waveguide was formed at 450°C, and all the other layers were grown at 500°C. The nominal thickness of InSb insets was 0.8 ML. The composition and growth features of the $A^{II}B^{VI}$ part of the structure were generally the same as in the reference structure (for details, see [4, 5]). However, in order to protect the InAs sur-

face during the sample transfer to the $A^{II}B^{VI}$ growth chamber, the sample was chemically passivated in an aqueous Na_2S solution [8] (instead of the previously used deposition of a polycrystalline arsenic layer). It was established that this chemical treatment followed by annealing at 500°C in a flow of arsenic ensures the formation of an atomically smooth (2×4)As-stabilized InAs surface, offering the ideal substrate for the subsequent coherent growth of $A^{II}B^{VI}$ compounds. The electroluminescence (EL) spectra and lasing properties of the structures were studied using four-side cleaved samples.

The current–voltage (*I–U*) curves of the laser heterostructures (see the inset to Fig. 1) have the shape characteristic of a diode with a forward branch cutoff voltage of 0.37 and 0.16 V at $T = 77$ and 300 K, respectively. Apparently, the cutoff voltage is determined by the bandgap of InAs. This indicates that the space charge region of the $p–n$ junction is situated completely inside the InAs waveguide layer.

Figure 1 shows the low-temperature EL spectra of the laser heterostructures measured at various levels of pumping up to the stimulated emission threshold (I_{th}). At a low pumping current, the EL spectrum displays a broad double band. The long-wavelength part generally resembles the PL spectrum with an emission maximum at ~0.35 eV observed for an undoped test structure with InSb insets formed at 450°C. The short-wavelength emission with a maximum near 0.38 eV dominates in the EL spectrum and exhibits a rather significant "blue" shift with an increase in the pumping current. We believe that this short-wavelength shift and a change in the EL band structure with increasing pumping current are explained by the occupation of higher energy states by the charge carriers in InSb quantum dots (QDs) and, probably, in the adjacent ultra-thin InAsSb layer. An analogous behavior of the EL spectrum was observed in laser heterostructures based on QDs of type I [9]. In the case of QDs of type II, the saturation of states with lower energies can be even more pronounced due to an increase in the time of radiative recombination.

The lasing observed at a wavelength of $\lambda \sim 3.075$ μm was determined by the optical transitions involving excited states in the QDs or in the adjacent wetting InAsSb layer. Figure 2 shows the laser spectrum observed in the regime of pulsed injection pumping (pulse width, 200 ns; repetition rate, 3.2 kHz). The average mode separation was 7.5 nm and the main laser peak width (not exceeding 4 nm) was determined by the transmission function of the detection system. It should be noted that the shift of the laser wavelength beyond 3 μm was not accompanied by an increase in the threshold current density, which remained the same as in the reference structure (3–4 kA/cm²).

Thus, using a p-AlGaAsSb/InAs/n-CdMgSe double hybrid heterostructure with the active region comprising InSb/InAs quantum dots of type II (rather than the "bulk" InAs layer), it is possible to shift the laser wave-

length from 2.78 to 3.075 μm (at low temperature) without a change in the threshold current density. It is expected that, if QD arrays of greater size, the structures with multiple QD layers and vertical QD ordering, and optimized base hybrid laser structures are used, it will be possible to reach longer emission wavelengths, reduce the threshold current density, and, probably, obtain lasing at room temperature.

REFERENCES

1. J. Wagner, Ch. Mann, M. Rattunde, and G. Weimann, Appl. Phys. A **78**, 505 (2004).

2. V. A. Solov'ev, I. V. Sedova, A. A. Toropov, *et al.*, Fiz. Tekh. Poluprovodn. (St. Petersburg) **35**, 431 (2001) [Semiconductors **35**, 419 (2001)].

3. S. V. Ivanov, V. A. Solov'ev, K. D. Moiseev, *et al.*, Appl. Phys. Lett. **78**, 1655 (2001).

4. S. V. Ivanov, K. D. Moiseev, V. A. Kaĭgorodov, *et al.*, Fiz. Tekh. Poluprovodn. (St. Petersburg) **37**, 762 (2003) [Semiconductors **37**, 736 (2003)].

5. S. V. Ivanov, V. A. Kaygorodov, S. V. Sorokin, *et al.*, Appl. Phys. Lett. **82**, 3782 (2003).

6. A. N. Semenov, V. A. Solov'ev, Ya. V. Terent'ev, *et al.*, in *Proceedings of the 6th All-Russia Conference on Physics of Semiconductors, St. Petersburg, 2003*, p. 322.

7. A. N. Semenov, V. A. Solov'ev, O. G. Lyublinskaya, *et al.*, in *Proceedings of the 6th International Conference on Mid-Infrared Optoelectronic Materials and Devices, St. Petersburg, 2004*, p. 147.

8. S. V. Ivanov, O. G. Lyublinskaya, Yu. B. Vasilyev, *et al.*, Appl. Phys. Lett. **84**, 4777 (2004).

9. D. Bimberg, M. Grundmann, and N. Ledentsov, *Quantum Dot Heterostructures* (Wiley, Chichester, 1999), p. 279.

Translated by P. Pozdeev

High-Efficiency LEDs Based on GaInAsSb Solid Solutions with Reduced Arsenic Content in the Active Region

B. E. Zhurtanov, T. N. Danilova, A. N. Imenkov, M. A. Sipovskaya, and Yu. P. Yakovlev

Ioffe Physicotechnical Institute, Russian Academy of Sciences, St. Petersburg, 194021 Russia

Received November 22, 2004

Abstract—Light-emitting diodes (LEDs) with the active region based on $Ga_{1-x}In_xAs_ySb_{1-y}$ solid solutions are obtained on GaSb substrates. The active region has a composition close to the domain of immiscibility ($x = 0.24$) and a reduced arsenic content ($y = 0.16$). The diode structures exhibit a high density of misfit dislocations. Nevertheless, the room-temperature external quantum yield reaches a record-high level of 1.2% in the spectral band with a maximum wavelength of 2.42 μm. The maximum output radiation pulse power reaches 3.3 mW at a current of 600 mA. The emission is predominantly due to the interband transitions, which is evidence of a high degree of stoichiometry of the active region. © *2005 Pleiades Publishing, Inc.*

Introduction. As is known, solid solutions of the $Ga_{1-x}In_xAs_ySb_{1-y}$ system are isoperiodic with GaSb ($y = 0.91x$) and exhibit immiscibility in the interval of actual x values from 0.25 to 0.75 [1–3]. A decrease in the content of arsenic (As) must lead to narrowing of the domain of immiscibility because the composition approaches $Ga_{1-z}In_zSb$ (this system has no immiscibility domain [1–3]). One may expect that, in this way, it is possible to use liquid phase epitaxy (LPE) for the growth of solid solutions with previously unreported bandgap widths (0.24–0.48 eV) corresponding to the immiscibility domain. It is important to note that a decrease in the content of As is also accompanied by increasing spin-orbit splitting of the valence band, which becomes greater than the bandgap width. As a result, the nonradiative CHHS Auger recombination process (whereby one hole passes to the conduction band and the other to a spin-split subband of the valence band) has a low probability and the internal quantum yield must increase.

However, a growth in the content of As is accompanied by an increase in the lattice parameter, which leads to the development of compressive mechanical stresses in the growing layer (while the bandgap width is practically independent of the As content). The lower the As content, the stronger the compression. This may result in the appearance of defects related to the lattice mismatch between the growing layer and the GaSb substrate. The properties of layers grown under such conditions have not yet been investigated. It is expected that the development of a method for growing $Ga_{1-x}In_xAs_ySb_{1-y}$ layers with a reduced As content on GaSb substrates, together with the method of epitaxy from lead-containing solution melts [4], will make possible the synthesis of compounds with compositions corresponding to the domain of immiscibility. Such epilayers are expected to exhibit highly effective electroluminescence (EL).

The aim of this study was to obtain LED structures with an active region having the $Ga_{1-x}In_xAs_ySb_{1-y}$ composition with $x = 0.24$ and a reduced content of As ($y < 0.91x$) as compared to the isoperiodic composition near the boundary of the immiscibility domain. Such structures were grown by LPE and characterized with respect to EL properties.

Methods of growth and investigation of LED structures. The LED structures (Fig. 1) were grown by LPE on 350-μm-thick *n*-type GaSb single crystal substrates with (111)*B* orientation. The substrates were doped with tellurium (Te) so that the electron density was $n = 8 \times 10^{17}$ cm⁻³. The active layer of a $Ga_{1-x}In_xAs_ySb_{1-y}$ solid solution with $x = 0.24$ and a thickness of 1.3 μm (Fig 1a, layer *1*) was grown in the cooling regime from a solution melt containing atoms of the solid solution components (Ga, In, Sb, As) and the dopant (Te). The content of As was 25% below that required for the growth of a layer isoperiodic with GaSb. The content of Te corresponded to the electron density $n = 1 \times 10^{17}$ cm⁻³ in the growing layer. The measured mismatch between lattice parameters of the grown active layer and the GaSb substrate was 0.26%, which is lower than the expected value (0.36%). The emitter (Fig 1a, layer *2*) was formed by growing a 3.5-μm-thick layer of *p*-type GaSb doped with germanium (Ge) so as to obtain a hole density of $p = 1 \times 10^{18}$ cm⁻³. The contact *p*-GaSb layer had a thickness of 0.5 μm and was doped with Ge to $p = 8 \times 10^{18}$ cm⁻³ (Fig. 1a, layer *3*).

We have manufactured and studied two variants of the LED design. In variant 1, the wafer was cut into 350×350-μm chips and these chips were soldered to the standard TO-18 cases, so that the epilayer faced a

dip in the base (Fig. 1b). In variant 2, the 500×500-μm chips were soldered to the standard TO-18 cases so that the substrate was in contact with the flat base (Fig. 1c). In variant 1, an ohmic contact with a diameter of 150-μm was formed on the outer (substrate) surface; in variant 2, a 300-μm-diam mesa and a 100-μm-diam ohmic contact were formed on the outer surface.

The EL spectra and directivity diagrams of LEDs were measured at room temperature for various forward currents in the range from 50 to 600 mA. The LEDs were power supplied by 1-ms current pulses at an 0.5 duty factor for the currents below 100 mA and by 200-ns pulses at an 0.02 duty factor for the currents above 100 mA. The LEDs were fan-cooled in order to reduce heating. The EL spectra were measured using a monochromator (MDR-2) calibrated in units of radiation power per unit wavelength (mW/μm). The measurements were performed in the direction perpendicular to the active layer. The total radiation power was determined by integrating over the directivity diagram.

Results and discussion. The surface of $Ga_{1-x}In_xAs_ySb_{1-y}$ epilayers with reduced As content has an unusual appearance, exhibiting an array of depressions with a diameter of about 1 μm and a period of about 10 μm. This array is probably formed by misfit dislocations related to a lattice mismatch, whereby the lattice parameter of the epilayer is greater than that of the substrate. The threads of dislocations are probably capable of significantly reducing the compressive mechanical stresses, which is confirmed by the planar character of the pate surface.

The I–U curves of LEDs exhibit a diode character. The cutoff voltage in the forward direction was 0.3 V and the serial resistance was about 3 Ω for both variants of the LED design. The emission spectra can be considered as single-band, although there is a small step on the long-wavelength wing (Fig. 2). This step is very weak and can be attributed to doubly charged acceptors related to deviations from stoichiometry [5, 6]. The dominating spectral band can be interpreted as being due to interband transitions. For comparison, it can be pointed out that in GaSb (where the degree of non-stoichiometry is 1–2%) the radiation via doubly charged acceptors is dominant while the interband transitions are virtually not manifested [5, 6]. The small-ness of this step in the obtained spectra is evidence of a high stoichiometry of the active region. The wavelength at the EL maximum in variant 1 of the LED design for small currents (<100 mA) is 2.42 μm (which corresponds to a photon energy of $h\nu = 0.51$ eV), while in variant 2 it is 2.40 μm ($h\nu = 0.52$ eV). The bandgap width estimated from the emission spectrum is 0.49 eV. The emission band halfwidth (FWHM) is 0.21 μm (44 meV = $1.7kT$) in variant 1 and 0.26 μm (57 meV = $2.2kT$) in variant 2. The wavelength of the EL maximum decreases with an increase in the diode current, which is related to the growth of electron density. When the diode current increases from 50 to 600 mA, this
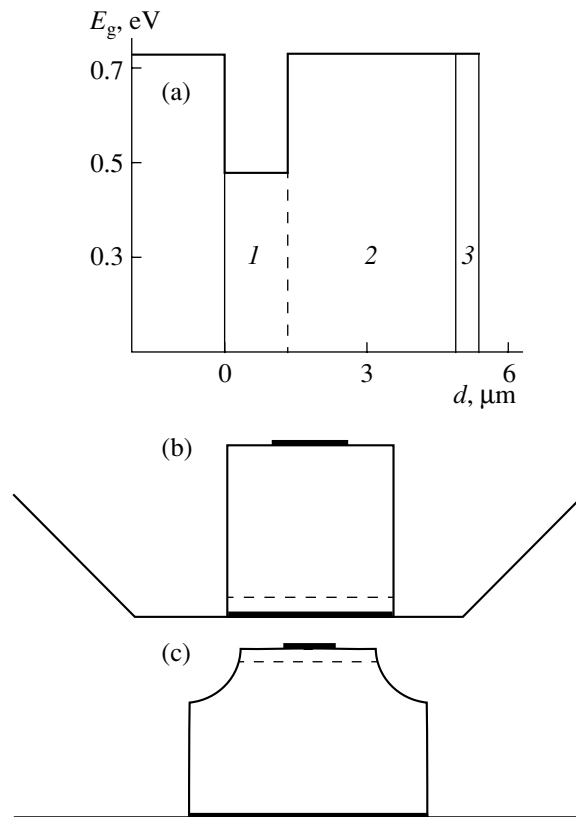

Fig. 1. LED structures based on a GaInAsSb solid solution with reduced As content: (a) energy band diagram of a heterostructure with (*1*) active region on GaSb substrate, (*2*) emitter, and (*3*) contact layer; (b) LEDs designed in variant 1 (epilayer is soldered to TO-18 case with a dip in base, LED 941 No. 1); (c) LED designed in variant 2 (substrate is soldered to TO-18 case with flat base, LED 941 No. 3-PM).
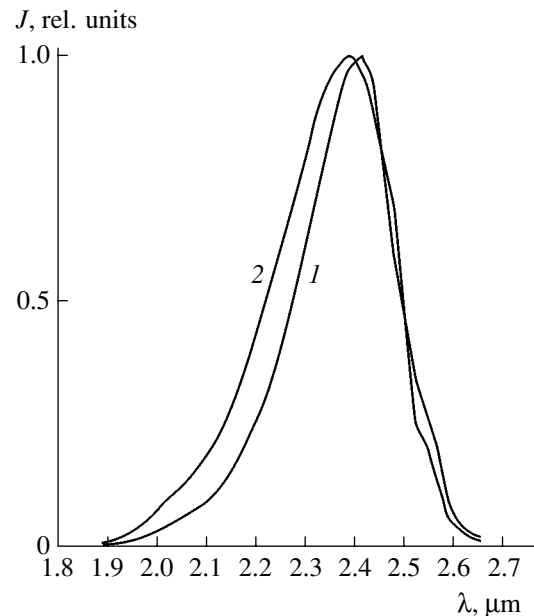

Fig. 2. Room-temperature EL spectra measured at a current of 50 mA for LEDs designed in variants 1 (curve *1*) and 2 (curve *2*).
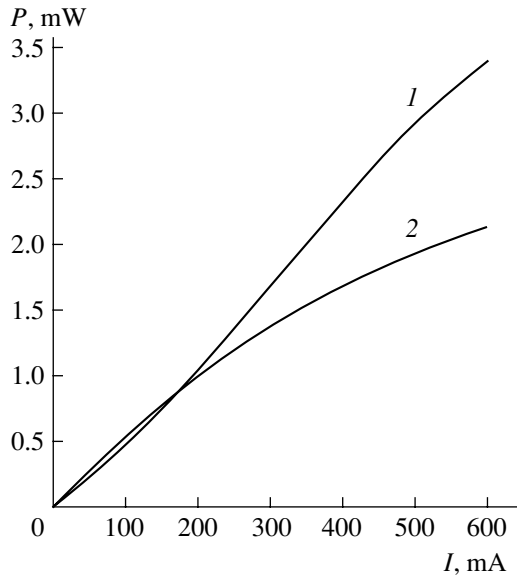
P, mW

Fig. 3. Plots of the output radiation pulse power versus current for LEDs designed in variants 1 (curve *1*) and 2 (curve *2*).

wavelength shift is 0.04 and 0.07 μm for variants 1 and 2, respectively. The width of the emission band increases to approximately the same extent. Thus, the emission spectra of LEDs only slightly differ for variants 1 and 2, in accordance with a difference in the current density.

The radiation directivity diagram for variant 1 can be considered as consisting of a cosine lobe, corresponding to the emission through the external crystal face, and a twice as narrow cosine lobe corresponding to the emission through side crystal faces and the reflection from the dip walls. The emission from variant 2 exhibited no preferred directions in the half-space, which is typical of deeply etched mesa structures [5].

The output radiation pulse power of LEDs designed in variant 1 almost linearly increases with the current (Fig. 3, curve *1*), with a slightly superlinear behavior for $I < 100$ mA and sublinear behavior for $I > 500$ mA. Variant 2 is characterized by a sublinear curve (Fig. 3, curve *2*), which is related to concentration of the injection current. This behavior was also observed in LEDs of this design operating at other wavelengths [5–7] in cases of poor current spreading over a thin *p*-type region. In the case of such concentration, the current density under the contact exhibits superlinear growth with the total current, which accounts for the corresponding increase in the level of superconductor excitation. For this reason, the wavelength at the maximum of radiation intensity is somewhat lower and decreases with the current somewhat more rapidly in variant 2 than in variant 1, where the areas of the *p*-type region and the ohmic contact are equal and the injection is more uniform. For the same reason, the spectral band width is greater in variant 2 than in variant 1.

An analysis of the shape of emission spectra shows that the density of nonequilibrium carriers in the recombination region of LEDs for variant 2 at a current of 600 mA is only about half of the density of equilibrium carriers. In variant 2, these densities are equal, which is indicative of a high excitation level. The high excitation level leads to an increase in the probability of the nonradiative CHCC Auger recombination process (whereby one hole passes from the conduction band to the valence band, and the liberated energy is transferred to another electron, which is retained in the conduction band), so the probability of the interband (radiative) recombination accordingly decreases.

The maximum differential quantum yield was 1.2% in both variants 1 and 2, but in variant 1 this maximum is achieved in a range of currents from 200 to 500 mA, while in variant 2 this yield takes place in the interval from 50 to 100 mA. The output radiation power in LEDs of variant 1 at 600 mA reaches 3.3 mW, which is 1.5 times the value in variant 2 and is also explained by more uniform injection over the entire area of the *p–n* junction. The maximum eternal quantum yield reached in this study is twice that reported for LEDs with a $Ga_{1-x}In_xAs_ySb_{1-y}$ active region (of the same thickness) isoperiodic with GaSb [8].

Apparently, a decrease in the content of As relative to a level necessary for the isoperiodic matching leads to a narrowing of the domain of immiscibility. Therefore, the composition of the active region falls out of this domain, which results in an increase in the crystallographic perfection and stoichiometry of the active region. The improved stoichiometry leads to a decrease in the concentration of doubly charged acceptors and in the intensity of radiation via this channel, while the interband radiation increases. The probability of the impact CHHS Auger recombination decreases because a decrease in the As content leads to increased spin-orbit splitting of the valence band. At the same time, the rate of the CHCC Auger process remains (to the first approximation) virtually unchanged. Improved stoichiometry also decreases the concentration of intrinsic doubly charged centers, which facilitates reaching a low density of the major charge carriers and a low rate of the CHCC Auger process. In the obtained LEDs, the major charge carriers are electrons. Their density is 30 times lower (1×10^{17} cm^{-3}), while the quantum yield of emission is about 10 times higher as compared to the values reported for 2.44 μm LEDs [4]. These trends indicate a possible way to further increase in the quantum yield of LEDs.

Conclusions. $Ga_{1-x}In_xAs_ySb_{1-y}$ based heterostructures for LEDs operating at 2.42 μm have been grown by LPE on GaSb substrates. The content of As in the active region with the composition $Ga_{0.76}In_{0.24}As_{0.16}Sb_{0.84}$ is 25% below that required for the growth of an epilayer isoperiodic with the substrate. The layer with reduced As content shows evidence of the formation of misfit dislocations related to a lattice mismatch between the

epilayer and the substrate. The obtained LEDs exhibit a record-high external quantum yield (1.2%) in the wavelength range 2.4–2.5 μm and have a maximum room-temperature output power of 3.3 mW. The external quantum yield is twice that obtained in analogous LEDs with an active region (of the same thickness) isoperiodic with the substrate. This result shows that the recombination via misfit dislocations is insignificant.

REFERENCES

1. O. Madelung, *Physics of III–V Compounds* (Wiley, New York, 1964).

2. P. I. Baranskiĭ, V. P. Klochkov, and I. V. Potykevich, *A Handbook on Semiconductor Electronics* (Naukova Dumka, Kiev, 1975) [in Russian].

3. I. Vurgaftman, J. R. Meyer, and L. R. Ram-Mohan, J. Appl. Phys. **89**, 5815 (2001).

4. A. P. Astakhova, E. A. Grebenshchikova, É. V. Ivanov, *et al.*, Fiz. Tekh. Poluprovodn. (St. Petersburg) **38**, 1466 (2004) [Semiconductors **38**, 1419 (2004)].

5. E. A. Grebenshchikova, A. N. Imenkov, B. E. Zhurtanov, *et al.,* Fiz. Tekh. Poluprovodn. (St. Petersburg) **37**, 1465 (2003) [Semiconductors **37**, 1414 (2003)].

6. E. A. Grebenshchikova, A. N. Imenkov, B. E. Zhurtanov, *et al.*, Fiz. Tekh. Poluprovodn. (St. Petersburg) **38**, 745 (2004) [Semiconductors **38**, 717 (2004)].

7. A. N. Imenkov, E. A. Grebenshchikova, B. E. Zhurtanov, *et al.*, Fiz. Tekh. Poluprovodn. (St. Petersburg) **38**, 1399 (2004) [Semiconductors **38**, 1356 (2004)].

8. A. A. Andaspaeva, A. N. Baranov, E. A. Grebenshchikova, *et al.*, Fiz. Tekh. Poluprovodn. (Leningrad) **23**, 373 (1989) [Sov. Phys. Semicond. **23**, 853 (1989)].

Translated by P. Pozdeev

Magnetoelastic Properties of an Amorphous Ferromagnetic Alloy Annealed by Electric Current

A. A. Gavrilyuk, A. L. Semenov, and A. Yu. Mokhovikov

Irkutsk State University, Irkutsk, Russia
e-mail: zubr@api.isu.ru
Received November 8, 2004

Abstract—The magnetoelastic wave propagation velocity and the magnetic-field-induced change in the elastic modulus (ΔE effect) have been studied as functions of the magnetic field strength in thin stripes of an amorphous ferromagnetic alloy ($Fe_{64}Co_{21}B_{15}$) annealed by direct electric current of variable density. It is shown that such treatment is an effective method for obtaining amorphous ferromagnetic alloy ribbons with uniaxial anisotropy and high magnetoelastic characteristics. © *2005 Pleiades Publishing, Inc.*

We have studied the effect of annealing by electric current on the magnetoelastic properties of a magnetostrictive amorphous ferromagnetic alloy of the $Fe_{64}Co_{21}B_{15}$ type obtained by rapid quenching of the melt and having a saturation magnetostriction of $\lambda_S \approx$ (25–30) $\times$ 10^{-6}. The aim of this treatment was (i) to relieve internal stresses developed in the course of rapid quenching and (ii) to induce a uniaxial anisotropy with the easy magnetization axis perpendicular to the length of the amorphous alloy ribbon.

The samples had the form of 3- to 6-cm-long stripes with a width of 1.0–1.2 mm and a thickness of 25 μm, which were cut from the amorphous alloy ribbons along the rolling direction. The samples were treated in air by passing a direct electric current along the stripes. The current density j was gradually increased from 2×10^7 to 7.3×10^7 A/m^2 at a step of 0.63×10^7 A/m^2. The time of current passage at each value j was 2 min.

Then, the magnetoelastic wave propagation velocity V_{me} and the magnetic-field-induced change in Young's modulus E (or ΔE effect) as functions of the applied magnetic field strength were measured using the resonance–antiresonance technique [1, 2]. A constant magnetic field H and a small variable magnetic field $h \approx$ 5 A/m (exciting magnetoelastic oscillations in the samples) were applied along the stripes.

Figure 1a shows the plots of V_{me} versus H for 5-cm-long samples annealed at various densities j of direct electric current. For small current densities ($j < 3.3 \times 10^7$ A/m^2), the V_{me} value exhibits a monotonic growth with H, which is evidence of the dominating process of domain wall displacement in the mechanism of magnetization moment rotation [3]. Therefore, no significant uniaxial anisotropy is induced in the samples annealed at $j < 3.3 \times 10^7$ A/m^2. As the current density is further increased in the interval from 3.3×10^7 to 6.7×10^7 A/m^2, the $V_{me}(H)$ curve exhibits a characteristic

minimum, with the minimum V_{me} value dependent on j. The appearance of a minimum on the $V_{me}(H)$ curves of magnetostrictive amorphous ferromagnetic alloys upon the treatment in this regime can be considered as evi-
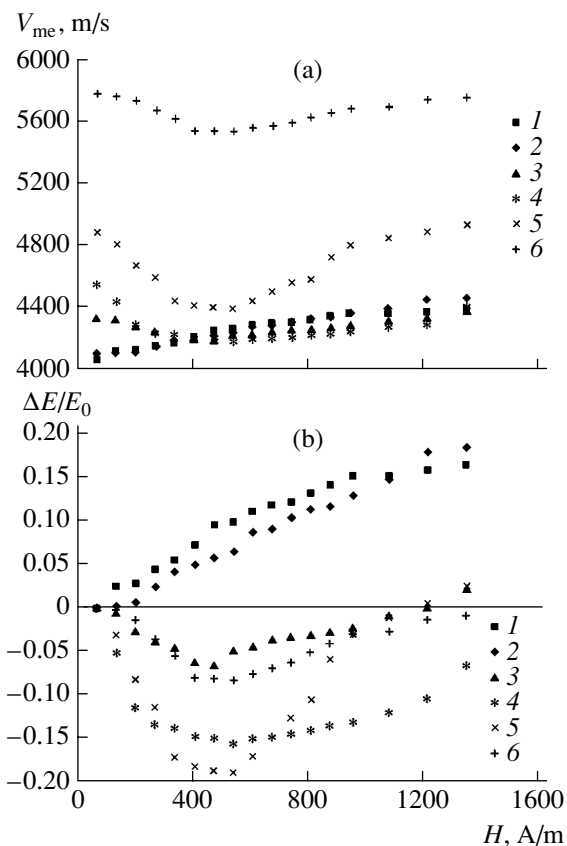

Fig. 1. Plots of (a) the magnetoelastic wave propagation velocity V_{me} and (b) the ΔE effect versus magnetic field strength H for the stripes of an amorphous ferromagnetic alloy annealed by direct electric current of various densities j (10^7 A/m^2): (*1*) 2; (*2*) 2.7; (*3*) 33; (*4*) 4.7; (*5*) 5.3; (*6*) 6.6.

dence of the induced uniaxial anisotropy with the easy axis perpendicular to the stripe length [2, 4]. The magnetic field H applied along the stripe rotates the magnetic moment to make it parallel to the field, which leads to a decrease in V_{me}. The subsequent increase in V_{me} in stronger magnetic fields is related to a change in the domain wall structure under the action of the applied field [2, 4]. The maximum relative change in the velocity of magnetoelastic wave propagation in a 5-cm-long stripe was observed for a sample annealed at $j = 5.3 \times 10^7$ A/m², in which case $|(V_{meH} - V_{me0})/V_{me0}|_{max} \approx 9.8\%$ (where V_{meH} and V_{me0} are the magnetoelastic wave velocities at $H \approx 600$ A/m and $H = 0$, respectively). As the current density is increased above $(5.3–6.0) \times 10^7$ A/m², the relative field-induced change in V_{me} decreases. This behavior of $V_{me}(H)$ upon the treatment at high current densities is explained by crystallization of the initially amorphous material, which leads to the growth in internal stresses and the breakage of the induced uniaxial anisotropy.

Figure 1b presents the plots of the ΔE effect versus H for 5-cm-long samples annealed at various densities j of direct electric current. The effect was defined as $\Delta E/E_0 = (E_H - E_0)/E_0$, where E_0 and E_H are Young's modulus measured in the absence of the magnetic field and upon application of the field H, respectively. For small current densities ($j < 3.3 \times 10^7$ A/m²), the ΔE effect is positive, whereby E_H increases with the magnetic field strength H. As the current density is increased in the interval from 3.3×10^7 to 7.3×10^7 A/m², the sign of the ΔE effect changes from positive to negative (E_H decreases with increasing H). The negative ΔE effect also evidences the existence of the induced uniaxial anisotropy with the easy axis perpendicular to the stripe length [5]. The positions of minima on the field dependences of V_{me} and $\Delta E/E_0$ are independent of the j value and correspond to $H \approx 470–540$ A/m. The maximum absolute value of the negative ΔE effect in a 5-cm-long stripe was observed upon the treatment at $j = 5.3 \times 10^7$ A/m², in which case $|\Delta E/E_0|_{max} \approx 0.20$. As the current density is further increased, the relative field-induced change in Young's modulus (negative ΔE effect) decreases, which can be also related to crystallization processes in the initially amorphous samples.

The electric current density j at which the negative ΔE effect appears in the stripes of various lengths was $(3.3–4) \times 10^7$ A/m². The maximum ΔE effect increased with decreasing sample length L (Fig. 2). On the other hand, the V_{me} value and the shape of the $V_{me}(H)$ curve exhibited no significant dependence on L and were entirely determined by j. These results can be explained as follows. The V_{me} value is related to Young's modulus E_H as follows:
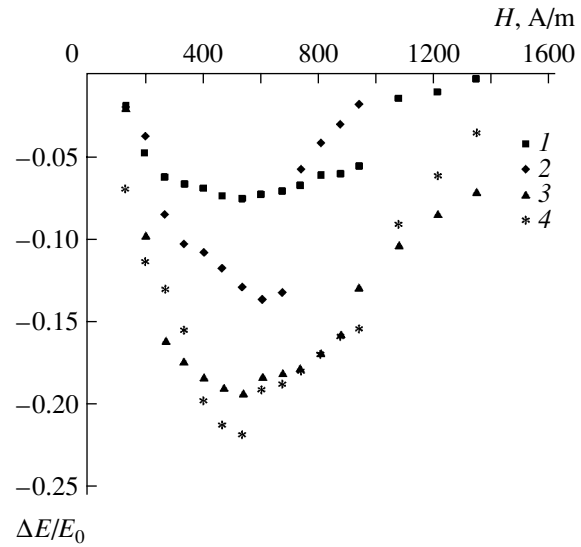
$$V_{me} = (E_H/\rho)^{1/2}, \qquad (1)$$

Fig. 2. Plots of the ΔE effect versus magnetic field strength H for the stripes of an amorphous ferromagnetic alloy of various lengths $L = 6$ (*1*), 5 (*2*), 4 (*3*), and 3 cm (*4*) annealed by direct electric current of the same density $j = 5.3 \times 10^7$ A/m².

where ρ is the sample density. If the magnetization proceeds by rotation of the magnetic moment toward the H direction, E_H can be expressed as [2]

$$E_H = E_0(2K - 3\lambda_S\sigma + NM_S^2\mu_0)^3/[(2K - 3\lambda_S\sigma + NM_S^2\mu_0)^3 + 9\lambda_S^2M_S^2H^2\mu_0^2E_0]. \qquad (2)$$

Here, M_S is the saturation magnetization, K is the parameter of induced uniaxial anisotropy, μ_0 is the magnetic permeability of vacuum, and N is the demagnetizing factor along the stripe. The latter quantity can be approximately expressed as [6]

$$N = (1/L)/[(1/L) + (1/a) + (1/b)], \qquad (3)$$

where a and b are the stripe width and thickness, respectively.

Then, the magnitude of the ΔE effect can be written as

$$\Delta E/E_0 = (9\lambda_S^2M_S^2H^2\mu_0^2E_0/[(2K - 3\lambda_S\sigma + NM_S^2\mu_0)^3 + 9\lambda_S^2M_S^2H^2\mu_0^2E_0]). \qquad (4)$$

According to expressions (1)–(4), the $\Delta E/E_0$ value depends much more strongly than V_{me} on N (and, hence, on L). A decrease in the absolute value of $\Delta E/E_0$ with increasing L also confirms that the magnetic moment rotation is the dominating mechanism of magnetization of the samples studied.

The results obtained in this investigation lead to the following conclusions:

(i) The passage of direct electric current in narrow thin stripes of magnetostrictive amorphous ferromagnetic alloys is an effective means of inducing uniaxial anisotropy in the material with the easy axis perpendicular to the current direction.

(ii) The electric current density at which the negative ΔE effect in magnetostrictive amorphous ferromagnetic alloys takes place is independent of the sample length.

(iii) The maximum absolute value of the negative ΔE effect in narrow stripes of a magnetostrictive amorphous ferromagnetic alloy annealed by the electric current increases with the sample length, while the magnetoelastic wave propagation velocity V_{me} and the shape of its dependence on the applied magnetic field are virtually independent of the sample length. This behavior can be explained within the framework of the model of homogeneous rotation of the magnetic moment in magnetostrictive amorphous ferromagnetic alloys with induced uniaxial anisotropy.

REFERENCES

1. H. T. Savage, A. E. Clark, and I. M. Powers, IEEE Trans. Magn. **11**, 1355 (1975).

2. A. A. Gavrilyuk, A. V. Gavrilyuk, and N. P. Kovaleva, Zh. Tekh. Fiz. **69** (6), 50 (1999) [Tech. Phys. **44**, 653 (1999)].

3. J. Gutierres, V. Muto, and P. T. Squire, J. Non-Cryst. Solids **287**, 417 (2001).

4. A. A. Gavrilyuk, N. P. Kovaleva, and A. V. Gavrilyuk, Pis'ma Zh. Tekh. Fiz. **24** (16), 79 (1998) [Tech. Phys. Lett. **24**, 657 (1998)].

5. I. V. Zolotukhin, Yu. E. Kalinin, V. A. Kondusov, *et al.*, Metallofizika (Kiev) **11** (4), 48 (1989).

6. P. D. Kim, Doctoral Dissertation (Krasnoyarsk, 1988).

Translated by P. Pozdeev

Molecular-Dynamics Study of a Possible Structural Instability during Relaxation of a Deformed Crystal

A. I. Dmitriev* and S. G. Psakhie

Institute of Strength Physics and Materials Science, Siberian Division, Russian Academy of Sciences,
Tomsk, 634055 Russia
* e-mail: dmitr@usgroups.com
Received November 5, 2004

Abstract—The development of elastic and plastic deformation in a crystal immediately upon termination of the stage of active loading has been computer-simulated by methods of molecular dynamics. Depending on the level of deformation reached at the active loading stage, the subsequent relaxation process may follow different scenarios. In particular, an interval of deformations is found for which the crystal lattice occurs in a state of unstable equilibrium, whereby small variations in the degree of compression may lead to significant changes in the character of formation of the bands of localization of atomic displacements. The obtained results may be important for an analysis of the influence of the inertial character of structural changes on the development of plastic deformation in crystals. © 2005 Pleiades Publishing, Inc.

In studying elementary events and mechanisms involved in the development of plastic deformation, it is necessary to take into account the inertial character of changes in the material structure. Indeed, the process of stress accommodation may lag behind the external action, so the elastic displacements and structural changes proceed in the material after termination of the stage of active loading [1, 2]. This delay is related to the fact that attaining a new equilibrium configuration (or returning to the initial state) requires a certain time determined by features of the relaxation process. The influence of the inertial character of structural changes can be manifested, for example, upon a change in the regime of deformation or in the course of cyclic loading. It is naturally expected that such effects are most clearly manifested upon termination of the active loading stage.

It should be noted that the class of relaxation phenomena includes both prolonged spatially extended (long-range) processes and the rapid spatially localized ones. Experimental investigation of the latter encounters considerable difficulties. This makes the task of theoretical description of the features of elastic and plastic deformation in a material immediately upon termination of the active loading stage especially important. In this context, we have studied the development of relaxation processes in a model crystal in the initial relaxation stage, that is, immediately upon termination of the stage of active loading, by method of molecular dynamics.

Relaxation processes were studied in a model crystal of copper preliminarily loaded to a certain level. The crystal had the shape of a parallelepiped with edges parallel to the crystallographic directions [100], [010], and [001] and equal to 150, 75, and 150 atomic units of

length (1 a.u. $= 0.529177 \times 10^{-10}$ m [3]). The model crystal is schematically depicted in Fig. 1, where region I is a freely deformed part of the crystal and regions II sim-
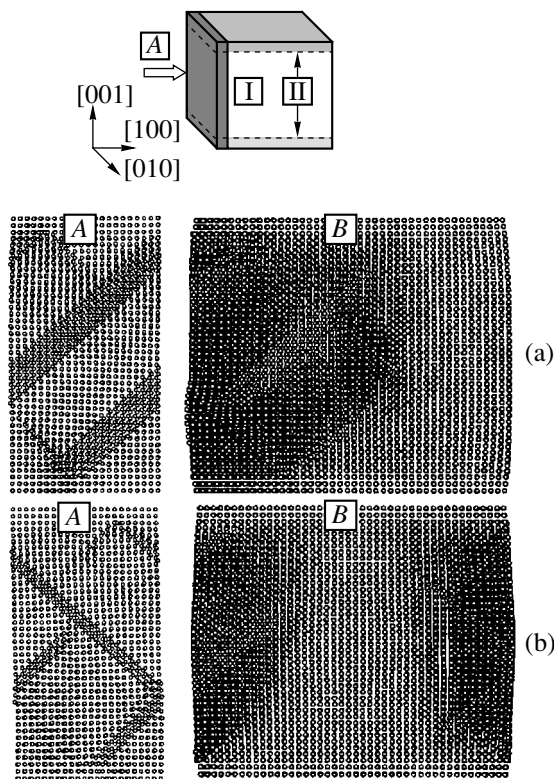

Fig. 1. Schematic diagram of the model crystal and the typical atomic configurations observed in the relaxation stage upon the initial straining to $\varepsilon = 10$ (a) and 10.5% (b). See the text for explanations.

ulate the external load. In our model, the latter regions represent the so-called string boundary conditions [4]. In order to take into account the extension of the model crystal, we used periodic boundary conditions in the [010] direction and simulated free boundaries in the [100] direction. The interatomic interactions were described within the framework of the method of embedded atom [5, 6]. The model crystal was loaded in two stages.

In the first (active) loading stage, atoms in the top and bottom regions II were assigned constant velocities along the direction [001] equal to –50 and 50 m/s, respectively, which corresponded to dynamic compression. Then, a series of calculations was performed in which the loading was continued until reaching various degrees of straining ε, up to the ultimate deformation corresponding to the onset of plastic flow.

In the second (passive) stage, we studied the course of relaxation in the model crystal. This process was traced under the conditions of terminated active loading, whereby the attained strain level was retained by fixing the final positions of atoms in regions II in the loading direction (along the [001] axis). Note that, in the directions other than [001], the positions of atoms were not fixed in both stages and the atomic coordinates (determined by the environment) were calculated by solving the equations of motion. In this paper, the results of analysis of the features of relaxation are illustrated in terms of changes of the atomic configuration in the model crystal. In order to avoid the induced effects related to the symmetry of the ideal crystal lattice, the model copper crystal was preliminarily heated to 20 K.

The results of computer simulations showed that, in the stage of active loading, plastic deformation in the model crystal takes place beginning with a degree of compression corresponding to ε ~ 12%. It was established that, if the degree of straining reached in the active loading stage is below 9.7%, the subsequent relaxation does not lead to structural changes in the model crystal. Investigation of the relaxation process in the crystal initially strained to ε > 9.7% showed that the crystal structure is subject to changes. This is manifested by the formation and development of the bands of localization of atomic displacements originating on the free surface. The sources of nucleation of the bands of localized atomic displacements occur in the regions of stress concentrators, namely, at the middle of each free surface and in the regions of contact between deformed region I and boundary regions II simulating the external load.

The results of our calculations indicated that relaxation upon the initial straining to 9.7–11% involves instability, which is manifested by the fact that rather small variations in the degree of compression (within 0.3%) may lead to significant changes in the character of the bands of localized atomic displacements. This is illustrated in Figs. 1a and 1b showing atomic configu-

rations in the model crystal observed in the course of relaxation upon straining to different extents in the initial stage. These diagrams show projections of the model crystal structure onto different crystallographic planes: patterns A and B correspond to projections onto the (100) and (010) planes, respectively. For the sake of clarity, patterns A show the projections onto the (100) plane for only the first three atomic planes at the free side of the crystal (see Fig. 1). As can be seen, the bands of localized atomic displacements in Fig. 1a are nucleated only on one of the free surfaces, while in Fig. 1b these bands are nucleated on both free surfaces. It was also found that the band of localized atomic displacements in Fig. 1a is initially nucleated only at the contact between deformed region I and boundary regions II, whereas in the case depicted in Fig. 1b, the bands originate not only at the contact between regions I and II but at the middle of the free surface as well. The bands of localized atomic displacements in the two cases have different configurations, although the atomic displacements in both cases are predominantly oriented along the $[0\bar{1}1]$ axis and in the perpendicular [011] directions.

To summarize, the results of our investigation indicate that relaxation of a preliminarily loaded crystal may involve the state of unstable equilibrium. Depending on the level of deformation reached at the active loading stage, the subsequent process of relaxation may develop according to different scenarios. Outside the interval of deformations corresponding to the state of unstable equilibrium, the new equilibrium configuration is attained via a single definite scenario.

REFERENCES

1. Yu. A. Khon, Pis'ma Zh. Tekh. Fiz. **24** (7), 79 (1998) [Tech. Phys. Lett. **24**, 280 (1998)].

2. S. G. Psakhie, T. Yu. Uvarov, K. P. Zol'nikov, *et al.*, Fiz. Mezomekh. **3** (4), 29 (2000).

3. L. D. Landau and E. M. Lifshitz, *Course of Theoretical Physics,* Vol. 3: *Quantum Mechanics: Non-Relativistic Theory* (Nauka, Moscow, 1989; Pergamon, New York, 1977).

4. A. I. Mel'ker, A. I. Mikhaĭlin, and E. Ya. Baĭguzin, Fiz. Met. Metalloved., No. 64, 1066 (1987).

5. M. S. Daw and M. I. Baskes, Phys. Rev. B **29**, 6443 (1984).

6. S. G. Psakhie and K. P. Zol'nikov, Pis'ma Zh. Tekh. Fiz. **23** (14), 43 (1997) [Tech. Phys. Lett. **23**, 555 (1997)].

Translated by P. Pozdeev

The Influence of Twin Boundaries on the Heat Capacity and Diffuse Scattering in a Crystal

V. N. Dumachev

Voronezh Institute of the Ministry of Internal Affairs of the Russian Federation, Voronezh, Russia
e-mail: dumv@comch.ru
Received September 17, 2004

Abstract—The influence of twin boundaries on the heat capacity and diffuse scattering in a crystal is described within the framework of a macroscopic dynamic theory. © 2005 Pleiades Publishing, Inc.

Achievements of the modern nanotechnologies in the synthesis of structures of arbitrary dimensions have led to the important task of studying natural low-dimensional formations in crystals, such as dislocations and domain walls, and the influence of such objects on the mechanical and kinetic properties of materials. This paper shows that coherent twin boundaries can significantly influence the thermodynamic properties of crystals.

Consider an elastic continuous medium containing a defect that acts as the source of a plastic deformation field. A local change in position of the surface of this defect will modify the mismatch between the defect and environment. In the case of a planar defect, this is manifested by the motion of misfit dislocations. The resulting configurational or surface forces act so as to bring the defect boundary to an equilibrium state, while the mismatch becomes (due to inertial properties of the medium) a source of elastic waves. Considering the total deformation of the crystal u_{lm} in the presence of the structural defect as comprising the elastic (ε_{lm}) and plastic (s_{lm}) components, the Lagrangian of the elastic continuum can be written as

$$L = \frac{1}{2}\int d\mathbf{r}\,dt(\rho(\dot{u}_i)^2 - (u_{ik} - s_{ik})\lambda_{iklm}(u_{lm} - s_{lm})). \quad (1)$$

Let us consider the coherent boundary as an independent object in the crystal possessing its own dynamical variable $\varsigma(\mathbf{r}_\parallel, t)$ representing a deviation of the boundary relative to the habit plane. Then, writing the plastic deformation caused by this deviation as

$$s_{ij} = \varsigma(\mathbf{r}_\parallel, t)\delta(z)\lfloor S_{ij} \rfloor,$$

substituting this expression into Lagrangian (1), and considering variations over the dynamical variables $u_i(\mathbf{r}, t)$ and $\varsigma(\mathbf{r}_\parallel, t)$, we eventually obtain a system of differential equations [1]

$$\rho\ddot{u}_i - \lambda_{iklm}\partial^2_{kl}u_m + \partial_k(\lambda^s_{ik}\delta(z)\varsigma(\mathbf{r}_\parallel, t)) = 0,$$

$$(\lambda^s_{ik}\partial_k u_m - \lambda^s\delta(z)\varsigma(\mathbf{r}_\parallel, t))_{z=0} = 0.$$

These equations have a self-consistent solution under the condition provided by the dispersion relation [2]

$$\frac{q_y^2 - \omega^2/c_t^2}{\sqrt{\mathbf{q}_\parallel^2 - \omega^2/c_t^2}} \quad (2)$$
$$+ \frac{4q_x^2}{\omega^2/c_t^2}(\sqrt{\mathbf{q}_\parallel^2 - \omega^2/c_l^2} - \sqrt{\mathbf{q}_\parallel^2 - \omega^2/c_t^2}) = 0.$$

Here, it is assumed that the habit plane of the boundary is perpendicular to the $0z$ axis, $[S_{ik}] = 1/2(n_iS_k + n_kS_i)$ is the offset of the plastic deformation tensor on the passage through the boundary, $n_i = (0, 0, 1)$ is vector of the normal to the boundary, $S_i = (S_x, 0, 0)$ is the vector of the boundary displacement, and $\lambda^s = S_{ik}\lambda_{iklm}S_{lm} = S_{ik}\lambda^s_{ik}$. The roots of dispersion equation (2) determine a relation between the eigenvector $\mathbf{q}_\parallel$ and the intrinsic frequency ω of bending oscillations of the boundary [3]: $\omega = \xi(\varphi)c_t\mathbf{q}_\parallel$.

First, let us calculate the phonon heat capacity of a crystal [4]. The Einstein approximation for this problem stipulates a linear dependence of the wave frequency ω on the wave vector $\mathbf{q}$. By using Eq. (2) it is also possible to take into account the influence of a nonlinear dispersion related to the presence of a planar defect in the crystal studied. The number of field oscillators with the wavenumbers below $\mathbf{q}$ can be determined as

$$N(\omega) = \int_0^q d\mathbf{q}_\parallel = \int_0^{\omega/c_t\xi(\varphi)} q\,dq\,d\varphi$$
$$= \frac{\omega^2}{2c_t^2}\int_0^{\pi/2}\frac{d\varphi}{\xi^2(\varphi)} = \frac{\omega^2}{2c_t^2}\frac{\pi}{2}\Omega,$$

where $\Omega \cong 1.074$. Then, the Debye frequency ω_0 for the

bound phonon states is

$$\omega_0^2 = \frac{4Nc_t^2}{\Omega\pi} = \frac{\omega_\theta^2}{3\Omega},$$

where ω_θ is the Debye frequency of the bulk waves. Such a considerable decrease in the Debye frequency of the twin boundary is related to softening of the phonon modes accompanying the displacement of atoms in the crystal lattice along the direction of the shear vector S_i.

Using the dispersion relation (2), we obtain the average energy of localized oscillations at low temperatures ($T \ll T_0$) in the Debye approximation:

$$\langle E_0 \rangle = \int_0^\infty \frac{\hbar\omega}{\exp(\hbar\omega/kT) - 1} dN(\omega)$$

$$= \frac{\hbar}{c_t^2}\frac{\pi}{2}\Omega\omega_0^3 2\zeta(3) = \frac{1}{\sqrt{3\Omega}}\langle E_\theta \rangle,$$

where $\zeta(3) = 1.202057$ is the Riemann zeta function and $\langle E_\theta \rangle$ is the average energy of the bulk waves in the defect-free crystal.

The heat capacity is defined as $c_v^0 = \partial E/\partial T$. However, in our case, it is convenient to calculate the ratio of this quantity to the heat capacity of the defect-free crystal:

$$\frac{c_v^0}{c_v^\theta} = \frac{\partial E_0/\partial T}{\partial E_\theta/\partial T} = \frac{\partial E_0}{\partial E_\theta} = \frac{1}{\sqrt{3\Omega}} \quad \text{or} \quad c_v^0 = \frac{c_v^\theta}{\sqrt{3\Omega}}.$$

Evidently, a decrease in the heat capacity is related to two factors: (i) a threefold decrease in the number of bulk oscillatory modes of the crystal and (ii) the anisotropic velocity of the surface wave packet propagating along the twin boundary.

The presence of a single coherent twin boundary in the crystal does not influence the positions of electron or X-ray diffraction reflections. An ensemble of parallel twins will only lead to the appearance of superstructure satellites. However, a change in the spectrum of crystal oscillations in the vicinity of the twin boundary leads to a significant decrease in the total intensity of the Born

scattering as a result of an increase in the diffuse scattering component [5].

Considering the thermal oscillations of atoms at the twin boundary as a system of elastic standing waves obeying relation (2), the influence of these oscillations on the intensity of selective maxima can be described in terms of the Debye–Waller factor

$$2M = \frac{16\pi^2 \langle u^2 \rangle}{3}\frac{\sin^2\vartheta}{\lambda^2}.$$

Here, the mean square deviation of atoms in the crystal can be expressed via the above relation for the average energy as

$$\langle u_0^2 \rangle = \int_0^\infty \frac{E_0}{\omega^2} dN(\omega)$$

$$= \int_0^\infty \frac{\hbar}{\exp(\hbar\omega/kT) - 1}\frac{dN(\omega)}{\omega} = \sqrt{3\Omega}\langle u_\theta^2 \rangle.$$

Similar to the case considered above, the presence of a coherent twin boundary in the crystal changes the observed effect by a factor of $\sqrt{3\Omega} \approx 1.8$.

REFERENCES

1. A. M. Roshchupkin, V. N. Nechaev, and V. N. Dumachev, Izv. Ross. Akad. Nauk, Ser. Fiz. **59** (10), 108 (1995).

2. V. N. Nechaev and A. M. Roshchupkin, Fiz. Tverd. Tela (Leningrad) **31** (8), 77 (1989) [Sov. Phys. Solid State **31**, 1321 (1989)].

3. L. D. Landau and E. M. Lifshitz, *Course of Theoretical Physics,* Vol. 7: *Theory of Elasticity* (Nauka, Moscow, 1987; Pergamon, New York, 1986).

4. Ya. P. Terletskii, *Statistical Physics* (Vysshaya Shkola, Moscow, 1994; North-Holland, Amsterdam, 1971).

5. V. I. Iveronova and G. P. Revkevich, *Theory of X-Ray Scattering* (Moscow State University, Moscow, 1978) [in Russian].

Translated by P. Pozdeev

The Yield of Cesium Atoms in Electron-Stimulated Desorption from Germanium-Covered Tungsten

V. N. Ageev and Yu. A. Kuznetsov

Ioffe Physicotechnical Institute, Russian Academy of Sciences, St. Petersburg 194021 Russia
Received October 6, 2004

Abstract—The yield of cesium (Cs) atoms during electron-stimulated desorption from a cesium layer adsorbed on a tungsten surface covered with a germanium film has been experimentally determined for the first time as a function of the electron energy, the germanium film thickness, the amount of adsorbed cesium, and the tungsten substrate temperature. The results are interpreted on the basis of a model of the Auger stimulated desorption. © 2005 Pleiades Publishing, Inc.

This Letter reports on the first experimental observation of the yield of cesium (Cs) atoms during electron-stimulated desorption (ESD) from a layer of cesium adsorbed on the surface of tungsten (W) covered by a germanium (Ge) film. Previously, extensive information was gained concerning the ESD of charged particles, whereas data on the ESD of neutral particles were very restricted [1]. However, in most cases, it is the yield of neutrals that determines the main component of the total flux of particles desorbed in the course of ESD. Therefore, elucidation of the laws of ESD of neutral species is especially important for the practical use of this phenomenon.

The experimental setup and method have been described in detail elsewhere [2]. The ESD measurements were performed using the time-of-flight technique during pulsed electron bombardment of a target, whereby desorbed Cs atoms were ionized in a surface-ionization detector [3]. The target was a tungsten ribbon with the dimensions $70 \times 2 \times 0.01$ mm and a (100)W crystal face predominantly emerging at the surface, which was preliminarily cleaned and textured using conventional procedures [4]. Germanium was deposited onto the tungsten ribbon from a straight-channel evaporator representing a tantalum tube charged with high-purity metallic germanium (impurity content was below 10^{16} cm^{-3}). The tube, placed near a substrate and oriented along the ribbon, had several output holes ensuring homogeneous distribution of the flux of Ge atoms over the substrate surface.

Cesium was deposited onto the target at $T = 300$ K from a resistance-heated evaporator in the course of thermal decomposition of cesium chromate. The concentration of adsorbed Cs atoms on the target surface was controlled by the time of deposition at a constant flux, the intensity of which was monitored by measuring the surface ionization current via the tungsten ribbon in the regime of saturation. The surface density of Cs atoms in a monolayer film adsorbed on the germanium-covered tungsten target was evaluated at $N_0 \sim 5 \times 10^{14}$ cm^{-2} (according to the maximum yield of Cs in the course of ESD).

The target ribbon could be cooled to a temperature in the range from 160–300 K by means of a controlled flow of gaseous nitrogen (cooled to liquid nitrogen temperature) via hollow feedthroughs. The ribbon could be also heated by electric current to a temperature determined from the temperature dependence of the electric resistance. The residual gas pressure in the vacuum chamber of the experimental setup did not exceed 5×10^{-10} Torr.

Figure 1 shows a plot of the yield q of Cs atoms versus the time of germanium deposition for the ESD of a monolayer film of cesium deposited at $T = 300$ K onto a germanium-covered tungsten target. The initial delay in the yield of Cs atoms is explained by a delay in ger-
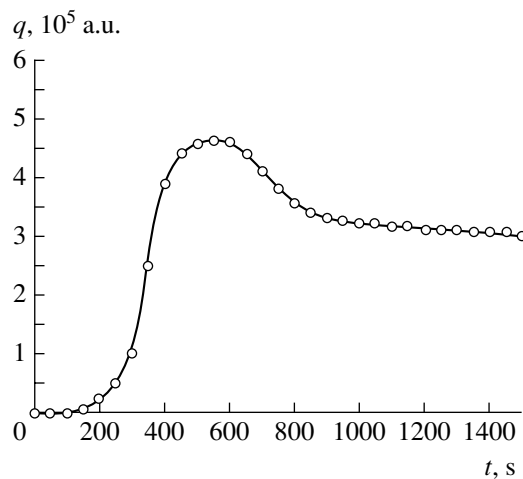

Fig. 1. A plot of the yield q of Cs atoms versus the time of germanium deposition for the ESD of a monolayer film of cesium deposited onto a germanium-covered tungsten target. Electron energy $E_e = 120$ eV.
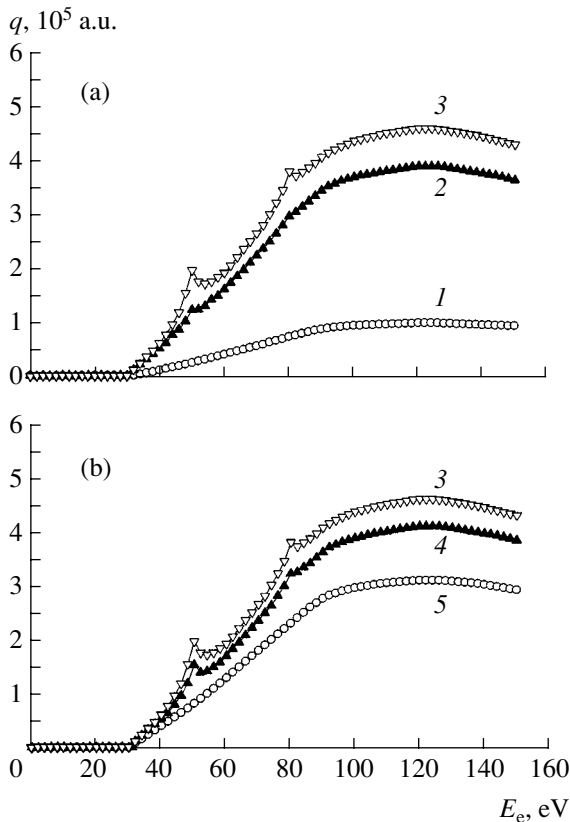
q, 10^5 a.u.

Fig. 2. Experimental plots of the yield q of Cs atoms versus the energy of bombarding electrons E_e for the ESD of a monolayer film of cesium deposited onto germanium layers of various thicknesses (ML): (*1*) 0.25; (*2*) 0.75; (*3*) 1.25; (*4*) 1.5; (*5*) 4.75.
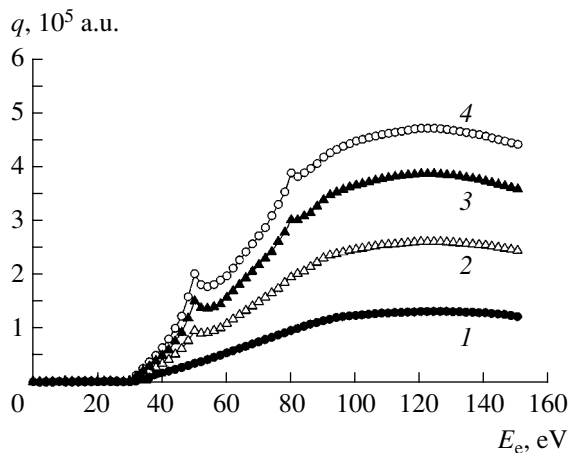
q, 10^5 a.u.

Fig. 3. Experimental plots of the yield q of Cs atoms from a monolayer germanium film on tungsten versus the energy of bombarding electrons E_e for the ESD of cesium films of various thicknesses (ML): (*1*) 0.25; (*2*) 0.50; (*3*) 0.75; (*4*) 1.0.

manium evaporation from the source, which is related to inertial heating. The subsequent linear increase in the Cs yield with the time of germanium deposition reflects stabilization of the source temperatures. The maximum

yield of Cs atoms corresponds to a one-monolayer (1 ML) film of germanium on the tungsten surface.

Figure 2 presents experimental plots of the yield q of Cs atoms versus the energy of bombarding electrons E_e for the ESD of a monolayer film of cesium deposited at $T = 300$ K onto germanium layers of various thicknesses. As can be seen, a threshold electron energy for the onset of Cs yield is independent of the thickness of the germanium film and amounts (with allowance for the emitter work function) to ~30 eV. This value is close to the ionization energy of the Ge $3d$ level [5]. For germanium films below 0.5 ML and above 2 ML, the value of q increases with E_e almost linearly up to $E_e \sim 90$ eV and then exhibits a broad maximum at approximately $E_e \sim 120$eV. In the region of intermediate germanium layer thicknesses, the $q(E_e)$ curve displays resonance peaks at the electron energies of about 50 and 80 eV. The intensity of these peaks also passes through a maximum with increasing germanium layer thickness and also depends on the coverage Θ of Cs atoms (Fig. 3). The peak at $E_e \sim 50$ eV appears for $\Theta > 0.25$, whereas the peak at $E_e \sim 80$ eV is clearly detected only for $\Theta > 0.5$. The positions of these peaks and the energy threshold of the yield of Cs atoms are independent of Θ, which indicates that the electron energy is independent of the work function of the target. The electron energies corresponding to the resonance peaks are in good agreement with the ionization energies of the W $5p$ and W $5s$ core levels [5].

The yield q of Cs atoms in ESD increases approximately linearly with the initial cesium coverage up to $\Theta \sim 0.9$ and then passes through a broad maximum. The slopes of the $q(\Theta)$ curves increase with the electron energy and are practically independent of the germanium film thickness. The q value drops with decreasing temperature, but the resonance peak heights remain virtually unchanged. The energy positions of the threshold and the resonance peaks are also not influenced by cooling of the target.

The adsorption of cesium on germanium leads to a decrease in the work function of the target. As is known [6, 7], Cs adatoms are uniformly distributed over the substrate surface at $T = 300$ K and occupy various adsorption sites, as reflected by a number of sharp peaks observed in the thermodesorption spectra [7]. At low coverages, Cs is adsorbed in the form of ions, while at $\Theta > 0.5$, the dipole–dipole repulsion decreases the binding of adsorbed species to germanium and leads to metallization of the adlayer.

The ESD of Cs atoms adsorbed on a germanium film deposited onto a tungsten ribbon can be interpreted in terms of a model of the Auger stimulated desorption, which was originally developed for description of the ESD of alkali metal atoms and ions from their adlayers on the surface of oxidized tungsten and molybdenum [8–11]. According to this model, the main channel of the ESD alkali metal atoms and ions is via the formation of a hole on the O $2s$ core level with an ionization

energy of about 25 eV, which determines a threshold for the appearance of alkali metal atoms and ions in the ESD spectra. The hole is filled at the expense of an electron taken from the O $2p$ level, which initiates the Auger process. The Auger electron either leaves the adsorption system or is trapped by the adsorbed alkali metal ion. As a result of this Auger process, the negative oxygen ion converts into a positive ion and, if the Auger electron leaves the system, this ion repels the positive alkali metal ion. This interaction leads to the ESD of positive alkali metal atoms. Should the Auger electron neutralize the positive alkali metal atom, and the positive oxygen ion restore its negative charge faster than the alkali metal ion would be reionized, the latter ion exhibits ESD as a result of overlap of its valence orbitals with those of the negative oxygen ion.

Germanium provides for a sufficiently good isolation of the adlayer of Cs atoms from tungsten, since the observed ESD yield of Cs atoms is only slightly lower than that from a cesium layer adsorbed on an oxidized tungsten surface [9]. The threshold electron energy for the yield of Cs atoms is ~30 eV, which is in good agreement with the ionization energy of the Ge $3d$ level. This agreement suggests that the mechanism of ESD in the system studied is analogous to that for the ESD of alkali metal atoms from oxidized tungsten and molybdenum surfaces. Auger electrons with an energy below 30 eV effectively neutralize adsorbed Cs^+ ions, while the positive germanium ions rapidly restore their initial charges at the expense of electrons taken from the substrate

The energy of the Auger electron capable of neutralizing an adsorbed alkali metal ion is an important factor of realization of the proposed mechanism of the ESD of alkali metal atoms, since the efficiency of neutralization of such adsorbed ions is higher for low-energy Auger electrons [10, 12].

In conclusion, we have demonstrated for the first time that Cs atoms can be desorbed upon the electron excitation of germanium.

REFERENCES

1. V. N. Ageev, Prog. Surf. Sci. **47**, 55 (1994).
2. V. N. Ageev, O. P. Burmistrova, and Yu. A. Kuznetsov, Fiz. Tverd. Tela (Leningrad) **29**, 1740 (1987) [Sov. Phys. Solid State **29**, 1000 (1987)].
3. É. Ya. Zandberg and N. I. Ionov, *Surface Ionization* (Nauka, Moscow, 1969) [in Russian].
4. É. F. Chaĭkovskiĭ, G. M. Pyatigorskiĭ, and Yu. F. Derkach, Izv. Akad. Nauk SSSR, Ser. Fiz. **38**, 376 (1974).
5. *Practical Surface Analysis by Auger and X-ray Photoelectron Spectroscopy*, Ed. by D. Briggs and M. P. Seach (Wiley, New York, 1983).
6. R. E. Weber and W. T. Peria, Surf. Sci. **14**, 13 (1969).
7. L. Surnev and M. Tikhov, Surf. Sci. **85**, 413 (1979).
8. V. N. Ageev, O. P. Burmistrova, and B. V. Yakshinskii, Surf. Sci. **194**, 1010 (1988).
9. V. N. Ageev, Yu. A. Kuznetsov, and N. D. Potekhina, Surf. Sci. **367**, 113 (1996).
10. V. N. Ageev, Yu. A. Kuznetsov, and N. D. Potekhina, Fiz. Tverd. Tela (St. Petersburg) **39**, 1491 (1997) [Phys. Solid State **39**, 1324 (1997)].
11. V. N. Ageev and Yu. A. Kuznetsov, Phys. Low-Dimens. Semicond. Struct. **1/2**, 113 (1999).
12. V. N. Ageev, O. P. Burmistrova, and B. V. Yakshinskii, Surf. Sci. **230**, 295 (1990).

Translated by P. Pozdeev

Recovering Parameters of the Ikeda Equation from Noisy Time Series

V. I. Ponomarenko and M. D. Prokhorov

Saratov Branch, Institute of Radio Engineering and Electronics, Russian Academy of Sciences, Saratov, Russia
e-mail: sbire@sgu.ru
Received September 30, 2004

Abstract—We describe a procedure for determining all parameters of the Ikeda delay-differential equation, modeling the dynamics of a passive optical resonator, from time series of the dynamical variable. It is demonstrated that the proposed procedure can be used for recovery of the nonlinear function and parameters of the Ikeda equation even in the presence of a high noise level. © *2005 Pleiades Publishing, Inc.*

In modeling spatially developed systems with feedback, it is necessary to take into account that signals propagate at a finite velocity and a certain time is required for a signal to travel a given distance. For this reason, optical systems with delayed feedback (time-delay systems)—both active and passive—are usually modeled in terms of differential equations with a delayed argument. In particular, the dynamics of a passive optical resonator is described by the Ikeda equation [1, 2]

$$\dot{x}(t) = -x(t) + \mu \sin(x(t-\tau_0) - x_0), \qquad (1)$$

where x is the dynamical variable characterizing a shift of the electric field phase in a nonlinear optical medium of the ring resonator, x_0 is the constant phase shift, μ is a coefficient proportional to the laser radiation intensity, and τ_0 is the time of light propagation in the ring resonator. It should be noted that the Ikeda equation has become one of the standard models widely used for the investigation of time-delay systems exhibiting complex dynamics.

This paper demonstrates the possibility to recover the Ikeda equation (1) from time series of the dynamical variable. In recent years, the problem of reconstruction of the nonlinear dynamical models of systems with time-delay feedback from their time series has received much attention. Since the time-delay systems possess an infinite number of the degrees of freedom and can exhibit chaotic motions of very high dimensionality [3], the task cannot practically be solved using the standard methods of reconstructing systems from their time series and special procedures have been developed for the recovery of time-delay systems [4–13]. Most of the proposed schemes are based on projecting an infinite-dimensional phase space of a given time-delay system onto low-dimensional subspaces. The quality of reconstruction of the time-delay system is evaluated in terms of criteria such as the minimum error of prediction of

the recovered model [4–7], the minimum information entropy [8], or various measures of complexity of the projected time series [9–13].

The Ikeda equation (1) belongs to a broad class of time-delay systems described by a first-order differential equation with delayed argument,

$$\varepsilon_0 \dot{x}(t) = -x(t) + f(x(t-\tau_0)), \qquad (2)$$

where f is a nonlinear function, τ_0 is the delay time, and ε_0 is a parameter characterizing the inertia of the system. In Eq. (1), $f = \mu \sin[x(t-\tau_0) - x_0]$ and $\varepsilon_0 = 1$. We have considered a system with the parameters $\mu = 20$, $\tau_0 = 2$, and $x_0 = \pi/3$, which correspond to the motion of system (1) over a chaotic attractor of high dimensionality [2]. Figure 1a shows a fragment of the typical time series of the Ikeda equation under consideration. The scale of this figure is such that 200 points of the time series account for a time interval equal to the delay time $\tau_0 = 2$. The entire time series contained 20000 points and exhibited about 1100 extrema.

In order to restore the delay time τ_0 from the observed time series $x(t)$ of the Ikeda equation, we use the method developed in [14], where it was demonstrated that a time series of the time-delay systems of type (2) contain virtually no extrema spaced from each other by τ_0. According to the proposed procedure, we count the number N of the pairs of extrema (simultaneous zeros of $\dot{x}(t)$ and $\dot{x}(t-\tau)$) for various values of τ differing from each other by the integration step $h = 0.01$ and construct the function $N(\tau)$ (Fig. 1b). The derivative $\dot{x}(t)$ was estimated from the given time series using a local parabolic approximation. The absolute minimum of $N(\tau)$ is observed for $\tau = \tau_0 = 2.00$, which exactly coincides with the delay time. It should be noted that the method proposed for determining τ_0 is quick-operating, since it makes use of only the operations of addition and comparison, not requiring compu-

tation of any measures of the complexity of motion [9–13] or the errors of data approximation [4–7].

For determining the parameter ε_0 and the nonlinear function f, the Ikeda equation is conveniently rewritten as

$$\varepsilon_0 \dot{x}(t) + x(t) = f(x(t - \tau_0)). \qquad (3)$$

As can be seen from this relation, a set of points with the coordinates $(x(t - \tau_0), \varepsilon_0 \dot{x}(t) + x(t))$ plotted on the corresponding plane will reproduce the function f. Since the quantity ε_0 is not known a priori, we have to plot $\varepsilon \dot{x}(t) + x(t)$ versus $x(t - \tau_0)$ for various ε in search for the single-valued relationship that is possible only for $\varepsilon = \varepsilon_0$. As a quantitative criterion of such a unique relationship in the search for ε_0, we can use the minimum length of a segment $L(\varepsilon)$ connecting points (ordered with respect to abscissa $x(t - \tau_0)$) on the above plane. In constructing the $L(\varepsilon)$ function (Fig. 1c), we varied the parameter ε at a step of 0.01. The minimum of $L(\varepsilon)$ is observed exactly at $\varepsilon = \varepsilon_0 = 1.00$. The corresponding set of points on the $(x(t - \tau_0), \varepsilon_0 \dot{x}(t) + x(t))$ plane (Fig. 1d) satisfactorily reproduces the nonlinear function f for Eq. (1). It should be noted that the proposed method, in contrast to other schemes reconstructing the nonlinear function using only the points corresponding to extrema or meeting some other special conditions [10, 11], makes use of all points of the given time series. This circumstance allows even short time series to be used for more complete reconstruction of the nonlinear function even in systems with weakly developed chaos. In the example under consideration, we have successfully constructed $L(\varepsilon)$ and restored the multimodal function f using only 2000 of the given time series.

The parameter μ in the Ikeda equation can be approximately evaluated from the amplitude of the sine curve in the plot of the recovered nonlinear function (Fig. 1d), after which the parameter x_0 can be calculated using the formula

$$x_0 = -\arcsin\left(\frac{\varepsilon_0 \dot{x}(t) + x(t)}{\mu}\right), \qquad (4)$$

where the quantity $\varepsilon_0 \dot{x}(t) + x(t)$ in the numerator is the value of the recovered function at $x(t - \tau_0) = 0$.

In order to refine the parameters μ and x_0, we have approximated the recovered function f by polynomials. The μ and x_0 values can be estimated to within one percent using polynomials of the 15th power and above. In particular, using approximation of the recovered nonlinear function in terms of a polynomial of the 20th power, we obtained $\mu = 19.94$ and $x_0 = 1.046$ (cf $\pi/3 \approx 1.047$).

In order to check the performance of the proposed method in the presence of perturbations, we applied it
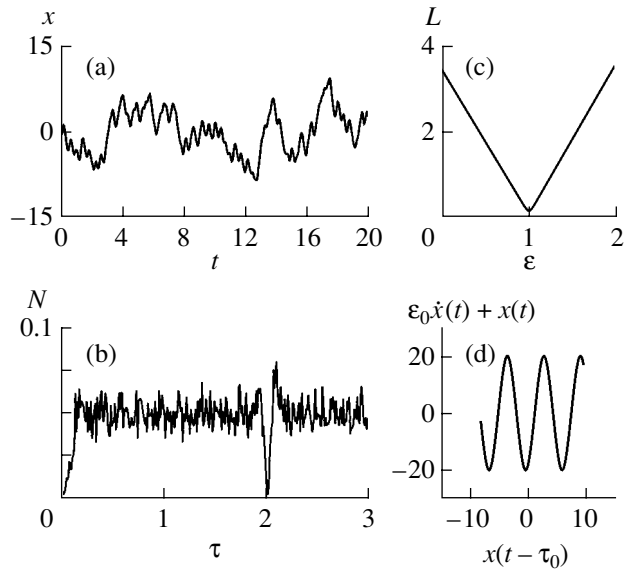

Fig. 1. Reconstruction of the Ikeda time-delay system: (a) the typical time series of the Ikeda equation (1); (b) a plot of the number $N(\tau)$ of the pairs of extrema spaced by various times τ in the given time series (normalized to the total number of such extrema; $N_{min}(\tau) = N(2.00)$); (c) a plot of the length $L(\varepsilon)$ of a segment connecting points (ordered with respect to abscissa $x(t - \tau_0)$) on the plane $(x(t - \tau_0), \varepsilon \dot{x}(t) + x(t))$ (normalized to the number of points; $L_{min}(\varepsilon) = L(1.00)$); (d) reconstruction of the nonlinear function f.

to a time series obtained by adding a Gaussian white noise with zero mean to initial time series corresponding to Eq. (1). Figure 2 presents the results of reconstruction of the Ikeda equation in the case when the added noise component had an rms deviation amounting to 20% of that for the time series without noise. Upon determining the position of minimum of the function $N(\tau)$ (Fig. 2a), we accurately restored the delay time at $\tau_0' = 2.00$, while the position of minimum of the $L(\varepsilon)$ function (Fig. 2b) provided a satisfactory estimation of the parameter of inertia: $\varepsilon_0' = 0.98$. The nonlinear function recovered for the obtained τ_0' and ε_0' values is depicted in Fig. 2c. Thus, despite a rather high noise level and an error in determining ε_0, the quality of recovery of the nonlinear function is quite satisfactory, being much better than the quality reached for the Ikeda equation with the same parameters in [15] using the method of optimal transformations (requiring considerable computational facilities). Approximating the recovered nonlinear function (Fig. 2c) using a polynomial of the 20th power, we estimated the system parameters as $\mu = 19.38$ and $x_0 = 1.048$.

To summarize, we suggest reconstruction of parameters of the Ikeda equation from the time series using a method based on the statistical analysis of the time intervals between extrema in the experimental time series and on the projection of the infinite-dimensional
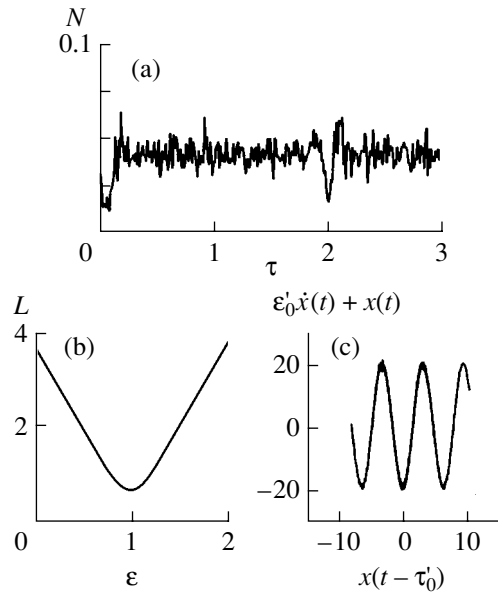
N

0.1

(a)

0   1   2   3

τ

L

4

(b)

2

0   1   2

ε

$\varepsilon'_0 \dot{x}(t) + x(t)$

20

0

−20

(c)

−10   0   10

$x(t - \tau'_0)$

Fig. 2. Reconstruction of the Ikeda time-delay system in the presence of a 20% additive noise: (a) a plot of $N(\tau)$ ($N_{min}(\tau) = N(2.00)$); (b) a plot of $L(\varepsilon)$ ($L_{min}(\varepsilon) = L(0.98)$); (c) reconstruction of the nonlinear function f.

phase space of the Ikeda system (1) onto specially selected two-dimensional subspaces. The proposed method ensures high-quality recovery of the nonlinear function and all parameters of the Ikeda equation even in the presence of a rather high noise.

REFERENCES

1. K. Ikeda, Opt. Commun. **30**, 257 (1979).
2. K. Ikeda and K. Matsumoto, Physica D **29**, 223 (1987).
3. J. D. Farmer, Physica D **4**, 366 (1982).
4. A. C. Fowler and G. Kember, Phys. Lett. A **175**, 402 (1993).
5. R. Hegger, M. J. Bünner, H. Kantz, and A. Giaquinta, Phys. Rev. Lett. **81**, 558 (1998).
6. C. Zhou and C.-H. Lai, Phys. Rev. E **60**, 320 (1999).
7. V. S. Udaltsov, J.-P. Goedgebuer, L. Larger, *et al.*, Phys. Lett. A **308**, 54 (2003).
8. Y.-C. Tian and F. Gao, Physica D **108**, 113 (1997).
9. D. T. Kaplan and L. Glass, Physica D **64**, 431 (1993).
10. M. J. Bünner, M. Popp, Th. Meyer, *et al.*, Phys. Lett. A **211**, 345 (1996).
11. M. J. Bünner, M. Popp, Th. Meyer, *et al.*, Phys. Rev. E **54**, 3082 (1996).
12. M. J. Bünner, Th. Meyer, A. Kittel, and J. Parisi, Phys. Rev. E **56**, 5083 (1997).
13. M. J. Bünner, M. Ciofini, A. Giaquinta, *et al.*, Eur. Phys. J. D **10**, 165 (2000).
14. B. P. Bezruchko, A. S. Karavaev, V. I. Ponomarenko, and M. D. Prokhorov, Phys. Rev. E **64**, 056216 (2001).
15. H. Voss and J. Kurths, Chaos, Solitons, Fractals **10**, 805 (1999).

Translated by P. Pozdeev

Chaotization of Mitron Oscillations

Er. V. Kal'yanov

Institute of Radio Engineering and Electronics (Fryazino Branch), Russian Academy of Sciences,
Fryazino, Moscow oblast, Russia
e-mail: erast@ms.ire.rssi.ru
Received October 4, 2004

Abstract—The possibility of obtaining chaotic oscillations in a mitron (voltage-tuned magnetron) is considered and illustrated by experimental results. It is shown that a mitron is capable of operating in a chaotic regime characterized by a scenario of transition to chaos via period-doubling (flip) bifurcations. © *2005 Pleiades Publishing, Inc.*

The mitron (also known as voltage-tuned magnetron) is an effective generator of microwave oscillations, which can be tuned in a broad frequency range [1, 2]. In contrast to conventional multichamber magnetrons, the mitron has a broadband oscillatory system with an interaction space formed by an interdigital electrode structure. This provides for a confined electron beam emission necessary for obtaining a bunched electron beam under conditions of relatively weak high-frequency oscillations. The confined emission is reached by placing the cathode outside of the interaction space.

The mitron has been developed as an effective source of regular oscillations with the possibility of frequency tuning in a broad range. Unlike the usual O-type backward-wave tubes (OBWTs), this device has a linear frequency characteristic, a comparatively high efficiency, and a signal-to-noise ratio reaching 140 dB/Hz. At the same time, it was demonstrated [3, 4] that the mitron admits the excitation of an electrically tunable noise, but the nature of this noise is insufficiently clear. In the context of extensive investigation of various systems, including microwave oscillators such as OBWTs [5], with respect to the possible manifestations of chaotic dynamics, it was of interest to study the noise generation in a mitron from this standpoint as well.

According to [4], the electron gun of a mitron operating in a regime of electrically tunable noise generation features noiselike oscillations with an average frequency on the order of several MHz. In such regimes, a noise-modulated electron flux is injected into the interaction space of the device. In this case, the electron gun is essentially a magnetron diode (MD) with an anode having the shape of a truncated cone.

The results of numerous previous experiments (described in sufficient detail in [1, 2, 6]) show evidence of the presence of side oscillations and a considerable excess noise in the classical MD. Filippov [7] even attempted to use an MD with a truncated-cone anode as an autooscillatory system for noise genera-

tion. It was probably the first report on the possibility of obtaining complex microwave oscillations (apparently, noiselike) with the aid of a dynamical system. On the other hand, it was suggested that a discrete set of frequencies (with an interval within the resolution of the frequency meter) could be excited, rather than the noise, since the very fact of noise generation using a dynamical system at that time seemed hardly probable. It was not until 1988 that the chaotic dynamics in MDs was clearly demonstrated by Smirnov and Usypchenko [8], who presented the power spectra showing the process of transition to chaos via the Feigenbaum scenario in accordance with the then achieved level of knowledge and the development of notions about noise generation as dynamical chaos (after the investigations of Lorenz [9] and some other researchers).

The mitron (essentially an electron-beam device of the M type) can be conditionally considered as an MD with a "probing" oscillatory system (based on the electron gun). From this standpoint, MD oscillations of relatively low frequency modulating the output signal can be characterized judging from the spectrum of microwave oscillations. This "probe" allows the structure of MD oscillations to be qualitatively studied without introducing perturbing elements into the system under consideration.

Figures 1 and 2 present the results of experiments on the chaotization of mitron oscillations (for a device operating in the decimetric wavelength range). Figures 1a–1f show the mitron oscillation spectra measured for various ratios of the control voltage U to the nominal value U_0. Figure 2 shows plots of the frequency shift (relative to the value corresponding to the nominal control voltage) and the output power (relative to the maximum value) versus the U/U_0 ratio.

The spectra in Fig. 1 illustrate the transition from regular oscillations to chaotic motions observed when the control voltage increases relative to the nominal value U_0 corresponding to the excitation of regular
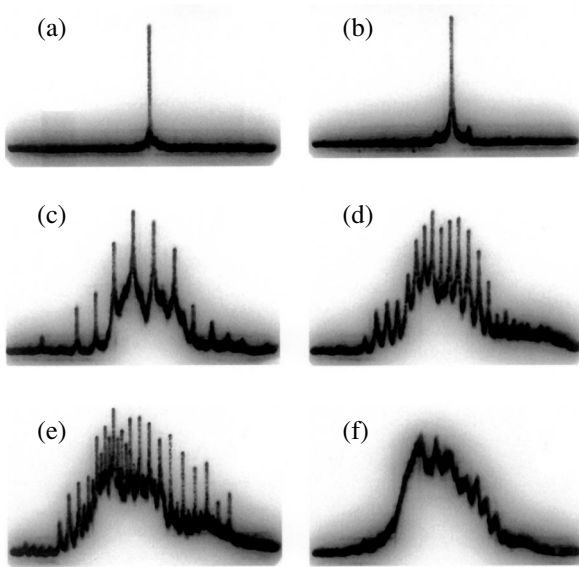
Fig. 1. The spectra of mitron oscillations measured for various ratios of the control voltage U to the nominal value U_0: (a) 1; (b) 1.24; (c) 1.28; (d) 1.36; (e) 1.42; (f) 1.44. The frequency sweep corresponds to 20 MHz at various middle frequencies; the intensity scale is logarithmic.
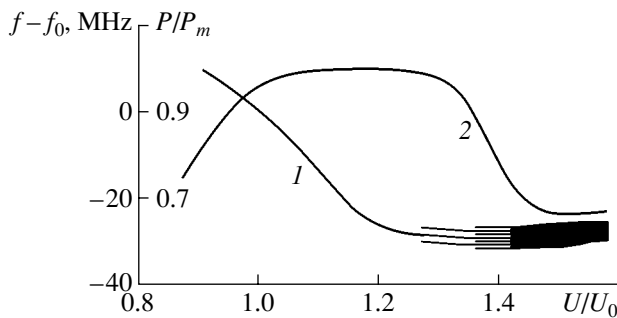

Fig. 2. Plots of (*1*) the frequency shift (relative to the value f_0 corresponding to the nominal control voltage) and (*2*) the output power (relative to the maximum value) versus the U/U_0 ratio. At $U/U_0 > 1.28$, the frequency plot qualitatively reflects changes in the mitron oscillation spectra (relative to a level of –10 dB).

oscillations at a frequency of $f_0 = 1232$ MHz (Fig, 1a, $U = U_0$). For $U/U_0 = 1.24$ (Fig. 1b) the mitron exhibits automodulation, whereby the spectrum exhibits small side components reflecting the excitation of oscillations in the region of the electron gun. This is accompanied by a decrease in the frequency (Fig. 2, curve *1*) caused by the electron bias. These oscillations modulate the electron flux, and the output spectrum acquires a set of discrete frequencies ($U/U_0 = 1.28$, Fig. 1c). This set occurs on a pedestal indicative of a noise component present both in the MD oscillations and in those generated in the interaction space. The output power exhibits a decrease (Fig. 2, curve *2*), which is evidence of a

decrease in the efficiency of interaction between the modulated electron flux and the microwave field. At $U/U_0 = 1.36$, the spectrum exhibits a change that reflects doubling of the period of modulating oscillations (Fig. 1d), while the spectrum observed at $U/U_0 = 1.42$ is indicative of the appearance of period 4 (Fig. 1e). Subsequent flip bifurcations are not distinguished on the background of excess noise. The pattern depicted in Fig. 1e changes to a noiselike spectrum (Fig. 1f, $U/U_0 = 1.44$).

The spectra presented in Fig. 1 quite clearly illustrate the transition to chaos according to the Feigenbaum scenario, although the influence of excess noise is also manifested in the motion of electron flux in crossed fields. This behavior is an example of noiselike oscillations appearing due to chaotic dynamics. However, some values of the anode voltage also make possible the transition to chaos via other scenarios, in particular, with noise generation without period-doubling bifurcations in the automodulation signal. This is probably related to a high level of excess noise, which smears the discrete frequencies appearing in the spectrum as a result of period-doubling bifurcations. Such a transition was observed in a mitron studied previously [4]. There are numerous factors accounting for the excess noise [1, 2, 6]. In particular, in crossed-field microwave devices, a significant role is played by the effect of back bombardment.

The observed manifestations of chaotic dynamics in mitrons suggest that this phenomenon can be used for controlling oscillations with respect to the signal-to-noise ratio. This ratio can be either increased or decreased by modifying the device elements responsible for the excitation of chaotic oscillations. Therefore, the knowledge about the nature of noiselike oscillations as the dynamic chaos manifestations is important for designing mitrons.

The results of investigations indicate that mitron operation in a noiselike regime may be caused by chaotic oscillations of a dynamical nature. These chaotic oscillations, generated in the electron gun of a mitron (which is essentially an MD with truncated-cone anode), modulate the electron flux exciting tunable microwave oscillations. The obtained results confirm the validity of the early attempts at creating a noise generator based on an autooscillatory system in the form of an MD which were undertaken (in 1952–1953 [7]) long before the development of notions about the possible chaotic behavior of dynamical systems.

REFERENCES

1. E. Okress, *Crossed-Field Microwave Devices* (Academic, New York, 1961; Inostrannaya Literatura, Moscow, 1961), Vol. 2.

2. V. N. Shevchik, G. N. Shvedov, and A. I. Soboleva, *Waves and Oscillations in Electron Flows at Microwave Frequencies* (Saratov State University, Saratov, 1962) [in Russian].

3. K. I. Thomassen and D. A. Dunn, Proc. IEEE **53**, 202 (1965).

4. E. V. Kal'yanov, Radiotekh. Élektron. (Moscow) **26**, 879 (1981).

5. B. P. Bezruchko, S. P. Kuznetsov, and D. I. Trubetskov, Pis'ma Zh. Éksp. Teor. Fiz. **29** (3), 180 (1979) [JETP Lett. **29**, 162 (1979)].

6. K. I. Betskiǐ, M. B. Palatov, M. B. Tseǐtlin, *et al.*, *Unwanted Oscillation in Microwave Devices*, Ed. by M. B. Tseǐtlin (Radio i Svyaz', Moscow, 1984) [in Russian].

7. M. M. Filippov, Izv. Vyssh. Uchebn. Zaved., Radiofiz. **1**, 143 (1958).

8. A. V. Smirnov and V. G. Usychenko, Radiotekh. Élektron. (Moscow) **33**, 883 (1988).

9. E. N. Lorenz, J. Atmos. Sci. **20**, 130 (1963).

Translated by P. Pozdeev

A Defect–Deformation Model
of the Surface Roughness Formation in Semiconductors
and Metals under Laser Irradiation

V. I. Emel'yanov* and K. M. Karimov

Moscow State University, Moscow, Russia
* e-mail: emel@em.msk.ru
Received September 29, 2004

Abstract—A defect–deformation (DD) model of irregular rough microstructure formation on the surface of semiconductors and metals under laser irradiation is developed. The DD model describes the development of roughness on various (from micron to nanometer) scales and agrees with the experimental data on the relationships between the surface roughness scale and the parameters of laser radiation and processed materials. Possibilities of controlled modification of the characteristics of laser-induced roughness by means of external actions are considered. © 2005 Pleiades Publishing, Inc.

Introduction. Rough surfaces of semiconductors and metals have received much attention in laser physics. This interest is related to the phenomenon of a strong increase of a local optical field and the corresponding enhancement of linear and nonlinear optical processes near such rough surfaces [1]. One method for the formation of rough solid surfaces is based on the exposure of targets to sequences of laser radiation pulses [2–4]. To our knowledge, no theory of laser-induced surface roughness formation is available that would describe the experimental dependences of the surface morphology characteristics on the parameters of laser radiation. The development of such a theory would provide a means of controlled modification of the scale and symmetry characteristics of the surface roughness ensembles, which is of considerable importance in numerous practical applications.

This Letter presents an outline of the developed defect–deformation (DD) model of irregular roughness formation on the surface of semiconductors and metals under laser irradiation. The proposed model is based on the notions about the introduction of a high density of point defects during laser irradiation of a given material, followed by their self-organization with the formation of local pileups at the extrema of a self-consistent surface relief. Predictions of the model agree with the available experimental data. It will be demonstrated that the symmetry of the surface roughness ensembles can be controlled by varying the angle of laser radiation incidence on the target surface and the level of applied mechanical stress.

DD mechanism. According to the DD model, the mechanism of surface roughness formation under laser irradiation is as follows. A sequence of laser radiation pulses with a pulse energy density F_0 exceeding the energy of melting F_m creates a high concentration n_v of vacancies in a surface layer of thickness h in a target crystal. Being highly mobile at elevated temperatures, these vacancies are initially uniformly distributed over the exposed surface. Let us consider the defect-rich layer of thickness h as a surface film possessing elastic properties different from those of the remaining crystal (substrate).

It was demonstrated previously (see review [5] and more recent paper [6]) that, when the concentration of mobile defects (vacancies) in the film exceeds a certain critical level ($n_v > n_{vc}$), the film features the development of DD instability. This instability results in the formation of a grating of the surface relief modulation at a rate of λ_q. The relief is modulated according to the law $\zeta(\mathbf{r}) = \zeta_q\cos(\mathbf{qr} + \phi(\mathbf{q}))\exp(\lambda_q t)$, where $\zeta(\mathbf{r})$ is the local surface deviation along the z axis (directed inward the crystal), $\mathbf{q}$ is the grating vector lying in the surface plane, $\mathbf{r} = \{x, y\}$ is the radius vector, ζ_q is the real amplitude, and $\phi(\mathbf{q})$ is the random phase. The vacancies tend to accumulate in the wells of the relief, thus forming the surface DD grating. The period $d = 2\pi/q_m$ of the dominating DD gratings (growing at the maximum rate λ_{qm}) is proportional to the film thickness h. At a sufficiently high concentration of defects, this period is $d \approx 2h$ [5, 6]. In addition to the dominating DD gratings having the wave vectors $\mathbf{q}_m$ with randomly distributed orientations, there arises a continuum of DD gratings with random orientations and the wave vectors close to q_m in the gain band $\lambda_q > 0$. It is the superposition of this continuum (separated in the gain band) that accounts for the pattern of chaotic modulation (i.e., roughness) of the surface relief with the characteristic scale $2h$ over the surface (Fig. 1).
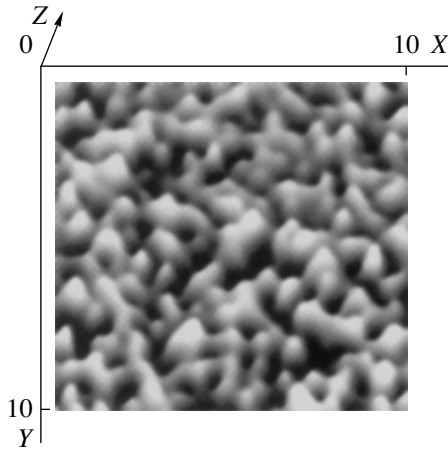
Fig. 1. The pattern of a surface relief (in dimensionless units) $Z(X, Y, T) = \zeta(x, y, t)/\zeta_0$, where ζ_0 is the DD model parameter, $X = xq_m$, $Y = yq_m$, and $T = t\lambda_{qm}$. The relief height Z was calculated using the formula

$$Z(X, Y, T)$$
$$= \int_0^{2\pi} d\varphi \int_0^2 dQ \cos(Q_X X + Q_Y Y + \phi(Q, \varphi)) \exp(\Lambda(Q)T),$$

where $Q_X = Q\cos\varphi$, $Q_Y = Q\sin\varphi$, $Q = q/q_m$, and $\Lambda(Q) = \lambda_q/\lambda_{qm} = 1 - (Q-1)^2$, and $\phi(Q, \varphi)$ is a phase randomly distributed in the $[0, 2\pi]$ interval.

Laser-induced surface roughness formation. Let a sequence of N laser pulses with $F_0 > F_m$ act on the target (metal or semiconductor) surface within a spot (laser beam) radius of r_0. Each pulse produces a surface layer of melt with thickness h_m (we assume that the resulting thickness of the defect-rich layer formed by the sequence of laser pulses is $h \gg h_m$). In addition, the laser-induced heating of the medium leads to the appearance of a deformed region with the characteristic size $2r_0$ in the lateral directions and along the z axis. In

this region, the strain is $\xi \simeq \alpha_T \Delta T$ (where α_T is the thermal expansion coefficient and ΔT is the laser-induced temperature increase) and the strain gradient along the z axis is $\partial\xi/\partial z \sim -\xi/2r_0 < 0$. The flux of vacancies drifting from the melt inward the medium is $j_v = n_v\theta_v(\partial\xi/\partial z)D_v/kT$, where $\theta_v < 0$ is the deformation potential, D_v is the vacancy diffusion coefficient, $T = T_0 + \Delta T$, and T_0 is the initial temperature. The drift of vacancies inward the medium takes place during a period of time when the temperature-induced strain exists, which can be estimated as $\tau_{drift} = r_0^2/\chi$, where χ is the thermal diffusivity. During this period, vacancies penetrate to a depth of $v\tau_{drift} = \theta_v(\partial\xi/\partial z)(D_v/kT)(r_0^2/\chi)$.

Upon termination of the N-pulse sequence, the double thickness of the vacancy-rich film (formed under the condition $\Delta T \gg T_0$) is

$$2h = 2Nv\tau_{drift} = Nr_0(\theta_v\alpha_T D_v/\chi k_B). \quad (1)$$

Formula (1) shows that the scale of roughness linearly increases with the number of laser pulses N (this growth exhibits saturation at $h \sim 2r_0$) and with the laser spot size r_0 (size effect) and exhibits exponential dependence on the laser pulse energy F_0 ($D_v = D_{v0}\exp[-E_m/k_B T]$).

Discussion. Dolgaev *et al.* [3] observed the formation of a microstructure on the surface of silicon, germanium, and titanium crystals under the action of $N = 10^4$ pulses of nonpolarized radiation of a copper vapor laser ($\lambda = 510.6$ nm; pulse duration, $\tau = 20$ ns; spot size, $r_0 = 20$ μm) with an energy density of ~1 J/cm^2, incident at an angle of 60°–90°. Figure 2a shows the typical scanning electron microscopy (SEM) image of roughness observed on the surface of titanium. As can be seen, this pattern is analogous to that predicted by the DD model. We have determined a Fourier spectrum for the structure presented in Fig. 2. This spectrum
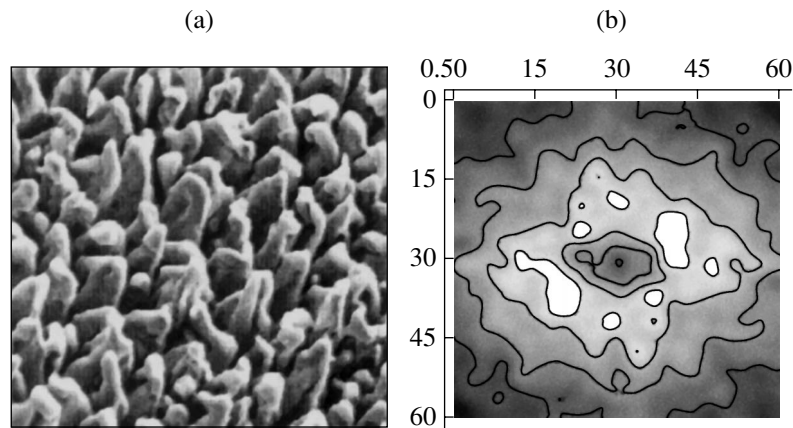

Fig. 2. A rough surface of titanium upon irradiation with $N = 10^4$ laser pulses with $F = 1$ J/cm^2 in vacuum: (a) A SEM micrograph (the average distance between roughness peaks is about 15 μm) [3]; (b) the corresponding 2D Fourier spectrum (calculated in this study).

(Fig. 2b) comprises a ring with a finite width corresponding to the pattern of chaotic superposition in Fig. 1. Three pairs of local maxima observed in the ring are indicative of a tendency to the formation of a quasi-hexagonal structure, which can be explained by nonlinear processes of angular self-organization of the DD grating modes (cf [7]). For $\theta_v \simeq 8 \times 10^{-18}$ J, $D_v \simeq 5 \times 10^{-8}$ cm^2/s, and $\alpha_T \approx 10^{-4}$, formula (1) yields an estimate of the roughness scale $2h \approx 14$ μm, which is close to the experimental value. It should be noted that the number of pulses used in [2] is about one-tenth of that in [3] and, accordingly, the roughness scale in the former case (5 μm [2]) is smaller than that in [3]. The scale of roughness exhibits a severalfold decrease with increasing distance from the laser spot center. This behavior also qualitatively agrees with formula (1).

The symmetry of the surface roughness ensemble can be changed from quasi-hexagonal to quasi-one-dimensional by applying a uniaxial mechanical stress (by analogy with what was reported for an ensemble of pores [8]) or by increasing the angle of incidence of the laser beam. As can be seen from Fig. 2b, where one pair of local maxima is more intense than the others, the oblique incidence selects a dominating direction in the DD grating formation. In semiconductors, the role of additional characteristic surface film thickness can be also played by the space charge region thickness H. Then, the DD model predicts the formation of a surface microstructure characterized by two scales, $2h$ and $2H$.

In this way, the DD model explains the formation of both large-scale (2–3 μm) and small-scale (~100 nm) roughness observed upon pulsed laser irradiation of a cadmium telluride semiconductor compound [4].

REFERENCES

1. V. I. Emel'yanov and N. I. Koroteev, Usp. Fiz. Nauk **135**, 345 (1981) [Sov. Phys. Usp. **24**, 864 (1981)].

2. T. H. Her, R. J. Finlay, C. Wu, *et al.*, Appl. Phys. Lett. **73**, 1673 (1998).

3. S. I. Dolgaev, S. V. Lavrishev, A. A. Lyanin, *et al.*, Appl. Phys. A **73**, 177 (2001).

4. A. Baĭdullaeva, M. B. Bulakh, A. I. Vlasenko, *et al.*, Fiz. Tekh. Poluprovodn. (St. Petersburg) **38**, 26 (2004) [Semiconductors **38**, 23 (2004)].

5. V. I. Emel'yanov, Kvantovaya Élektron. (Moscow) **28**, 1 (1999).

6. V. I. Emel'yanov and D. V. Babak, Appl. Phys. A **74**, 797 (2002).

7. V. I. Emel'yanov, V. V. Igumnov, and V. V. Starkov, Pis'ma Zh. Tekh. Fiz. **30** (10), 83 (2004) [Tech. Phys. Lett. **30**, 438 (2004)].

8. V. I. Emel'yanov, K. I. Eremin, V. V. Starkov, and E. Yu. Gavrilov, Pis'ma Zh. Tekh. Fiz. **29** (6), 19 (2003) [Tech. Phys. Lett. **29**, 226 (2003)].

Translated by P. Pozdeev

Plasma Flow Crisis and the Limiting Electron Temperature in a Vacuum Arc in Axial Magnetic Field

I. A. Krinberg

Irkutsk State University, Irkutsk, Russia
e-mail: krinberg@physdep.isu.ru
Received November 4, 2004

Abstract—The possibility of supersonic motion of cathode plasma in a low-current vacuum arc in an axial magnetic field has been studied. It is shown that an increase in the electron temperature unavoidably leads to a plasma flow crisis, whereby the plasma velocity decreases to the sound velocity. The dependence of the limiting length of a stationary flow on the magnetic field has been studied. The maximum possible electron temperature T_{cr} in the plasma is determined by the initial ion energy and can be estimated as $T_{cr} \approx 3T_m$, where T_m is the maximum electron temperature in the cathode spot region. © 2005 Pleiades Publishing, Inc.

Introduction. As is known [1, 2] energy supply to a supersonic cylindrical gas (plasma) flow leads to a decrease in the flow velocity. If a continuous transition to subsonic velocities is impossible, the flow exhibits crisis at a certain distance from the initial cross section, whereby the stationary motion becomes no longer possible. Such situations can arise in a supersonic plasma flow ejected from a cathode spot region in vacuum arc discharge [3]. Previously [4, 5] the critical conditions were analyzed for a high-current vacuum arc, in which the velocity of "fast" ions emitted from the cathode was found to decrease to the sound velocity as a result of the interaction with a counterflow of "slow" ions emitted from the anode.

This paper considers the possibility of a plasma flow crisis caused by the application of an axial magnetic field to a low-current vacuum arc discharge with a hollow or grid anode, in which case the flow of ions from the anode is practically absent.

Recently, it was demonstrated [6] that radially expanding (cone-shaped) plasma flow from cathode to anode is transformed into a flow along the applied magnetic field, provided that the frequency of electron–ion collisions becomes lower than the Larmor frequency. The electron temperature in the direction along the flow continuously increases as a result of Joule heating, which leads to a decrease in the flow velocity. The change in the flow velocity was ignored in [6], but it was taken into account in the refined model [7]. The latter modified variant of the model is applied below to an analysis of the crisis of a current-carrying plasma flow in an external magnetic field.

Plasma flow model. The quasi-one-dimensional model [7] assumes a constant value of the axial current density, as well as constant plasma density and temperature in the flow cross section. The ion temperature is considered negligibly small compared to the electron temperature. The plasma flow viscosity and thermal conductivity are ignored. Under these assumptions, the system of equations describing the parameters of quasi-neutral plasma as functions of the distance z from the cathode spot is as follows:

$$\frac{d}{dz}(\rho V_z S) = 0, \tag{1}$$

$$\rho V_z S \frac{dV_z}{dz} = \left(-\frac{d(PS)}{dz}\right) + \left(\frac{I}{c}\right)^2 \frac{d\ln R}{dz}, \tag{2}$$

$$\rho V_z S \frac{dV_R}{dz} = \frac{3PS}{R} - \frac{2}{R}\left(\frac{I}{c}\right)^2 - \frac{\sigma I B^2}{ec^2 N_e}\frac{dR}{dz}, \tag{3}$$

$$\frac{3}{2}\frac{dT_e}{dz} = T_e \frac{d\ln N_e}{dz} + \frac{eI}{\sigma S}. \tag{4}$$

Here, I is the discharge current; $B = \mathrm{const}$ is the applied axial magnetic field; $\rho = mN_e/Z_i$ and $P = T_e N_e$ are the plasma density and pressure, respectively; N_e and T_e are the electron density and temperature, respectively (in energy units); V_z is the longitudinal velocity of ions (plasma); m and Z_i are the ion mass and average charge, respectively; σ is the plasma conductivity; c is the velocity of light; e is the electron charge; $S = \pi R^2$ and R are the cross section area and radius of the plasma jet; and $V_R = V_z(dR/dz)$ is the radial velocity at the side boundary of the plasma jet. For a stationary flow with neglect of the viscosity and thermal conductivity, relations (1)–(3) in the absence of an external magnetic field ($B = 0$) coincide with the analogous equations in [8].

Plasma flow crisis. By excluding the particle density from Eqs. (2)–(4) with the aid of Eq. (1), it is pos-
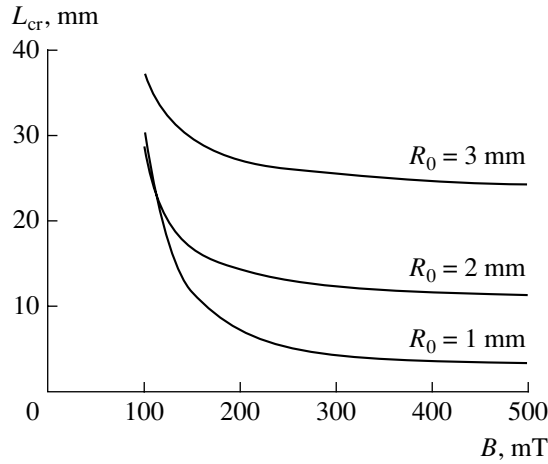
Fig. 1. Plots of the critical length L_{cr} of the plasma flow versus external magnetic field for various values of the initial flow radius (cathode material, copper; discharge current, 200 A).
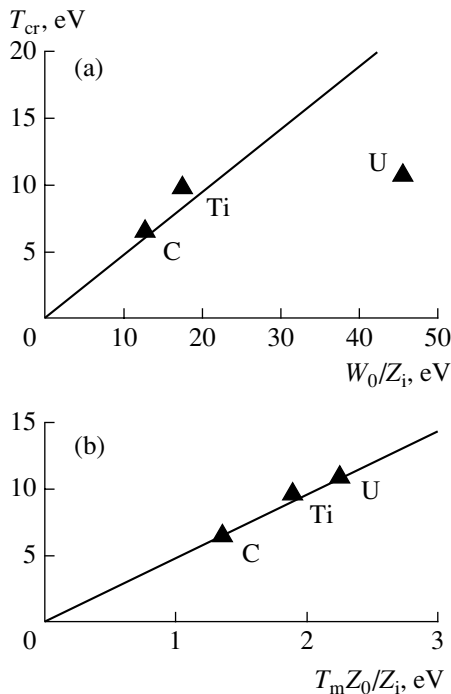

Fig. 2. Plots of the critical electron temperature T_{cr} for a low-current vacuum arc in a magnetic field versus (a) initial ion energy and (b) electron temperature in the cathode spot. Solid lines show the results of calculations using (a) formula (6) and (b) formula (7); symbols represent comparative experimental data [9, 11–14].

sible to obtain a linear algebraic system of equations with respect to the first derivatives of T_e, V_z, V_R, and R. A determinant of this system is $DET = (3/2)V_z(1 - C_S^2/V_z^2)$, where $C_S = (5Z_iT_e/3m)^{1/2}$ is the local ion sound velocity. If the determinant vanishes at a certain point $z = L_{cr}$, the system exhibits a singularity at this point

that corresponds to the impossibility of a stationary motion for $z > L_{cr}$ [4, 5]. In the case under consideration, $DET = 0$ at $V_z = C_S$. The corresponding value of the limiting (critical) flow length L_{cr} can be determined by numerically solving the system of Eqs. (1)–(4) supplemented by the balance equations for the ion composition [6, 7]. The results of such calculations are presented in Fig. 1.

Limiting electron temperature. Integrating Eqs. (1) and (2), we obtain the relation

$$V_z - \gamma V_0 \ln R + \frac{Z_i T_e}{mV_z} = V_0 - \gamma V_0 \ln R_0 + \frac{Z_0 T_0}{mV_0}, \quad (5)$$

where V_0, T_0, Z_0, and R_0 are the flow parameters in the input cross section; $\gamma = eI/(mc^2V_0\delta)$ is a dimensionless parameter [7]l; $\delta = eG/mI < 0.1$ is the erosion coefficient [3]; and $G = \rho VS = const$ is the mass flux.

The input cross section can be placed in the region where the cathode plasma microjets merge together to form the common flow. Within a microjet, the maximum electron temperature is $T_m \approx 1.5$–4.5 eV [9]. The ions are accelerated up to $V_0 = M(5Z_0T_m/3m)^{1/2}$, where the Mach number $M \approx 3.5$ is the same for all cathode materials [10, 11]. In the region of mixing ($z = 0$), the ion velocity and average charge are approximately the same as those at the end of the microjet, while the electron temperature decreases ($T_0 < T_m$) [10]. Since $M^2 \gg 1$, the last term in relation (5) can be ignored. For the discharge currents $I \le 500$ A, we have $\gamma \le 0.1$ [7] and, hence, the corresponding term can be ignored as well. Then, for a critical point (where $V_z = V_{cr} = C_S$, $T_e = T_{cr}$), Eq. (5) yields $V_{cr} = (5/8)V_0$ and

$$T_{cr} = \frac{15W_0}{32Z_i}, \quad (6)$$

where $W_0 = mV_0^2/2$ is the initial kinetic energy of ions. Taking into account the relation between V_0 and T_m, it is possible to express the limiting (critical) electron temperature in the plasma flow through the maximum temperature in the cathode spot:

$$T_{cr} = \alpha \frac{Z_0}{Z_i}T_m, \quad (7)$$

where $\alpha = 75M^2/192 \approx 4.8$.

Figure 2 shows a comparison of the relations (6) and (7) to experimental data. The values of electron temperature for a vacuum arc in a magnetic field were taken from [12]; the initial ion energy, from [11, 13]; the Z_i and Z_i/Z_0 values, from [14]; and the temperature in the cathode spot, from [9]. As can be seen from Fig. 2a, formula (6) shows quite good agreement with the data for carbon (C) and titanium (Ti) cathodes and a significant deviation from the data for the uranium (U) cathode.

However, it should be noted that the experimental data for C and Ti are represented by the results of W_0 measurements reported in [11], while the data for U refer to the earlier W_0 measurements [13] (characterized by the authors as less accurate and somewhat overstated). The agreement of relation (7) with the experiment is quite satisfactory for all cathode materials (Fig. 2b). Taking into account that a low-current arc in a magnetic field is characterized by $Z_i/Z_0 \approx 1.5$, we obtain from relation (7) a simple estimate for the limiting temperature: $T_{cr} \approx 3T_m$.

Conclusion. The above considerations show that a stationary supersonic plasma flow in a low-current vacuum arc in a magnetic field can exist in the entire interelectrode gap with a length L below a certain value ($L < L_{cr}$). If $L > L_{cr}$, the velocity flow decreases to the sound velocity and the flow crisis takes place with two possible outcomes: (i) the plasma flow behind the cross section where $V_z = C_S$ changes from stationary to pulsating [1] or (ii) the initial cross section increases (via possible expansion of the cathode spot) so that the critical length grows (Fig. 1) to become equal to the interelectrode gap width ($L_{cr} = L$). In the latter case, the flow velocity decreases to the sound velocity only near the anode. In both cases, the electron temperature will be close to the limiting (critical) value, which is confirmed by acceptable agreement between theoretical estimates and measured data.

REFERENCES

1. I. I. Novikov, *Applied Magnetic Fluid Dynamics* (Atomizdat, Moscow, 1969) [in Russian].

2. G. N. Abramovich, *Applied Gas Dynamics* (Nauka, Moscow, 1991), Vol. 1.

3. G. A. Mesyats and S. A. Barengol'ts, Usp. Fiz. Nauk **172**, 1113 (2002) [Phys. Usp. **45**, 1001 (2002)].

4. Ya. I. Londer and K. N. Ul'yanov, Teplofiz. Vys. Temp. **39**, 699 (2001).

5. Ya. I. Londer and K. N. Ul'yanov, Teplofiz. Vys. Temp. **42**, 198 (2004).

6. I. A. Krinberg, Pis'ma Zh. Tekh. Fiz. **29** (12), 42 (2003) [Tech. Phys. Lett. **29**, 504 (2003)].

7. I. A. Krinberg, Prikl. Fiz. **6**, 77 (2004).

8. V. V. Vikhrev and S. I. Braginskii, in *Reviews of Plasma Physics*, Ed. by M. A. Leontovich (Gosatomizdat, Moscow, 1980; Consultants Bureau, New York, 1986), Vol. 10, pp. 243–318.

9. A. Anders, Phys. Rev. E **55**, 969 (1997).

10. I. A. Krinberg, Zh. Tekh. Fiz. **71** (11), 25 (2001) [Tech. Phys. **46**, 1371 (2001)].

11. A. Anders and G. Y. Yushkov, J. Appl. Phys. **91**, 4824 (2002).

12. M. Galonska, R. Hollinger, *et al.*, in *Proceedings of the 21st International Symposium on Discharges and Electrical Insulation in Vacuum, Yalta, 2004*, Vol. 1, pp. 209–212.

13. G. Y. Yushkov, A. Anders, E. M. Oks, and I. G. Brown, J. Appl. Phys. **88**, 5618 (2000).

14. E. M. Oks, A. Anders, *et al.*, IEEE Trans. Plasma Sci. **24**, 1174 (1996).

Translated by P. Pozdeev